PROPAGATION OF LIGHT

IN ENSEMBLES OF

SEMICONDUCTOR

NANOWIRES

SILKE L. DIEDENHOFEN

Propagation of Light in Ensembles of Semiconductor Nanowires

Silke L. Diedenhofen

Propagation of Light in Ensembles of Semiconductor Nanowires

PROEFSCHRIFT

ter verkrijging van de graad van doctor aan de
Technische Universiteit Eindhoven, op gezag van de
rector magnificus, prof.dr.ir. C.J. van Duijn, voor een
commissie aangewezen door het College voor
Promoties in het openbaar te verdedigen op
maandag 20 december 2010 om 16.00 uur

door

Silke Luzia Diedenhofen

geboren te Goch, Duitsland

Dit proefschrift is goedgekeurd door de promotor:

prof.dr. J. Gómez Rivas

Copromotoren:
prof.dr. E.P.A.M. Bakkers
en
prof.dr. A. Fiore

L'essentiel est invisible pour les yeux
- Le Petit Prince,
Antoine de Saint-Exupéry

Contents

<div align="right">

CHAPTER 1

</div>

INTRODUCTION

1.1 Semiconductor Nanowires

Semiconductor nanowires are novel nanostructures with a diameter in the subwavelength range and large aspect-ratios. Recent developments in bottom-up nanofabrication techniques allow the growth of free-standing semiconductor nanowires with controlled composition, lateral dimensions of typically 10 to 1000 nm, and lengths of several micrometers. A scanning electron micrograph of a single nanowire lying on a substrate is shown in Figure 1.1. The growth of nanowires based on group IV [1], III/V [2–5], and II/VI [6, 7] semiconductors has been demonstrated. The small lateral dimensions of nanowires enables to grow them hetero-epitaxially onto different substrates [8–10] or even to design heterostructures with segments, shells, and/or quantum dots of different semiconductors in a single nanowire [5, 11–13]. Nanowires are promising nanostructures for optical [2–4, 14–18], electrical [19, 20] and opto-electronical [21] applications. Lasing [14], LEDs [2], and photosensitive devices [15] have been demonstrated on single nanowires. Ensembles of nanowires are recognized as promising materials for large area LED's [3], anti-reflection coatings [22], and solar cells [17, 23].

In this thesis, we describe how light propagates in ensembles of semiconductor nanowires. Propagation of light in ensembles of nanowires is strongly influenced by their diameter. We demonstrate that ensembles of thin nanowires form one of the strongest optically anisotropic media reported so far. This optical anisotropy is tunable, not only depending on the diameter or filling fraction of the nanowires, but also on the orientation of the nanowires with respect to the substrate. Additionally, we show that the optical anisotropy can be modified by adding a thin shell of SiO_2 around the nanowires. The strong modification of the optical anisotropy due to the SiO_2 shell renders ensembles of nanowires a promising medium for sensing applications.

We characterize layers of thick nanowires and we find that they belong to the strongest scattering media to date. Scattering of light by ensembles of nanowires is anisotropic and depends on the orientation of the nanowires.
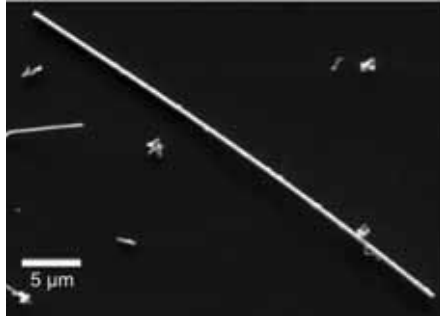
Figure 1.1: Scanning electron micrograph of a semiconductor nanowire lying on a substrate.

The bottom-up growth process of nanowires allows for growing the nanowires such that their top diameter is smaller than their base diameter. We demonstrate that dense ensembles of these tapered or conically shaped nanowires exhibit a graded refractive index that increases the light coupling into high refractive index semiconductors.

We have measured the reflection of arrays of base-tapered InP nanowires and we find that the very broadband and omnidirectional low reflection of these layers is due to enhanced optical absorption in the nanowire layer. This strong absorption renders nanowires as promising building blocks for solar cells.

In this chapter, we introduce nanowires and optical properties of single nanowires. In Section 1.3 we reveal how optical properties of single nanowires influence the propagation of light in ensembles of nanowires. We give an outline of this thesis in Section 1.4.

1.2   Optical Properties of Single Nanowires

The large geometrical anisotropy of thin nanowires, characterized by the large difference between the length of the nanowire and its diameter, leads to a strong optical anisotropy. Giant polarization anisotropy was demonstrated for the absorption and the photoluminescence emission of single nanowires [15]. From standard textbook Mie calculations [24], the scattering anisotropy of infinitely long cylinders embedded in a homogeneous medium can be determined for plane waves incident as depicted in Figures 1.2a and 1.2b.

A typical measure of the scattering strength is the scattering efficiency. The scattering efficiency is the ratio between the scattering cross section and the geometrical cross section of a scatterer. The scattering cross section is a hypothetical area which is given by the ratio of the total scattered power to the incident irradiance while the geometrical cross section is given by the projected area of the scatterer on the plane perpendicular to the incident wavevector. Usually, efficiencies are defined such that they are less than unity. However, the scattering efficiency is not so constrained. Figure 1.3a shows the scattering efficiency of an infinitely long GaP nanowire with a refractive index of 3.3 at a wavelength of 690 nm. The nanowire is embedded in air and the calculation is done as a function of
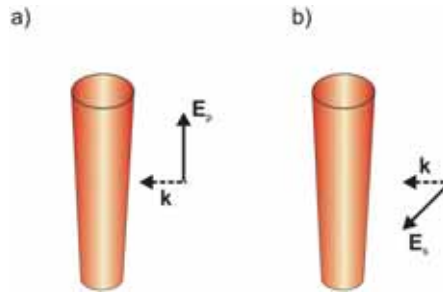
Figure 1.2: Incident plane wave onto a nanowire polarized parallel (a) and perpendicular (b) to the long axis of the nanowire. The vector represented by the dotted line is the **k**-vector of the incident wave, while the solid line vector displays the polarization.

its diameter for light polarized parallel (solid black curve) and perpendicular (red dashed curve) to the nanowire axis. For a small nanowire diameter, light polarized parallel to the nanowire long axis is scattered more efficiently than light polarized perpendicular to the nanowire long axis. The scattering efficiency does not only depend on the polarization, but also the diameter of the nanowire has an important influence. The scattering cross section and the geometrical cross section are nearly identical for a nanowire diameter of ~ 300 nm, resulting in a scattering efficiency around unity. Strong resonances occur for nanowire diameters slightly smaller or bigger than 300 nm. These resonances indicate that nanowires with these diameters interact more strongly with the incident plane wave. The fluctuations of scattering efficiency are called Mie resonances. The ratio of the two scattering efficiencies for light that is polarized parallel and perpendicular to the nanowire long axis is depicted in Figure 1.3b for an incident wavelength of 690 nm. For a nanowire diameter of 51 nm, the ratio reveals a pronounced maximum of 140. For larger diameters, the ratio converges to 1, meaning equal scattering efficiency for incident light polarized parallel or perpendicular to the long axis.

The large scattering anisotropy of nanowires becomes obvious when performing bright-field optical microscopy. Figure 1.4 shows two bright-field optical micrographs of InP nanowires with a diameter of 50 nm lying on top of a SiO_2 substrate. The two images are taken on the same position of the sample. The only difference between the two images is the orientation of the detected polarization of light. As scattering of light from nanowires is strongly anisotropic, only the nanowires that are aligned with the detector polarization are visible.

1.3   Optical Properties of Ensembles of Nanowires

The bottom-up method used for growing nanowires allows the growth of layers with different nanowire diameters, densities, lengths, and position of the nanowires. If these nanowires are grown with all lateral dimensions smaller than the wavelength of visible light, i.e., the distance between the nanowires and their diameter are smaller than the
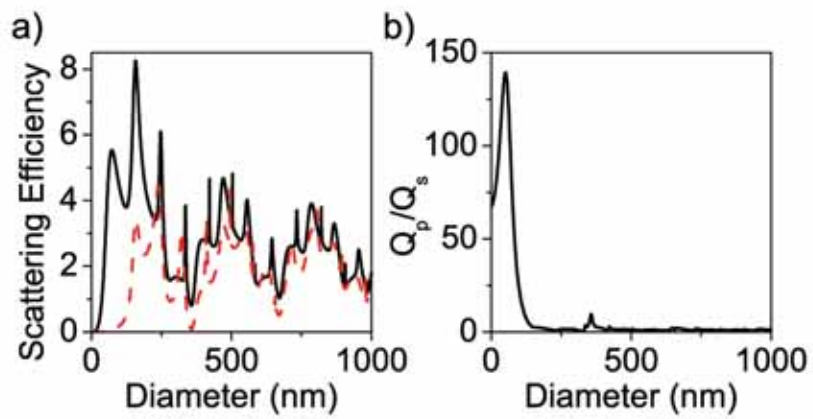
Figure 1.3: a) Scattering efficiency at λ = 690 nm as a function of diameter of an infinitely long GaP nanowire with refractive index n = 3.26 embedded in air for light polarized parallel (solid black curve) and perpendicular (red dashed curve) to the long axis of the nanowire. b) Ratio of the two scattering efficiencies.
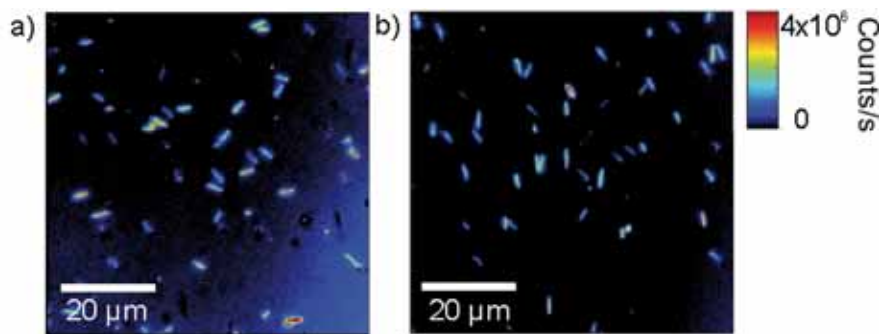
Figure 1.4: Bright field scattered intensity of nanowires lying on a substrate with a polarization along a) the horizontal and b) the vertical directions. The directions of the polarization are indicated by the arrows. The two images are taken at the same position of the sample. Nanowires lying oriented with the direction of the polarization are visible.

wavelength, the layer of nanowires can be described as a homogeneous medium with effective optical constants [25]. Figure 1.5 shows a scanning electron micrograph of an ensemble of GaP nanowires with all lateral dimensions smaller than the wavelength of light. The optical properties of this medium can be tuned, depending on these dimensions. High density ensembles of nanowires form a strongly anisotropic material. A measure of the anisotropy of the material is the birefringence, i.e., the refractive index of a birefringent medium depends on the polarization of light.

Layers of thick nanowires form a strongly scattering medium, which is opaque due to multiple scattering. Layers of short nanorods that are conically shaped exhibit a graded refractive index. This graded refractive index reduces the reflection of the substrate due to optical impedance matching. If the nanowires are periodically patterned and the pitch is in the order of the wavelength of light, photonic crystals can be fabricated with tailored optical properties.
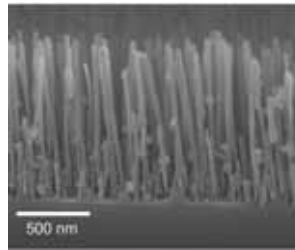
Figure 1.5: Scanning electron micrograph of an ensemble of GaP nanowires.

1.4   Outline of this Thesis

In this thesis, we describe how light propagates in ensembles of semiconductor nanowires. The outline of the thesis is as follows.

In Chapter 2 we explain the growth of GaP nanowires and InP/InAsP/InP nanowires. The nanowires considered in this thesis are grown using the vapor-liquid-solid growth mechanism, that makes use of a metal catalyst particle for seeding their growth. The nanowires are grown from thin gold films or by periodically structured gold particles that are designed by substrate conformal imprint lithography.

Dense ensembles of GaP nanowires exhibit a giant form birefringence, i.e., different refractive indices for different polarizations. The modeling of the birefringence as well as the optical experiments for determining the giant birefringence are described in Chapter 3. This birefringence needs to be considered in future devices based on ensembles of nanowires.

The large birefringence of ensembles of vertically aligned GaP nanowires can be modified by adding a thin shell of SiO_2 around the nanowires. The modification of the reflection of light from these structures is studied in Chapter 4 for s- and p-polarization and for the reflection contrast. The peak shift of the reflection contrast of the layers of SiO_2 coated

nanowires is determined for different SiO_2 layer thicknesses. We demonstrate that nanowire layers are very sensitive to small changes in their surrounding. Our measurements set the basis for ultra-sensitive sensors based on nanowire layers.

Due to the preferential growth direction of nanowires in the <111> direction, the growth on (100) substrates results in nanowires aligned in two distinct directions forming an angle of 35° with respect to the substrate. Varying the direction of the nanowires allows for tuning the optical anisotropy of the ensemble. The birefringence of nanowires that are grown on a (100) substrate is explained in Chapter 5. We have determined the birefringence for nanowire layers with different nanowire diameters. We show that for a certain nanowire diameter an ensemble acts as a $\lambda/4$-waveplate.

Layers with thick nanowires form a strongly scattering medium. We have measured the scattering mean free path, i.e., the mean distance between two scattering events of light, in ensembles of GaP nanowires that are grown on either (111) or (100) GaP substrates. We found that layers of nanowires belong to the strongest scattering media reported so far. The measurements of the scattering mean free path and their analysis is described in Chapter 6.

In Chapter 7, we demonstrate that the light coupling efficiency into high index substrates can be increased by layers of nanorods. The light coupling efficiency is increased in a broad spectral and angular range with ensembles of conically shaped nanorods and cylindrically shaped nanorods. This enhanced coupling is due to a gradient of the refractive index from that of air to the index of the substrate. Increasing the light coupling efficiency into high index substrates is of importance for future photovoltaic devices.

In Chapter 8, we demonstrate enhanced optical absorption in arrays of InP nanowires. Arrays of nanowires form a very efficient absorber layer. We have characterized the strong absorption by reflection measurements and finite-difference time-domain simulations.

We end the thesis with Chapter 9, describing possible applications based on nanowires. A gas and bio-sensor using ensembles of nanowires is proposed and a new graded refractive index layer for III/V multi-junction solar cells. Further, a novel design of a base-tapered nanowire based solar cell is proposed in this chapter.

GROWTH OF SEMICONDUCTOR NANOWIRES

We introduce in this chapter the growth of InP and GaP nanowires using the vapor-liquid-solid (VLS) growth mechanism by metal-organic vapor phase epitaxy. The VLS growth mechanism requires a metal catalyst particle. Depending on the catalyst, ordered or disordered ensembles of nanowires can be grown. We describe the growth of disordered ensembles of nanowires from a thin gold film and the growth of ordered arrays of nanowires from nanoparticles structured by substrate conformal imprint lithography. Further, we discuss the nanowire morphology depending on the growth parameters and the substrate.

2.1   Introduction

The vapor-liquid-solid (VLS) growth mechanism of semiconductor nanowires was introduced by Wagner and Ellis in 1964 [26]. For VLS growth, a metal catalyst particle is used to seed the growth of the nanowire underneath it. Since the 1960's the growth of semiconductor nanowires has been studied intensely for group IV nanowires such as silicon [1, 27] and germanium [27], III/V nanowires such as InP [28, 29], GaP [28, 30, 31], and GaAs [32, 33], III/nitrides such as GaN [34, 35], and II/VI nanowires such as ZnO [6, 36]. Using the VLS growth, nanowires can be grown heteroepitaxially, i.e., on a substrate of a different material than that of the nanowire. For example, heteroepitaxial growth of III/V nanowires has been achieved on Si [9]. Non-epitaxial growth of GaP/GaAs nanowires was shown on SiO_2 [37]. Furthermore, core-shell or radial heterostructures such as Ge-Si [38] or GaP-GaAs [39] and axial heterostructures such as InAs wires containing InP segments [5], InP/InAsP [21] or GaP/GaAs wires with multiple heterojunctions [37] can be grown. Dopants can be added during growth leading to pn-junctions in nanowires. These junctions have been realized along the radial [40] and the axial directions [21, 41].

The growth of III/V nanowires has been demonstrated using different epitaxy techniques such as laser-ablation [42], metal beam epitaxy (MBE) [35], and chemical beam epitaxy (CBE) [5]. In this thesis, the nanowire samples are fabricated by metal-organic vapor phase epitaxy (MOVPE) [41].

While for the VLS-growth a metal-catalyst particle is necessary, different catalyst-free growth processes have been also reported such as: a self catalytic VLS mechanism [43], dislocation-driven processes [44, 45], oxide-assisted growth [46, 47], or vapor-solid growth [48, 49]. However, the VLS growth mechanism is the best understood and the one mainly used for the growth of nanowires.

The metal particle that catalyzes the nanowire growth can be deposited using different techniques: via spin-coating from a colloidal solution [50], spraying an aerosol solution, or by deposition of a thin film, which will break up randomly into nanoparticles by heating the sample [51]. Using these approaches, the density and position of the nanowires are not controlled. To control the position, diameter, and density of the nanowires, the gold nanoparticles have to be patterned on the substrate. Different approaches have been reported, such as e-beam lithography [9, 52, 53], gold deposition through an anodic aluminium oxide template [54], nanosphere lithography [55] and nano-imprint lithography [56]. This later technique enables patterning of large surface areas at relatively low cost.

In this thesis, different approaches of designing the catalyst particle are used, depending on the desired optical properties: For achieving high density ensembles of nanowires that lead to strongly birefringent layers (see Chapters 3 and 4), strongly scattering nanowire samples (Chapter 6), and nanowire-antireflection layers (Chapter 7), depositing 0.3 nm of gold as catalyst leads to the best results. While structuring the metal nanoparticles using substrate conformal imprint lithography (SCIL) results in reproducible growth of arrays of nanowires (see Chapter 8).

This chapter is organized as follows. In Section 2.2, we explain the role of the gold catalyst particle in the growth of nanowire layers and its fabrication. The VLS growth mechanism is described in Section 2.3 and the process parameters for the nanowire sam-

ples used in this thesis are given in Section 2.4.

2.2 Gold Catalyst Particle

The gold catalyst particles used for seeding the growth of the nanowires are prepared in two different ways: either a thin gold film is evaporated to seed the growth at random positions with a high nanowire density, or a thicker gold film is structured by SCIL for seeding the growth at predefined positions on the sample. The first method has been used to structure GaP nanowires on top of GaP substrates (Chapters 3-7), while the second method was used for the growth of periodic arrays of InP nanowires on top of InP substrates (Chapter 8).

For achieving high density arrays of nanowires, a thin film of Au with a thickness of 0.3 nm is evaporated on the (111)B (P-terminated) side of the wafer. The electron beam evaporation took place in the evaporation machine Balzac BAK 550 during 6 s. This gold film splits during annealing in the MOVPE reactor into small gold islands with random size distribution and position from which the nanowires grow. Figure 2.1a shows a top-view scanning electron micrograph of nanowires, after a very short period of VLS growth (2 min). This image depicts the splitting of the thin gold film into catalyst particles. Figure 2.1b shows the diameter distribution of the gold particles. The gold film splits into particles with a lognormal diameter distribution with an average diameter of 18.7 nm. Since sites smaller than 10 nm cannot be discerned in the SEM image (Fig. 2.1a), the measured distribution is slightly biased towards larger diameters.
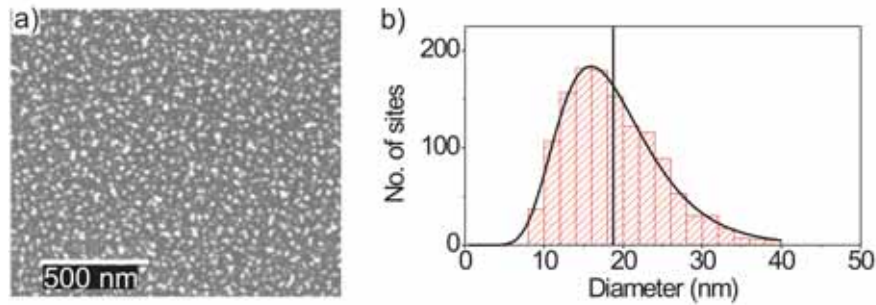
Figure 2.1: a) Top-view scanning electron micrograph and b) diameter distribution of nanowire nucleation sides.

Substrate conformal imprint lithography (SCIL) is used to achieve periodic arrays of gold nanoparticles aligned in a square lattice with a pitch of 513 nm and a diameter of around 90 nm. The SCIL method makes use of a flexible patterned stamp made from poly-di-methylsiloxane (PDMS) [57]. The 2 inch stamp is molded from a silicon master pattern which contained arrays of holes and was fabricated using e-beam lithography.

The composite stamp is molded from the master following the procedure described in Refs. [57, 58], which yields a soft PDMS stamp with protruding pillars. The developed nano-imprint process has the following steps illustrated in Figure 2.2. A 100 nm thick layer of poly-methylmethacrylate (PMMA) is applied by spin coating on 2 inch (111)B InP wafers, after which the wafers are baked on a hotplate at 150 °C for 15 minutes. Next, silica-based sol-gel imprint resist is applied by spin coating over the PMMA layer (Fig. 2.2a) [59]. After the spin coating process the stamp is applied on the sol-gel resist. The features in the stamp are filled with the sol-gel resist by capillary forces. The water in the sol-gel diffuses in the stamp to form a solid silica glass (Fig. 2.2b). Finally, the stamp is carefully removed from the patterned silica layer by peeling. The remaining residual sol-gel layer between the bottom of the features and the PMMA layer is removed by a CF_4 based reactive ion etch (RIE) (Fig. 2.2c). Then oxygen RIE is used to transfer the pattern of the sol-gel layer into the underlying PMMA layer (Fig. 2.2d). We adjust the time of the oxygen etch such that a short over etch is applied in the III/V material in order to remove any residual PMMA. A chemical etch process in a 1% HF solution removes the formed oxide on the semiconductor surface, after which a thin (6 nm) gold layer is deposited onto the patterned sol-gel/PMMA surface by perpendicular evaporation (Fig. 2.2e). The lift-off process is performed in acetone, which dissolves the PMMA layer and releases the silica and gold metal which are suspended by PMMA. This process leaves precisely placed gold disks of controlled diameter and thickness on the semiconductor substrate (Fig. 2.2f). Since the lift-off process leaves residues on the substrate besides the patterned arrays, which are shown in Figure 2.3, the wafer is cleaned in a piranha solution ($H_2SO_4 : H_2O_2 : H_2O$, 5:1:1) for 30 s before the nanowire growth is started.

2.3 VLS-Growth Mechanism

The VLS growth mechanism of group III/V nanowires is schematically depicted in Figure 2.4a and 2.4b for the growth of GaP nanowires and consists of three basic steps: First, the substrate is placed in a reactor, where it is heated in a group V atmosphere (I). The gold particles melt and form liquid droplets. This is achieved by dissolving the semiconductor material from the substrate to form an alloy of group III and gold with a reduced melting temperature as compared to pure gold. In this stage, the diameter of the gold-group III particle increases. When the desired growth temperature is reached, the group III precursor is added into the reactor. The droplet adsorbs more group III material until saturation occurs (II). The liquid droplet becomes in equilibrium with the solid phase of the semiconductor and nucleation occurs. In the third stage, the semiconductor crystal grows at the solid/liquid interface (III). After growth, the reactor is cooled down in a group V atmosphere (IV). Steps A-D in Figure 2.4b correspond to steps I-III in Figure 2.4a and are related to the VLS growth mechanism. Simultaneously, the precursors can be adsorbed at the substrate or nanowire surface, which leads to side wall growth of the wire (Fig. 2.4b, E-G), or to layer growth on the substrate (H).

The side-wall growth of the nanowires is not catalyzed by the gold particle, therefore at low temperatures in the MOVPE reactor the sidewalls grow at a much slower rate than
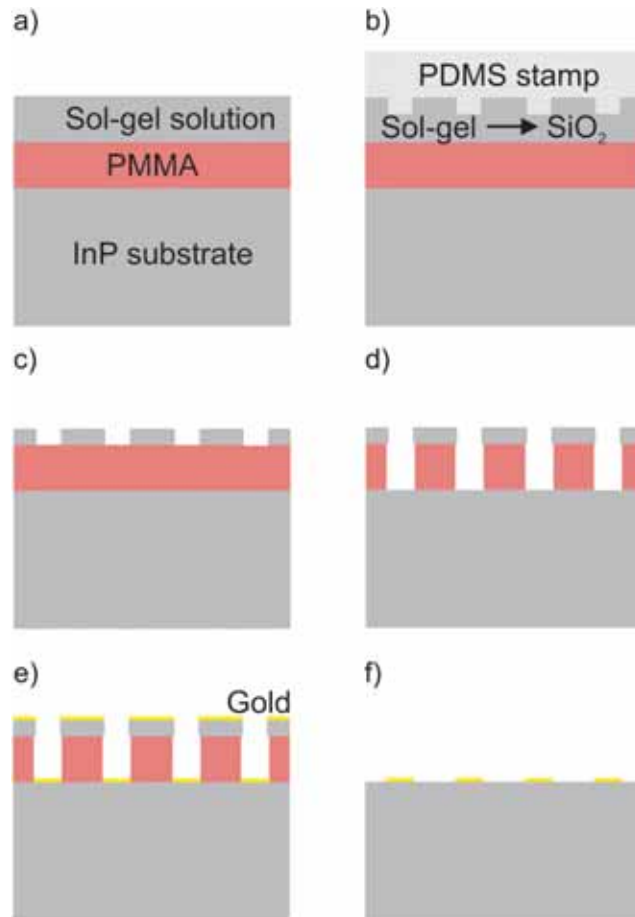
Figure 2.2: Schematic of the different steps of SCIL. a) The InP substrate is coated with PMMA and a sol-gel solution. b) The PDMS stamp is pressed into the sol-gel solution and the sol-gel reacts to SiO_2. c) Using a CF_4 plasma etch, the pattern is transferred deeper into the SiO_2. d) The pattern is transferred into the PMMA by an O_2 plasma etch. e) Gold is evaporated onto the pattern. f) After the lift-off process, the gold stays at the predefined positions.
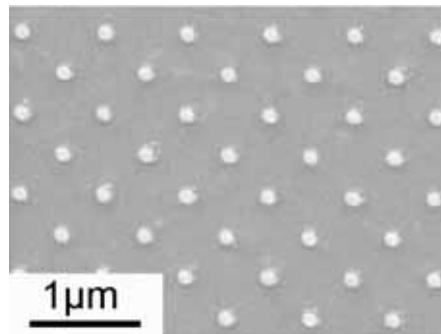
Figure 2.3: Top-view scanning electron micrograph of the gold nanoparticles patterend by SCIL before cleaning in a piranha solution.
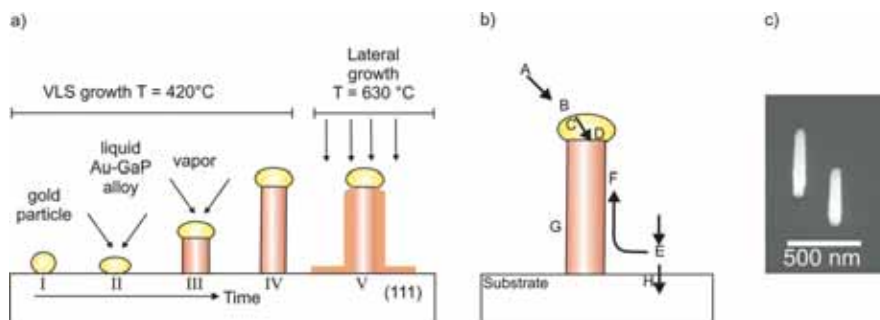
Figure 2.4: a) Vertically aligned cylindrical nanowires grow at a temperature of 420 °C. The length of the nanowires is defined by the growth time. Increasing the diameter of the nanowires is possible by switching to the lateral growth mode occuring at a higher temperature. b) Schematic drawing of the relevant chemical processes in the nanowire growth. (A) The precursors are transported through the gas phase (B) and dissociate on the catalytic particles or on the nanowire surface. (C) The reactants diffuse through the metal particle. (D) The semiconductor lattice is formed at the liquid-solid interface. (E) The precursor molecules are adsorbed on the substrate or on the nanowire surface. (F) Surface diffusion. (G) Film growth on the nanowire sidewall. (H) Film growth on the substrate surface. c) Scanning electron micrograph of GaP nanowires grown for 30 s at a temperature of 550 °C.

the VLS growth. Figure 2.4c shows GaP nanowires grown for 30 s at a temperature of 550 °C. However, at higher temperatures, e.g., 630 °C, the sidewall growth becomes more favorable and the diameter of the nanowires increases (step V in Fig. 2.4a). A growth temperature between 420 °C and 630 °C allows fabricating conically shaped nanowires, as both VLS growth and side-wall growth occur simultaneously. By varying the temperature, both growth mechanisms can be adjusted so that nanowires with a certain tapering angle can be grown (Fig. 2.5) While the tapering angle can be controlled, the diameter and length of the nanowires are correlated. Figure 2.5b shows nanowires grown for 1200 s at a temperature of 580 °C.
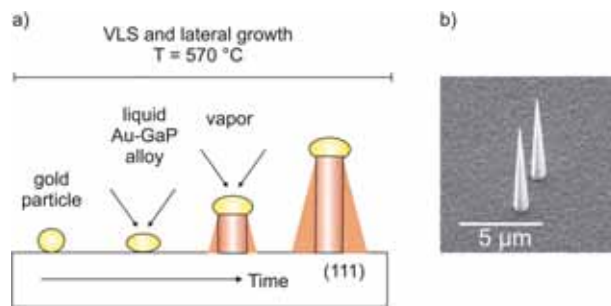
Figure 2.5: a) At a temperature of 570 °C, both VLS and lateral growth occur simultaneously resulting in tapered or conical nanowires. b) Scanning electron micrograph of tapered nanowires grown for 1200 s at a temperature of 580 °C.

Considering that nanowires grow preferentially into the [111] direction [60], the orientation of the nanowires with respect to the substrate can be varied by growing them on substrates with different crystallographic orientation. On a (100) substrate, the nanowires grow preferentially with an angle of 35° with respect to the substrate surface according to the <111> direction. Figure 2.6a displays a schematic representation of the nanowire growth on a (100) GaP substrate. The inset of this figure shows a SEM image of a nanowire sample grown for 1020 s at 420 °C and for 200 s at 630 °C. The SEM image clearly reveals the preferential growth direction of the wires. The <111> directions on the (100) plane are defined in Figure 2.6b. In the inset of Figure 2.6b, a tilted-view SEM image taken under an angle of 30° is shown. The SEM image shows that the nanowires grow preferentially in the two <111>B directions of the four possible <111> directions. The growth into the <111>B direction is favored over the <111>A direction as the surface free energy of the liquid-solid interface is minimized [61].

2.4 Recipes for Nanowire Growth

Here, the recipes for the growth of GaP nanowires on single and double side polished (111) and (100) GaP substrates and on an AlInP layer on a GaAs (100) substrate are given. We also give the recipe for the growth of InP/InAsP/InP nanowires on (111) InP substrates. First,
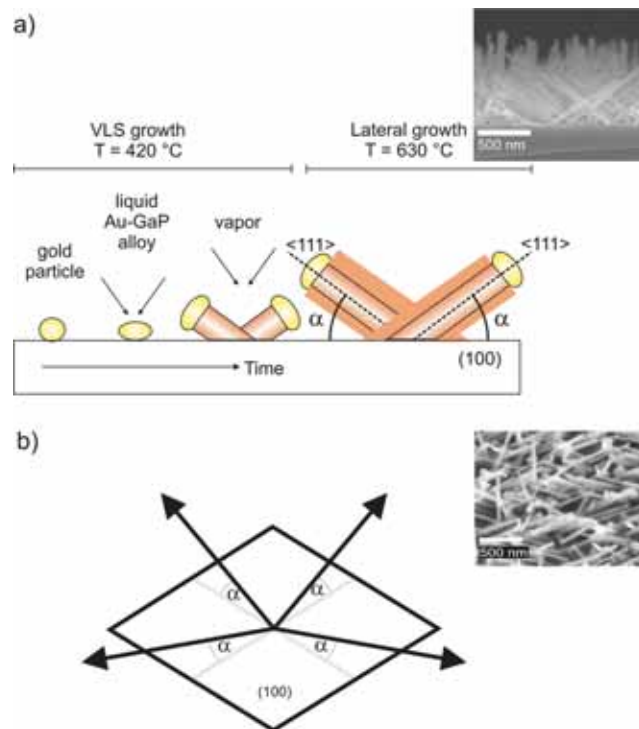
Figure 2.6: a) The nanowire growth is catalysed by a gold particle deposited on a (100) semiconductor substrate. Cylindrical nanowires grow under an angle of 35° with respect to the substrate at a temperature of 420 °C and the length of the nanowires is defined by the growth time. Increasing the diameter of the nanowires is possible by switching to the lateral growth mode at 630 °C. The inset shows a cross-sectional SEM image of nanowires grown for 1020 s at 420 °C and for 200 s at 630 °C. b) Schematic of the <111> directions on a (100) plane. The angle α correspond to 35°. The inset shows a tilted view SEM image of the same sample as in a).

the pretreatment of the substrate is explained for single and double side polished GaP substrates and single side polished InP substrates. Next, the deposition of the Au catalyst is described and the nanowire growth parameters are given.

- GaP Substrates
    - Single Side Polished (111) GaP Substrate
        * Cleaning of the substrates in an anisotropic etching step in HNO_3:HCl:H_2O (2:3:3) at 80 °C for 2 min. This etching step is necessary to remove any native oxides that would hinder the nanowire growth.
        * Evaporation of 0.3 nm Au on the polished (111)B (P-terminated) side of the substrate. This gold film acts as catalyst for the nanowire growth and splits into particles during annealing in the low pressure (50 mbar) MOVPE reactor (Aixtron200).
        * Nanowire growth in MOVPE reactor using trimethylgallium (TMG) and phosphine (PH_3) as precursors. A total flow of 6 liters/min was used, with hydrogen as carrier gas. The growth temperatures and times are given in Table 2.1 and are chosen depending on the desired dimensions of the nanowires. To achieve cylindrical shaped nanowires, the temperature was 420 °C. After the desired length of the nanowires was reached, the temperature was increased to 630 °C for side-wall growth for varying the diameter of the nanowires. After growth, the samples were cooled down in a PH_3-containing atmosphere.
    - Double-Side Polished (111) GaP Substrate
        * Protection of the backside of the double-side polished GaP, with a layer of 500 nm of SiO_2 deposited on the (111)A (Ga-terminated) side by plasma-enhanced chemical vapor deposition (PECVD) at a temperature of 300 °C.
        * Cleaning step in HNO_3:HCl:H_2O (2:3:3) at 80 °C for 2 min.
        * Evaporation of 0.3 nm Au on the polished (111)B (P-terminated) side of the substrate
        * Nanowire growth in MOVPE reactor for temperatures and times given in Table 2.1 depending on the desired dimensions of the nanowires. Conically shaped nanowires are grown at a temperature of 570 °C for obtaining VLS and side-wall growth simultaneously. After growth, the samples were cooled down in a PH_3-containing atmosphere.
    - Double Side Polished (100) GaP Substrate
        * Deposition of a layer of 500 nm of SiO_2 on one side of the substrate by PECVD at a temperature of 300 °C.
        * Cleaning step in HNO_3:HCl:H_2O (2:3:3) at 80 °C for 2 min.
        * Evaporation of 0.3 nm Au on the polished GaP side of the substrate.
        * Nanowire growth in MOVPE reactor for temperatures and times given in Table 2.1 depending on the desired dimensions of the nanowires. After growth, the samples were cooled down in a PH_3-containing atmosphere.

- AlInP layer on (100) GaAs Substrates

  - Growth of 30 nm AlInP on a GaAs substrate followed by a GaAs protection layer.

  - Etching of GaAs top layer.

  - Spin coating of colloids with a diameter of 10 nm.

  - Nanowire growth in MOVPE reactor for temperatures and times given in Table 2.1 depending on the desired dimensions of the nanowires. Conically shaped nanowires are grown at a temperature of 570 °C for obtaining VLS and side-wall growth simultaneously. After growth, the samples were cooled down in a PH_3-containing atmosphere.

- InP Substrates

  - Annealing of epi-ready InP substrates for 10 min at a temperature of 550 °C to remove the not-specified epi-layer.

  - Patterning of the gold catalyst by SCIL.

  - Removal of undesired organic residues of the SCIL process, by a cleaning step in piranha etch at a temperature of 20 °C for 30 s.

  - Annealing step of the InP substrates covered with the gold nanoparticles for 10 min at a temperature of 550 °C in a PH_3-atmosphere inside the MOVPE.

  - InP nanowire growth in MOVPE reactor using trimethylindium (TMIn) and phosphine (PH_3) as precursors at a temperature of 420 °C. Along the axial direction of the InP nanowire, an InAsP heterostructure is grown by adding arsine (AsH_3) into the MOVPE reactor. After growth, the samples were cooled down in a PH_3-containing atmosphere.

Table 2.1 summarizes the parameters used for growing the nanowire samples described in this thesis. The parameters include the orientation and material of the substrate, the growth temperature, growth time, resulting diameter and length of the nanowires, and the chapter in which the measurements on the sample are described.

2.5 Conclusions

We have described in this chapter the growth of GaP nanowires on GaP substrates and on AlInP layers and of InP/InAsP/InP nanowires on InP substrates using the vapor-liquid-solid growth mechanism by metal-organic vapor phase epitaxy. GaP nanowires are grown from thin gold films used as catalyst, either on (111) substrates, resulting in vertically aligned nanowires, or on (100) substrates resulting in a majority of nanowires grown with an angle of 35° with respect to the substrate. The gold catalysts for the InP nanowire growth are patterned using substrate conformal imprint lithography resulting in periodic arrays of vertically aligned heterostructured InP/InAsP/InP nanowires.

Table 2.1: Growth parameters of the samples measured in this thesis including substrate, growth temperature, growth time, length, diameter and chapter where the sample is described.

Sample	Substrate	Growth temperature [$^\circ$C]	Growth time [s]	Length [μm]	Diameter [nm]	Chapter
I	GaP(111)	420/630	1020/350	1.26±0.1	40±25	3, 4
II	GaP(111)	420	1020	1.31±0.1	21.5±3.5	3
III	GaP(111)	420/630	1020/100	1.27±0.1	26±4.5	3
IV	GaP(111)	420/630	1020/200	1.3±0.1	31±5.5	3
V	GaP(111)	420/630	1080/200	1±0.1	33±9	4
VI	GaP(100)	420	1020	1.2±0.1	22±4	5
VII	GaP(100)	420/630	1020/200	1.3±0.1	31±3	5
VIII	GaP(100)	420/630	1020/500	1.4±0.2	43±10	5
IX	GaP(100)	420/630	1020/800	1.5±0.2	72±19	5
X	GaP(111)	420	1020	1±0.2	12±4	6
XI	GaP(111)	420/630	1020/200	0.92±0.1	30±5	6
XII	GaP(111)	420/630	1020/800	1.1±0.2	59±13	6
XIII	GaP(111)	420/630	1020/1100	1.1±0.2	81±16	6
XIV	GaP(111)	420/630	1020/1400	1.1±0.2	90±16	6
XV	GaP(111)	420/630	1020/1700	1.1±0.2	110±18	6
XVI	GaP(100)	420/630	1020/1700	1.6±0.2	118±19	6
XVII	GaP(111)	570	600	0.18±0.025	tapered	7
XVIII	GaP(111)	420	320	0.2±0.05	27±5	7
XIX	InP(111)	420	1800/10/1800	3±0.2	tapered	8
XX	InP(111)	420	5400/50/5400	5±0.2	tapered	8
XXI	InP(111)	420	7200/50/7200	7.5±0.5	tapered	8
XXII	AlInP/GaAs(100)	570	180	-	tapered	9

BIREFRINGENCE OF VERTICALLY ALIGNED GaP NANOWIRES

We present the first experimental demonstration of broadband birefringence of dense ensembles of vertically aligned nanowires. In particular, we investigate GaP nanowires grown on (111) substrates. The birefringence of the nanowire layer is obtained by fitting measurements of the reflection contrast with a transfer-matrix formalism based on Jones calculus and compared to Maxwell-Garnett effective medium theory.

3.1 Introduction

Light travels in a medium with a phase velocity reduced from the speed of light in vacuum by the refractive index of the medium. If the medium is isotropic, light experiences a refractive index that is independent on the angle of incidence or its polarization. Light impinging with an angle larger than $0°$ at the interface between two different media, is refracted due to the contrast in refractive indices. This basic law of optics was first formulated by Snell in 1621 [62].

If a medium is formed by subwavelength anisotropic scatterers and if these scatterers are aligned along certain directions, the homogenization performed by any effective medium model leads to the permittivity tensor

$$\epsilon = \begin{pmatrix} \epsilon_1 & 0 & 0 \\ 0 & \epsilon_2 & 0 \\ 0 & 0 & \epsilon_3 \end{pmatrix},$$ (3.1)

with ϵ_1, ϵ_2, and ϵ_3 the effective medium permittivities along the three principal axes. A medium with this characteristic is called birefringent, as light propagating through it experiences different refractive indices or has different phase velocities depending on its polarization state. The permittivity tensor is diagonal, so that the light polarized along one of the three principal axes is not affected by the permittivity along the other axes. If $\epsilon_1 \neq \epsilon_2 \neq \epsilon_3$ the medium is called biaxial, whereas if $\epsilon_1 = \epsilon_2 \neq \epsilon_3$, we have an uniaxial medium [63]. In uniaxial media ϵ_1 and ϵ_2 are usually referred to as the ordinary permittivity and ϵ_3 is called the extraordinary permittivity.

The origin of the anisotropy can be of different nature: A medium is optically anisotropic either due to an anisotropy in the microscopic structure, i.e., natural birefringence, or because it is formed by macroscopic subwavelength anisotropic scatterers, i.e., form birefringence. Natural birefringent materials such as calcite and quartz are well known and used in optical components. Semiconductor nanowires are anisotropic scatterers. As we have seen in Chapter 1, scattering of light by single nanowires depends strongly on the polarization of the incident light. The scattering cross-section for light polarized parallel to the long axis of the nanowire is larger than for light polarized perpendicular to this axis. Moreover, nanowires can be grown epitaxially on crystalline substrates along well-defined crystallographic directions. If this direction of growth is unique, layers of vertically aligned nanowires form an uniaxial birefringent material with an effective permittivity given by the tensor

$$\epsilon = \begin{pmatrix} \epsilon_o & 0 & 0 \\ 0 & \epsilon_o & 0 \\ 0 & 0 & \epsilon_e \end{pmatrix},$$ (3.2)

where ϵ_o represents the effective ordinary permittivity or the permittivity that light polarized perpendicular to the long axis of the nanowires experiences, and ϵ_e refers to the effective extraordinary permittivity or the permittivity for light polarized parallel to the nanowire axis. The same definition holds for the refractive indices of the layer: The ordinary refractive index n_o corresponds to the refractive index for light polarized perpendicular to

the nanowire long axis, while n_e describes the refractive index for light polarized parallel to this axis. Figure 3.1 shows a scanning electron micrograph of vertically aligned GaP nanowires grown on a (111) GaP substrate together with an illustration of the directions of the ordinary and extraordinary refractive indices. The birefringence is due to the different boundary conditions for light polarized parallel or perpendicular to the nanowire axis. For light polarized parallel to the nanowire axis, the tangential component of the electric field is continuous, while for light polarized perpendicular to the nanowire axis, the normal component of the displacement field is continuous.
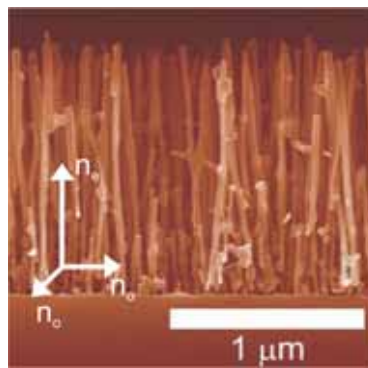
Figure 3.1: Scanning electron micrograph of ensembles of GaP nanowires grown on a (111) substrate. The directions of the refractive indices are indicated with the arrows.

Form birefringence has been studied extensively in nanostructured materials like porous silicon [64–70], porous group II/VI [71] and group III/V semiconductors [72], silicon photonic crystals [73], and carbon nanotubes [74–76]. In this thesis, the birefringence of ensembles of semiconductor nanowires is described.

This chapter is organized as follows. In Section 3.2 the effective refractive indices of the nanowire layer are defined using Maxwell-Garnett effective medium theory. Further, the reflection and transmission amplitude coefficients at the interface of an isotropic and an anisotropic layer are derived. Using the effective refractive indices of the layer and the reflection and transmission coefficients, the transfer-matrix method based on Jones calculus is introduced for modeling the reflection from nanowire layers. In Section 3.3 the birefringence of nanowire layers is determined experimentally by fitting reflection measurements with the transfer-matrix method. A strong emphasis is put on analyzing the reflection contrast, i.e., the ratio of reflected light passing through a crossed and parallel aligned polarizer and analyzer. From these experiments and fits, the birefringence parameter is determined over a broad wavelength range.

3.2 Theoretical Background

For modeling the reflection of light from a dense layer of vertically aligned nanowires, several aspects need to be considered: First, a model describing the effective refractive

indices of the nanowire layer has to be defined. Second, the reflection and refraction of light at the interface between an isotropic medium, such as air or the GaP substrate, and the anisotropic nanowire layer, has to be calculated. Last, the transfer-matrix for the three-layer-system consisting of air, the birefringent nanowire layer, and the GaP substrate has to be determined.

3.2.1 Effective Medium Theory

Before we determine the effective refractive indices for s- and p-polarization, we define the ordinary and extraordinary refractive indices. The directions of the two polarization vectors of light experiencing these refractive indices are schematically depicted in Figure 3.1; the ordinary refractive index n_o is the refractive index for light polarized perpendicular to the nanowire elongation, while the extraordinary refractive index n_e is the refractive index for polarization parallel to the nanowire axis. In a first approximation, the nanowires can be considered as infinitely long cylinders, because their length is longer than the wavelength. Kirchner *et al.* found that the Maxwell-Garnett effective medium theory [77] describes n_o of a medium consisting of infinitely long cylinders with a diameter and a distance between cylinders smaller than the wavelength of light [25]. The volume average of the two media forming the effective medium describes n_e. For the case of GaP nanowires surrounded by a dielectric, we have:

$$n_e = \sqrt{f_{GaP} \cdot n_{GaP}^2 + (1 - f_{GaP}) \cdot n_d^2},$$ (3.3a)

$$n_o = \sqrt{n_d^2 \cdot \left(1 + \frac{2 f_{GaP} \alpha_1}{1 - f_{GaP} \alpha_1}\right)},$$ (3.3b)

where n_d and n_{GaP} are the refractive indices of the dielectric and GaP respectively, f_{GaP} is the GaP filling fraction of the nanowire layer and α_1 is the depolarization factor $\alpha_1 = (n_{GaP}^2 - n_d^2)/(n_{GaP}^2 + n_d^2)$.

Maxwell-Garnett effective medium theory is not symmetric to the interchange of the permittivity between the scatterers and the surrounding medium. In other words, the effective Maxwell-Garnett permittivity of semiconductor nanowires in air is not the same as that of air pores in a semiconductor matrix. To illustrate this asymmetry we have plotted in Fig. 3.2 the birefringence parameter, defined as

$$\Delta n = n_e - n_o = \sqrt{\epsilon_e} - \sqrt{\epsilon_o},$$ (3.4)

as a function of the semiconductor filling fraction for direct (nanowires in air) and inverse (air pores in a semiconductor matrix) structures. The solid and dashed red curves in Fig. 3.2 correspond to a direct and inverse medium respectively, containing a semiconductor of permittivity 16 and air. The solid and dashed black curves represent the birefringence of similar direct and inverse media with a semiconductor of permittivity 4 and air. In general, the birefringence increases as the permittivity of the semiconductor gets larger and an ensemble of nanowires has a larger birefringence than a similar medium
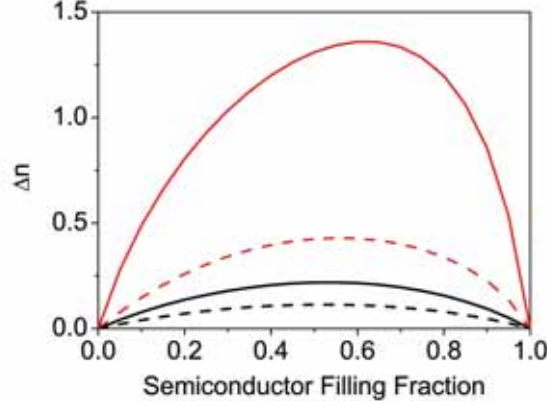
Figure 3.2: Birefringence parameter calculated with the Maxwell-Garnett effective medium theory for four different anisotropic media formed by a semiconductor and air as a function of the semiconductor filling fraction. The solid black and red curves represent the birefringence for semiconductor nanowires with a permittivity of 4 and 16 respectively, in air. The dashed black and red curves correspond to the birefringence in samples of pores in a semiconductor matrix for the same values of the permittivity.

of nanopores. For comparison; the optical birefringence of quartz is 0.042 while the birefringence of calcite is 0.17 at a wavelength of 589.3 nm [78].

The effective refractive indices for s- and p-polarization can be derived from the ordinary and extraordinary refractive indices. For s-polarization, the electric field is perpendicular for any angle of incidence to the long axis of the nanowires. Therefore, the refractive index for s-polarization equals the ordinary refractive index, $n_s = n_o$ [63]. For normal incidence, the electric field is perpendicular to the nanowire axis for all polarizations. As the angle of incidence onto the sample is varied, the effective refractive index for p-polarized light increases due to the larger projection of the electric field along the nanowire axis. The phase velocity of p-polarized light propagating in a birefringent medium and therefore the refractive index for p-polarized light in a birefringent medium is defined as a function of the internal angle θ'_p and depends on the extraordinary and ordinary refractive index [79]

$$\frac{1}{v_p} = n_p = \left(\frac{\cos^2\theta'_p}{n_o^2} + \frac{\sin^2\theta'_p}{n_e^2}\right)^{-0.5}. \tag{3.5}$$

A derivation of Equation (3.5) can be found in Ref. [63]. From Equation (3.5) and Snell's law at the interface between a dielectric and the birefringent medium

$$n_d \sin\theta = n_p \sin\theta'_p, \tag{3.6}$$

with n_d the refractive index of the dielectric and θ the external angle of incidence, the angle-dependent refractive index for p-polarization is given in terms of the ordinary and

extraordinary refractive indices by [66]

$$n_{\mathrm{p}} = \sqrt{n_{\mathrm{o}}^2 + \frac{n_{\mathrm{e}}^2 - n_{\mathrm{o}}^2}{n_{\mathrm{e}}^2} \cdot \sin^2 \theta}. \tag{3.7}$$

3.2.2 Reflection and Refraction of Light at the Interface between Isotropic and Uniaxial Media

Light impinging on the interface between two different media is reflected and refracted depending on its polarization. The reflection and transmission of light at the interface between two isotropic media is well known since Fresnel derived in the 1820s the amplitude reflection and transmission coefficients. To derive the reflection and transmission coefficients at the interface between isotropic and uniaxial media, s- and p-polarized light need to be considered separately. In this section, refraction of light at the interface between an isotropic and an anisotropic medium is explained using equifrequency surfaces in k-space. Further, the amplitude reflection and transmission coefficients for p-polarized light are derived. These coefficients differ from the Fresnel coefficients at the interface of two isotropic media.

Refraction of light in a birefringent layer depends strongly on its polarization state. As explained before, the electric field of s-polarized light is perpendicular to the nanowire elongation for any angle of incidence and the refractive index for s-polarized light equals the ordinary refractive index. Therefore, s-polarized light travels in the birefringent nanowire layer as if the layer was isotropic. In Figure 3.3a the equifrequency surfaces for s-polarized light in an isotropic dielectric and in the nanowire layer are represented. The equifrequency surface describes the relation between the wavevectors k_{x} and k_{z}, i.e., the wavevector of light parallel and normal to the interface between the two media, at a fixed frequency. For a plane wave with a **k**-vector of components (k_{x}, k_{z}) propagating in an isotropic medium the equifrequency surface is given by $k_{\mathrm{x}}^2 + k_{\mathrm{z}}^2 = \frac{\omega^2}{c^2} n^2$, which represents a circle of radius $\frac{\omega}{c} n$. The refractive index of air and the nanowire film for s-polarization are angle independent; therefore a wave propagating in these media is described by circular equifrequency surfaces (Fig. 3.3a). Since the interface separating both media is translational invariant in the xy-plane, the wave vector parallel to the interface must be conserved. Therefore, if we know the incident wavevector **k**$_{\mathrm{i}}$ at the interface, the refracted wave vector, **k**$_{\mathrm{r}}$ in the nanowire film is determined by the conservation of the component parallel to the interface. This conservation law is indicated by the dotted line in Figure 3.3a. The direction of the group velocity, $v_{\mathrm{s}}^{\mathrm{g}}$ is normal to the tangent of the equifrequency surface, which is indicated by the dashed line in Figure 3.3a. Therefore, the group velocity and the **k**-vector, thus the phase velocity, in the nanowire film are co-linear for s-polarized light.

This situation is different for p-polarized light. The electric field for this polarization has a component parallel and a component perpendicular to the nanowire elongation, resulting in a refractive index that depends on both the ordinary and the extraordinary refractive index. Due to the dependence of the refractive indices for p-polarized light on the angle of incidence (see Eq. 3.7), the equifrequency surface forms an ellipse. The

refracted wave vector is again defined by the conservation of its component parallel to the surface and the group velocity direction is normal to the tangent of the ellipse. As illustrated in Figure 3.3c, the directions of the wave vector and the group velocity are not identical for p-polarized light. The angles for the wave vectors, $\theta'_{s,p}$ and group velocities $\theta^g_{s,p}$ for s- and p-polarized light are schematically drawn in Figure 3.3b and d, respectively.
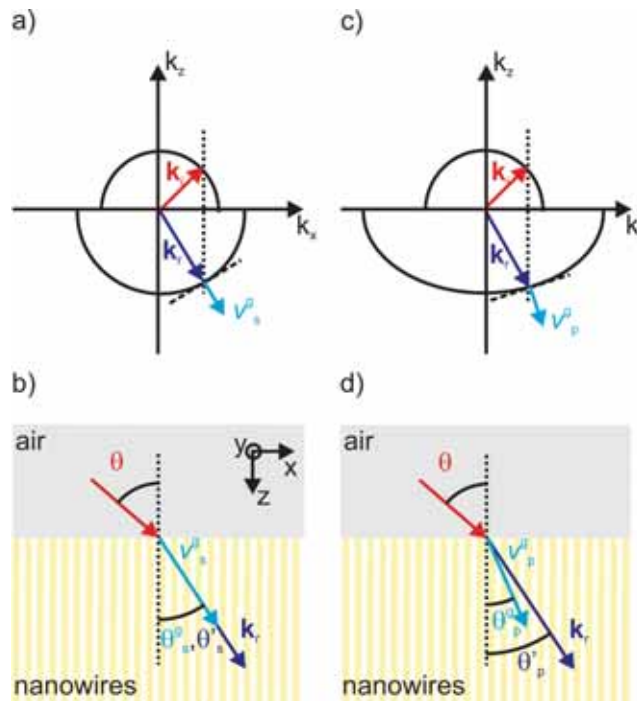
Figure 3.3: Equifrequency surfaces for a) s-polarized and c) p-polarized light incident from an isotropic medium, into an anisotropic medium, e.g., the nanowire layer. The refracted wave vector $\mathbf{k_r}$ is given by the conservation of the parallel component of the wave vector to the interface, while the group velocity $v^g_{s,p}$ is normal to the tangent of the equifrequency surface. b) and d) schematic diagrams of the refracted wave vector and the group velocity for s- and p-polarized light at the air-nanowire interface, respectively.

Now that we have described how light is refracted at the interface between isotropic and anisotropic media, we can determine the reflection and transmission coefficients. We derive these coefficients at the interface between a dielectric and an anisotropic medium by applying the electromagnetic boundary conditions and in particular by the continuity of the tangential component of the electric and magnetic field at the interface between two media. Figure 3.4a illustrates the reflection and transmission of p-polarized light with the wave vector $\mathbf{k_i}$ and the angle of incidence θ with respect to the normal of the interface.

The continuity of the tangential component of the electric field at the interface, $z = 0$, requires that the components of the incident, transmitted, and reflected fields along the

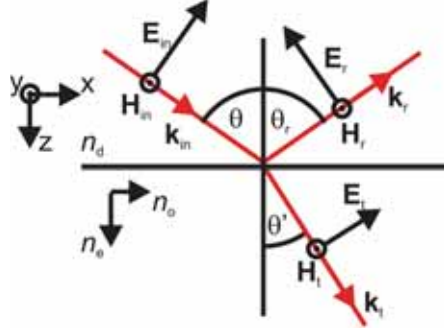**Figure 3.4:** Reflection and transmission of p-polarized light incident with an angle θ at the interface between a dielectric with the refractive index n_d and the nanowire layer with ordinary and extraordinary refractive indices.

x-direction satisfies the equation

$$E_{\text{in,x}} + E_{\text{r,x}} = E_{\text{t,x}}, \tag{3.8}$$

i.e., the superposition of the incident and reflected field equal the transmitted field at the interface. Analogously, the continuity of the tangential component of the magnetic field requires

$$H_{\text{in,y}} + H_{\text{r,y}} = H_{\text{t,y}}. \tag{3.9}$$

To obtain an equation for the x-component of the electric field using the continuity of the magnetic field, we need to relate the y-component of the magnetic field to the x-component of the electric field. This relation is provided by Ampère's law

$$\nabla \times \mathbf{H} = -i\mathbf{k} \times \mathbf{H} = \frac{\partial \mathbf{D}}{\partial t}, \tag{3.10}$$

with

$$D = \begin{pmatrix} \epsilon_{\text{o}} & 0 & 0 \\ 0 & \epsilon_{\text{o}} & 0 \\ 0 & 0 & \epsilon_{\text{e}} \end{pmatrix} \begin{pmatrix} E_{\text{x}} \\ 0 \\ E_{\text{z}} \end{pmatrix}, \tag{3.11}$$

for p-polarized light. Equations (3.10) and (3.11) result in

$$H_{\text{y}} = -\frac{1}{k_{\text{z}}} \omega \epsilon_{\text{o}} E_{\text{x}}. \tag{3.12}$$

The y-component of the magnetic field in the dielectric is given by

$$H_{\text{in,r,y}} = -\frac{1}{k_{\text{in,r,z}}} \omega \epsilon_{\text{d}} E_{\text{in,r,x}} \tag{3.13}$$

and in the anisotropic medium by

$$H_{\text{t,y}} = -\frac{1}{k_{\text{t,z}}} \omega \epsilon_{\text{o}} E_{\text{t,x}}, \tag{3.14}$$

with $k_{\mathrm{in,r,z}} = -k_{\mathrm{r,z}} = k_{\mathrm{in,z}}$. From Equations (3.9), (3.13),and (3.14) it follows

$$\frac{1}{k_{\mathrm{in,z}}} \omega \epsilon_{\mathrm{d}} (-E_{\mathrm{i,x}} + E_{\mathrm{r,x}}) = \frac{1}{k_{\mathrm{t,z}}} \omega \epsilon_{\mathrm{o}} E_{\mathrm{t,x}}. \tag{3.15}$$

To determine the amplitude reflection coefficient, $r_{\mathrm{p}} = \frac{E_{\mathrm{r,x}}}{E_{\mathrm{i,x}}}$, we replace $E_{\mathrm{t,x}}$ in Equation (3.15) by Equation (3.8). Using $k_{\mathrm{in,z}} = \frac{2\pi}{\lambda} n_{\mathrm{d}} \cos\theta$ and $k_{\mathrm{t,z}} = \frac{2\pi}{\lambda} n_{\mathrm{p}} \cos\theta_{\mathrm{p}}'$ and solving for the reflection coefficient, r_{p}, results to

$$r_{\mathrm{p}} = \frac{n_{\mathrm{o}}^2 \cos\theta - n_{\mathrm{d}} n_{\mathrm{p}} \cos\theta_{\mathrm{p}}'}{n_{\mathrm{o}}^2 \cos\theta + n_{\mathrm{d}} n_{\mathrm{p}} \cos\theta_{\mathrm{p}}'}. \tag{3.16}$$

The transmission coefficient can be deduced using Equation (3.15) by replacing $E_{\mathrm{r,x}}$ with Equation (3.8), which results in

$$t_{\mathrm{p}} = \frac{E_{\mathrm{t,x}}}{E_{\mathrm{i,x}}} = \frac{2 n_{\mathrm{d}} n_{\mathrm{p}} \cos\theta_{\mathrm{p}}'}{n_{\mathrm{d}} n_{\mathrm{p}} \cos\theta_{\mathrm{p}}' + n_{\mathrm{o}}^2 \cos\theta}. \tag{3.17}$$

For s-polarization, the amplitude reflection and transmission coefficients can be obtained similarly. The reflection and transmission coefficients for s-polarized light are given by

$$r_{\mathrm{s}} = \frac{n_{\mathrm{d}} \cos\theta - n_{\mathrm{s}} \cos\theta_{\mathrm{s}}'}{n_{\mathrm{d}} \cos\theta + n_{\mathrm{s}} \cos\theta_{\mathrm{s}}'}, \tag{3.18}$$

and

$$t_{\mathrm{s}} = \frac{2 n_{\mathrm{d}} \cos\theta}{n_{\mathrm{d}} \cos\theta - n_{\mathrm{s}} \cos\theta_{\mathrm{s}}'}. \tag{3.19}$$

These coefficients are the same as the amplitude coefficients at the interface between two isotropic media.

To conclude, we have shown how light is refracted at the interface between isotropic and anisotropic media and we have deduced the reflection and transmission coefficients at the interface. In the next section, we describe how to treat more than one interface in layered media.

3.2.3 Jones Calculus for Anisotropic Layers

The reflection from a layer of nanowires can be modeled with the Jones calculus for a three layer system consisting of air, nanowires and the substrate [80]. The Jones calculus is based on Jones vectors, the transmission and reflection coefficients at the interfaces, and the phase changes in air and in the nanowire layer. In this section, we deduce the intensity of the light reflected by the three layer system and explain the reflection contrast by using Jones calculus.
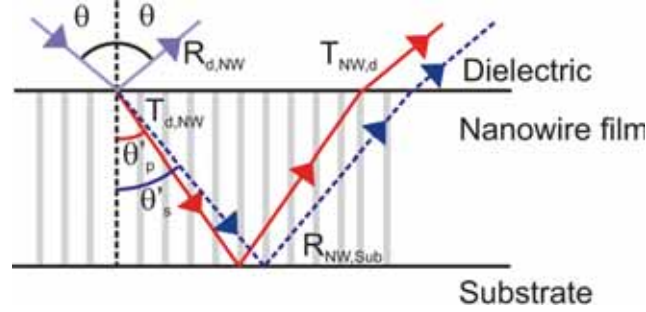
Figure 3.5: Optical path in the nanowire structure. The blue dotted lines indicate the path of s-polarized light, the red solid curves refer to the p-polarized light. The angles θ'_s and θ'_p are the angles of refraction for s- and p-polarized light, respectively. The incident light is polarized at an angle of 45° with respect to the plane of incidence defined by the **k**-vector and the normal to the surface.

Figure 3.5 illustrates the optical path of light impinging on the nanowire layer with a certain angle of incidence θ. The polarization of the incident light is assumed to form an angle of 45° with respect to the plane of incidence. A fraction of the light amplitude is reflected at the air-nanowire layer interface. The rest transmits into the nanowire film. Linearly polarized light with arbitrary polarization can always be expressed as a combination of s- and p-polarization. Therefore, the incident light with a polarization at an angle of 45° with respect to the plane of incidence can be split into two terms: Light with the electric field component perpendicular to the nanowire elongation travels as a s-polarized wave in the layer, while light with the electric field component parallel to the nanowire elongation travels as a p-polarized wave. A fraction of these amplitudes reflect at the nanowire layer-substrate interface back into the nanowire layer and are partly transmitted into air. The amplitude that has traveled through the nanowire layer interferes with the amplitude that is immediately reflected at the first interface.

Following the model described by Figure 3.5, the transfer-matrix method depends on the reflection and transmission coefficients at the dielectric-nanowire layer interface, $r_{d,NW}$ and $t_{d,NW}$, the reflection coefficient at the nanowire layer - substrate interface, $r_{NW,Sub}$, and the transmission coefficient at the nanowire layer - dielectric interface, $t_{NW,d}$. Further, we need to determine the phase change of light traveling through the nanowire layer and the phase change of the light reflected at the first interface.

According to Figure 3.5, the reflected amplitude, $\mathbf{A_r}$, is given by

$$\begin{aligned} \mathbf{A_r} \quad = \quad & \mathbf{R}_{d,NW} \cdot \mathbf{J}_{in} + \mathbf{P}_d \cdot \mathbf{T}_{NW,d} \\ & \cdot \mathbf{P}_{NW} \cdot \mathbf{R}_{NW,Sub} \cdot \mathbf{P}_{NW} \cdot \mathbf{T}_{d,NW} \cdot \mathbf{J}_{in}, \end{aligned} \tag{3.20}$$

with $\mathbf{P}_d$ and $\mathbf{P}_{NW}$ the propagation matrices accounting for the phase changes of the light propagating through the dielectric and the nanowire layer, respectively, $\mathbf{J}_{in}$ the Jones vector defining the polarization of the incident light, and $\mathbf{R}_{d,NW}$, $\mathbf{R}_{NW,Sub}$, $\mathbf{T}_{NW,d}$, and $\mathbf{T}_{d,NW}$ diagonal reflection and transmission matrices including the Fresnel amplitude reflection

coefficients for s- and p-polarized light at the dielectric-nanowire and nanowire-substrate interfaces, and the Fresnel amplitude transmission coefficients at the nanowire-dielectric and dielectric-nanowire interfaces, respectively. The reflection and transmission coefficients for the dielectric-nanowire layer and nanowire layer-substrate interfaces were derived in Section 3.2.2. The first term of Equation 3.20 considers the Fresnel reflection at the air-nanowire interface. The second term includes the first reflection at the nanowire-substrate interface (see Fig. 3.5). Further oscillations in the nanowire layer are not taken into account in this calculation as multiple reflections in the nanowire layer are negligible due to the roughness of the air-nanowire and the nanowire-substrate interface. From Equation 3.20, we can see that we need to define the Jones vectors for the incident polarization, the reflection and transmission coefficients at the interfaces and the phase changes in the layer.

The Jones vectors $\mathbf{J}_{in}$ for s- and p-polarized light and for light polarized to +45° and -45° are given in Table 3.1.

Table 3.1: Jones vectors for s- and p-polarization and light polarized by +45° and -45°.

s-polarization	p-polarization	+45°	-45°
$\begin{pmatrix} 1 \\ 0 \end{pmatrix}$	$\begin{pmatrix} 0 \\ 1 \end{pmatrix}$	$\frac{1}{\sqrt{2}} \cdot \begin{pmatrix} 1 \\ 1 \end{pmatrix}$	$\frac{1}{\sqrt{2}} \cdot \begin{pmatrix} 1 \\ -1 \end{pmatrix}$

The phase changes of light traveling through the nanowire film with thickness L, $\phi_{NW,s,p}$, and through the dielectric, $\phi_{d,s,p}$ are given by

$$\phi_{NW,s,p} = \frac{2\pi}{\lambda} n_{s,p} \frac{L}{\cos\theta'_{s,p}}, \tag{3.21}$$

and

$$\phi_{d,s,p} = \frac{4\pi}{\lambda} n_d \sin\theta L \tan\theta'_{s,p}, \tag{3.22}$$

with $\theta'_{s,p}$ the angle between the wave vector and the sample normal inside the nanowire film. A detailed derivation of the phase change can be found in Ref. [81]. The propagation matrices $\mathbf{P}_d$ and $\mathbf{P}_{NW}$ for light propagating in the dielectric and in the nanowire film, respectively, are given by the phase change:

$$\mathbf{P}_d = \begin{pmatrix} \exp\left(-i\phi_{d,s}\right) & 0 \\ 0 & \exp\left(-i\phi_{d,p}\right) \end{pmatrix}, \mathbf{P}_{NW} = \begin{pmatrix} \exp\left(i\phi_{NW,s}\right) & 0 \\ 0 & \exp\left(i\phi_{NW,p}\right) \end{pmatrix}. \tag{3.23}$$

From the reflected amplitude $\mathbf{A}_r$, the reflected intensity, I_r, with a certain polarization can be determined by multiplying the matrix $\mathbf{A}_r$ with the Jones vector of the analyzer $\mathbf{J}_{out}$, and squaring this product

$$I_r = |\mathbf{J}_{out} \cdot \mathbf{A}_r|^2. \tag{3.24}$$

Using Equation (3.24), the intensity of light reflected by the nanowire layer can be determined for arbitrary polarizations.

A very sensitive measure of the birefringence of a medium is the reflection contrast, i.e., the ratio of light reflected from a birefringent layer transmitted through a polarizer and analyzer set crossed and parallel aligned. The sensitivity of the reflection contrast to the birefringence can be understood as follows. The total phase for s- and p-polarizations, $\phi_{s,p}$, accumulated after transmission through the birefringent layer can be expressed as

$$\phi_{s,p} = 2\phi_{NW,s,p} - \phi_{d,s,p} = \frac{4\pi}{\lambda}n_{s,p}L\cos\theta'_{s,p}, \tag{3.25}$$

where L denotes the thickness of the nanowire layer, λ the optical wavelength in vacuum, and $\theta'_{s,p}$ the angles between the normal to the surface of the sample and the wave vector in the medium. The factor 2 in the first term of the sum is due to the fact that the reflected light in the nanowire-substrate interface crosses the nanowire layer twice. The increase in the refractive index with θ for the p-polarization component and the increase of the phase for this polarization gives rise to a phase retardation and the rotation of the polarization vector. This retardation is measured as an increase of the intensity detected with crossed polarizers, $I_\perp$, and a concomitant decrease of intensity obtained with parallel polarizers, $I_\parallel$. The polarization contrast $I_\perp/I_\parallel$ in transmission or reflection represents the extinction of the original polarization state and is thus a measure for the quality of the birefringent material. For calculating the polarization contrast in reflection, the incident polarization is chosen to form an angle of 45° with the plane of incidence and the transfer-matrix method is applied twice: once with the analyzer set to 45°, i.e., the crossed state; and once with the analyzer set to -45°, i.e., the parallel state. The ratio of both signals defines then the reflection contrast.

3.3 Experimental Results

The birefringence of vertically aligned GaP nanowires was determined in Ref. [18] at a wavelength of 632 nm. In that work several ensembles of nanowires with different diameters and therefore different GaP filling fractions were investigated. Figure 3.6 shows the experimentally determined values of the birefringence parameter, i.e., the difference between extraordinary and ordinary refractive index, as a function of the filling fraction with open symbols. For comparison, the solid curve represents the birefringence parameter calculated using Eqs. (3.3) and (3.4). The small discrepancy between measurements and calculation can be attributed to the bending of the nanowires, which yields a lower Δn than that predicted by the theoretical model of perfectly aligned nanowires due to a reduction of the extraordinary refractive index and an increase of the ordinary refractive index [82]. The red symbol in Figure 3.6 represents the birefringence of calcite, which is a material with a high natural birefringence. Layers of GaP nanowires exceed the birefringence of calcite by more than a factor of 4.

While the birefringence of ensembles of GaP nanowires at a single wavelength was presented in Ref. [18], we have investigated the birefringence of these ensembles in a broad range of wavelengths from 550 nm to 1700 nm.
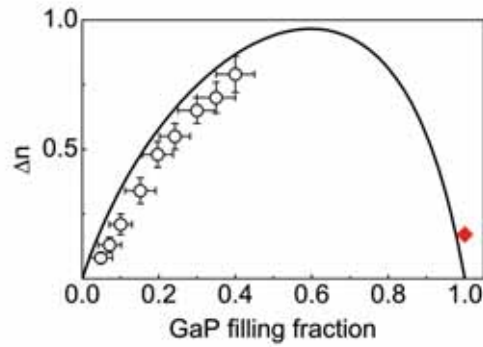
Figure 3.6: Birefringence parameter Δn as a function of the GaP filling fraction for ensembles of GaP nanowires with an average nanowire length of 1.5 μm, and different GaP filling fractions (reproduced from [18]). The birefringence of calcite is included for comparison (red diamond).

3.3.1 Reflection Contrast

The birefringence of vertically aligned GaP nanowires that are grown on a (111) GaP substrate can be determined by angular dependent polarization measurements of the reflection contrast. The angle resolved measurements are performed using a setup consisting of two computer controlled rotational stages that allow θ-2θ measurements. In this setup the sample can be rotated. This rotation varies the angle of incidence onto the sample θ. The detector is rotated around the the sample to an angle 2θ to measure the specular reflection from the sample. A schematic representation of the setup is given in Figure 3.7.
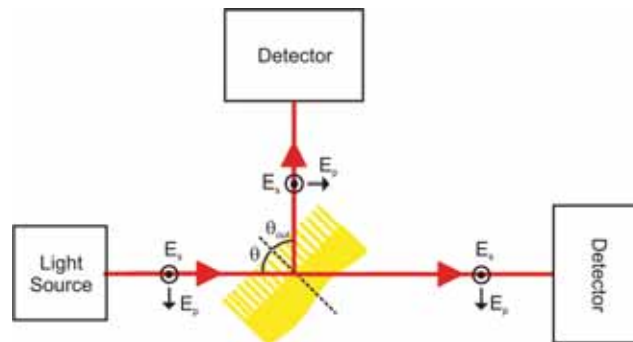

Figure 3.7: Schematic of the angle resolved setup. The sample and the detector are both mounted on computer controlled rotational stages to vary the angle of incidence as well as the detector angle independently and simultaneously.
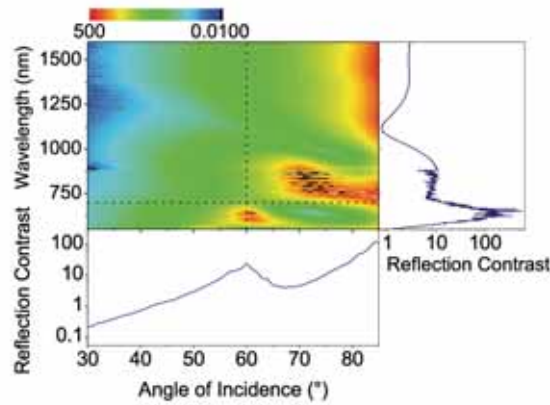
Figure 3.8: Measurement of the reflection contrast as a function of angle of incidence and wavelength and cuts of the contour plot at a wavelength of 700 nm and for an angle of incidence of 60° for GaP nanowires with a diameter of 40 nm and a length of 1.26 μm (Sample I in Table 2.1 on page 29).

The reflection contrast is determined experimentally using a halogen lamp as light source in combination with a fiber-coupled spectrometer with a silicon detector (Ocean Optics, USB2000) or an InGaAs photodetector array (Andor iDus). The polarizer in the incident light path is set at 45 ° with respect to the plane of incidence. The polarizer allows to have equal intensity of s- and p-polarized light. An analyzer is placed in the detector path and the reflection contrast is determined by dividing the intensity measured with crossed polarizer and analyzer, $I_\perp$, to the intensity measured with parallel polarizer and analyzer, $I_\parallel$.

A typical measurement of the reflection contrast as a function of angle of incidence and wavelength is given in Figure 3.8 for wavelengths longer than the electronic bandgap energy of GaP (λ_G = 549 nm). The reflection contrast is measured on Sample I (see Table 2.1 on page 29). The nanowires in the layer have a nanowire length of 1.26 ± 0.1 μm and diameter of 40 ± 25 nm, corresponding to a GaP filling fraction of 15 ± 4 %. The measurements show clear maxima and minima for certain angles and wavelengths. We show later, that these maxima and minima are related to both Fabry-Pérot oscillations in the nanowire layer and to the birefringence. While for wavelengths shorter than 1000 nm, the reflection contrast shows features for angles smaller than 80 °, for longer wavelengths the reflection contrast only increases with the angle.

To get a better understanding of the angular and spectral maxima and minima of the measured reflection contrast, we have performed a calculation of this contrast of a nanowire layer using the Jones calculus explained on pages 40-41. Figure 3.9 shows the calculated reflection contrast for a nanowire layer thickness of 1.26 μm. The refractive indices
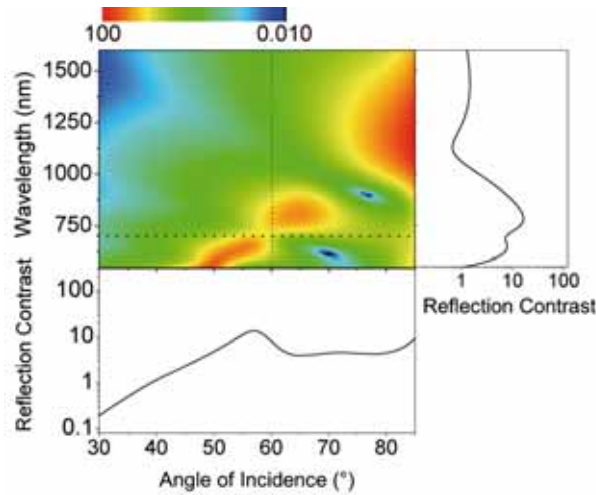
Figure 3.9: Calculation of the reflection contrast as a function of angle of incidence and wavelength and cuts of the contour plot at a wavelength of 700 nm and for an angle of incidence of 60°. The refractive indices used for this calculation are obtained from fits to measurements of s- and p-polarized reflectance of a layer of nanowires with a diameter of 40 ± 25 nm and a length of 1.26 μm.

used for this calculation are obtained from fits to the s- and p-polarized reflection.[1] Together with the contour plot of the reflection contrast as a function of angle of incidence and wavelength, cuts of the calculation are shown for a wavelength of 700 nm as a function of angle of incidence and for an angle of incidence of 60 ° as a function of wavelength.

To identify the origin of the maxima and minima in the reflection contrast, we have performed calculations where we neglect either the reflection at the air-nanowire interface, i.e., the first term in Equation 3.20 is set to 0, or where we assume a non-birefringent medium, i.e., the refractive index for s-polarized light equals the refractive index of p-polarized light. In the last case, the refractive index is set as the average of the ordinary and extraordinary refractive index and it does not depend on the angle of incidence.

The calculation neglecting the first reflection, and therefore neglecting the Fabry-Pérot oscillations in the nanowire layer is displayed in Figure 3.10. This calculation shows a maximum at a similar angle and wavelength as in the calculation of Figure 3.9 with a comparable amplitude. From the calculation neglecting Fabry-Pérot interference, we can conclude that the band of high reflection contrast in Figure 3.9 for angles of incidence between 45° and 90° and for wavelengths between 550 and 1250 nm is due to the birefringence of the layer. However, the origin of the two local minima within this band at angles of incidence of ∼ 59° and ∼ 70° is not yet explained, as well as the increase in contrast for wavelengths above 1000 nm to larger angles.

The modulation of the high reflection contrast band and the increase in contrast for

---

[1] More details of the determination of n_s and n_p can be found in Section 4.2.2 on page 53.
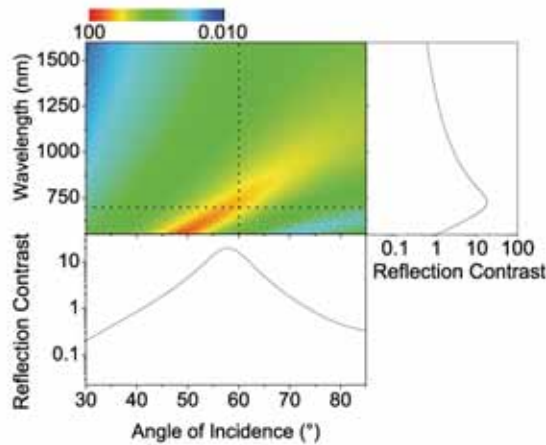
Figure 3.10: Calculation of the reflection contrast as a function of angle of incidence and wavelength and cuts of the contour plot at a wavelength of 700 nm and for an angle of incidence of 60°. In this calculation the reflection at the air-nanowire interface is neglected. The refractive indices used for this calculation are obtained from fits to measurements of s- and p-polarized reflectance of a layer of nanowires with a diameter of 40 ± 25 nm and a length of 1.26 μm.

wavelengths above 1000 nm can be explained by calculations of the reflection contrast for a non-birefringent medium. The refractive index used in this calculation is the average of the ordinary and extraordinary refractive index obtained from fits of the s- and p-polarized reflectance from sample I. These are shown in Figure 3.11. The contrast calculated for a non-birefringent medium is around one order of magnitude lower than that of the birefringent medium. As a function of wavelength, oscillations occur in the reflection contrast and this contrast increases for larger angles. The reflection contrast of the nanowire layer is given by the superposition of the birefringence and the Fabry-Pérot oscillations in the nanowire layer. While the effect of the birefringence is pronounced for angles varying between 40° and 70°, the Fabry-Pérot oscillations influence the reflection contrast at larger angles of incidence.

3.3.2 Broadband Birefringence

To determine the birefringence of a nanowire layer, the measured reflection contrast can be fitted as a function of angle of incidence for different wavelengths using the ordinary and extraordinary refractive indices as fitting parameters. While the maxima and minima in the reflection contrast can be fitted as a function of angle for a single wavelength with a unique set of n_o and n_e, the increase of the reflection contrast at higher angles for wavelengths longer than 1000 nm shown in Figure 3.8 cannot be unambiguously fitted with a single value of n_o and n_e. Therefore, a trustworthy birefringence parameter can
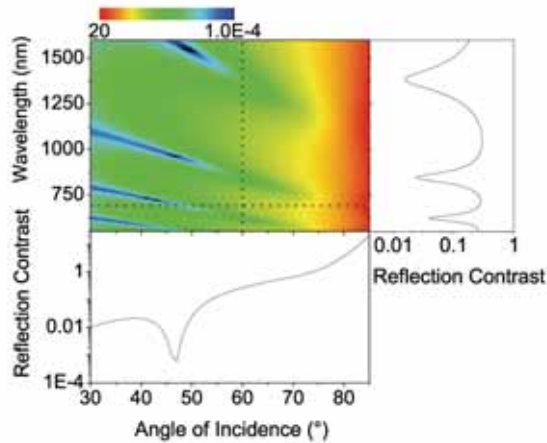
Figure 3.11: Calculation of the reflection contrast of an isotropic layer as a function of angle of incidence and wavelength and cuts of the contour plot at a wavelength of 700 nm and for an angle of incidence of 60°. The refractive index used in this calculation is the average of the ordinary and extraordinary refractive indices obtained from fits of s- and p-polarized reflectance of a layer of nanowires with a diameter of 40 ± 25 nm and a length of 1.26 μm.

be only obtained for wavelength shorter than 1000 nm. Fig. 3.12 shows a measurement (symbols) and fit (curves) of the reflection contrast of a nanowire layer with an average nanowire length of 1.3 μm and an average diameter of 21 nm, corresponding to a GaP filling fraction of 5 % (sample II, Table 2.1, page 29). The measurement and the fit are given as a function of angle of incidence and for three different wavelengths λ = 600 nm, 650 nm, and 700 nm. Each curve exhibits a maximum for a certain angle of incidence, which shifts to smaller angles at increasing wavelengths. From these fits, the wavelength dependent birefringence parameter can be determined. Figure 3.13a shows the wavelength dependent birefringence parameter Δn for sample II with a GaP filling fraction of 5 % (squares) together with a calculation (curve) of the birefringence using Maxwell-Garnett effective medium theory for a filling fraction of 5 %. In the wavelength range studied, the birefringence parameter is nearly constant, which is in agreement with Maxwell-Garnett effective medium theory. The small discrepancy between the experimental and theoretical values is related to the aforementioned bending on the wires, which results in an increase of the ordinary refractive index and a decrease of the extraordinary refractive index. Figure 3.13b shows the birefringence parameter Δn for sample II, III (circles), and IV (triangles) (see Table 2.1 on page 29). The diameters of the nanowires on these samples are 21 ± 3.5 nm, 26 ± 4.5 nm, and 31 ± 5.5 nm, respectively. With increasing nanowire diameter, and therewith increasing nanowire filling fraction, the birefringence parameter increases.
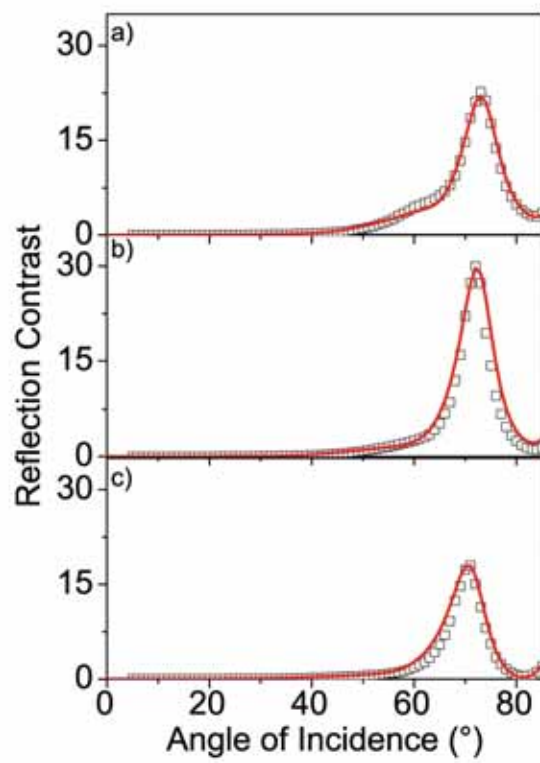
Figure 3.12: Measurement (symbols) and fits (curve) of the reflection contrast of a GaP nanowire sample with an average diameter of 21 nm corresponding to a GaP filling fraction of 5 % and an average nanowire length of 1.3 μm for a wavelength of a) 600 nm, b) 650 nm, and c) 700 nm.
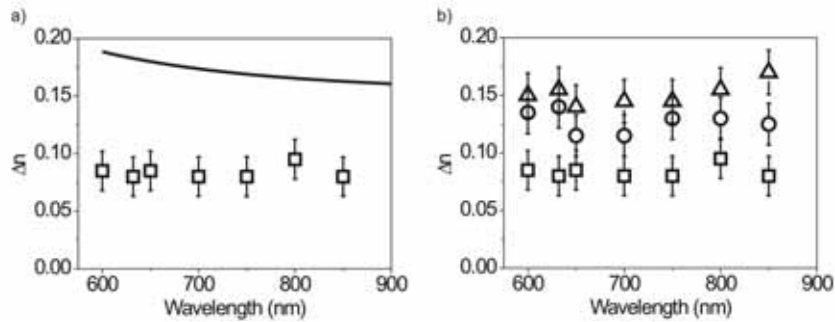
Figure 3.13: a) Birefringence parameter as a function of wavelength for a nanowire layer with an average diameter of 21 nm and a GaP filling fraction of 5 % (squares) and the birefringence determined from Maxwell-Garnett effective medium theory for a GaP filling fraction of 5 %. b) Birefringence parameter as a function of wavelength for different nanowire layers with an average diameter of 21 nm (squares), 26 nm (circles), and 31 nm (triangles).

3.4   Conclusions

In this chapter, we have described uniaxial media and we have shown that densely packed ensembles of vertically aligned GaP nanowires form uniaxial media exhibiting giant bire-fringence. The birefringence can be determined by measuring the reflection contrast. We have shown that the maxima and minima of the reflection contrast are related to a combination of the birefringence and Fabry-Pérot oscillations in the nanowire layer. The reflection contrast of ensembles of nanowires is modeled using Maxwell-Garnett effective medium theory and the transfer-matrix method based on Jones calculus. By fitting the ordinary and the extraordinary refractive indices, the birefringence was determined for a wavelength range from 600 nm to 850 nm. We have shown that the birefringence is constant in this range, which is in agreement with Maxwell-Garnett effective medium theory.

MODIFIED BIREFRINGENCE IN CORE-SHELL NANOWIRES

We demonstrate that the large birefringence of ensembles of vertically aligned GaP nanowires can be significantly modified by adding a shell as thin as 10 nm of SiO$_2$ around the nanowires. The modification of the birefringence is determined experimentally by polarization-dependent reflection measurements. This modification is modeled with Maxwell-Garnett effective medium theory and Jones calculus for anisotropic layers. S-polarized light is more sensitive than p-polarized light to changes in the surrounding of the nanowires. The reflection contrast exhibits large and narrow peaks that are strongly shifted due to the presence of the thin shell.

4.1 Introduction

Over the last decade, porous systems have attracted much attention in the fields of gas-, bio-, or chemical sensors [83–93]. Porous structures are very sensitive to changes in their surroundings due to a large surface to volume ratio. Recent works on porous silicon have shown that the reflection [83] and transmission [84], as well as the birefringence [85], are modified by infiltrating the pores with DNA [86], proteins [87], or gases [88]. In principle, all these sensors have one thing in common: They detect a change in the refractive index of the material filling the pores. We describe in this chapter the inverse system of a porous material, namely vertically aligned GaP nanowires. The dense ensembles of nanowires form an open structure in contrast to closed porous structures. Open structures can be easily infiltrated with the material to be sensed. The birefringence of the nanowire layers, that is described in Chapter 3, together with their large surface to volume ratio, leads to a high sensitivity of the reflection or transmission of light to the material surrounding the wires. We have chosen to work with SiO_2 as the material forming the nanowire shell because of its refractive index of 1.45 similar to that of bio-molecules in the visible and near-infrared [94]. Therefore, our results indicate that layers of semiconductor nanowires can be used as sensitive bio-sensors.

This chapter is organized as follows. First, we explain wavelength dependent reflection measurements for s- and p-polarization. We show that the SiO_2 shell modifies the reflection of the nanowire layer strongly, and that s-polarized light is more sensitive to the thin shell than p-polarized light. The larger sensitivity of s-polarization to changes in the surrounding of the nanowires is reproduced by calculations using the Maxwell-Garnett effective medium theory for coated cylinders [95]. In Section 4.3, the modification of the reflection contrast by SiO_2 shells with thicknesses between 10 nm and 30 nm is measured and calculated. We find that the reflection contrast peak shifts parabolically as a function of SiO_2-shell thickness.

4.2 Wavelength-dependent Modification of the Reflection

We demonstrate in this section that the birefringence of a layer of GaP nanowires is strongly modified by a SiO_2 shell as thin as 12 nm. The modification of the birefringence is measured for s- and p-polarized light as a function of the wavelength and we find that the reflection of s-polarized light is more sensitive to the SiO_2-shell. The deposition of the thin shell of SiO_2 by plasma-enhanced chemical vapor deposition (PECVD) is explained in Section 4.2.1. The thickness of the shell is determined by TEM. In Section 4.2.2 reflection measurements of layers of nanowires using s- and p-polarized incident light are presented. The measurements are analyzed using Maxwell-Garnett effective medium theory and Jones calculus. This analysis is described in Section 4.2.3.

4.2.1 Sample Fabrication

The nanowires are grown during 1020 s at a temperature of 420 °C. To increase the filling fraction of GaP in the nanowire layer, a shell is grown around the nanowires during 350 s

at a temperature of 630 °C (sample I, Table 2.1, page 29). A more detailed description of the nanowire growth process in given in Chapter 2.

We cleaved the sample into two pieces, and left one half as grown for reference measurements. On the other piece, SiO_2 was evaporated by plasma enhanced chemical vapor deposition (PECVD) in the dynamic deposition mode at a temperature of 300 °C and a pressure of 2.4 Torr for 10 s. We have chosen the dynamic deposition mode, as the deposition of SiO_2 occurs in this mode in five different chambers of the PECVD reactor, resulting in a homogeneous coating around the nanowires.
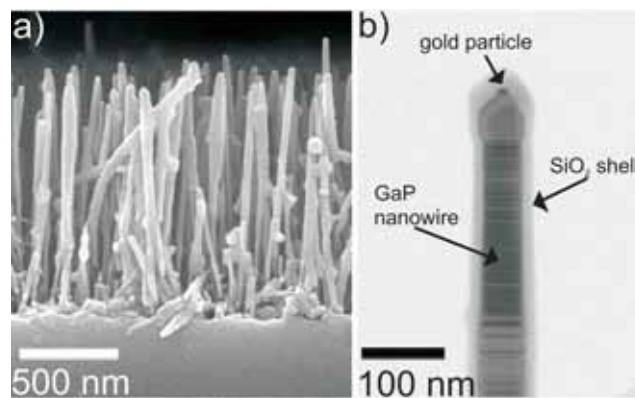

Figure 4.1: a) Side view scanning electron micrograph of as grown nanowires (Sample I, Table 2.1 on p. 29). b) Transmission electron micrograph of a nanowire coated with SiO_2.

Figure 4.1a shows a side view scanning electron micrograph (SEM) of the as grown nanowire sample. From this image, the length of the nanowires can be estimated to be 1.26 ± 0.1 μm and the diameter 40 ± 25 nm. In Figure 4.1b a transmission electron micrograph (TEM) of a nanowire covered with 12 nm of SiO_2 is shown. It is remarkable that the SiO_2 shell has a constant thickness over the nanowire length, which indicates a good infiltration of SiO_2 in the nanowire layer. The core of the nanowire shows twinning defects, with alternating orientations along the $< 111 >$ axis of the wire, and the gold particle used to catalyze the growth of the wires is visible on top of the nanowire. Both the twinning defects and the gold particle have no significant effect on the optical properties discussed next [18, 96].

4.2.2 Optical Experiments

We have measured spectra of the angle dependent specular reflectance of sample I (see Table 2.1, page 29) using the setup described in Chapter 3 on page 43. We used a halogen lamp as light source and a silicon spectrometer and an InGaAs spectrometer for detecting the visible and the near-infrared reflection, respectively.

Figure 4.2 shows the specular reflectance spectra for s- (black squares) and p-polarized light (red circles) measured at an angle of incidence of 60 °. From the Fabry-Pérot os-
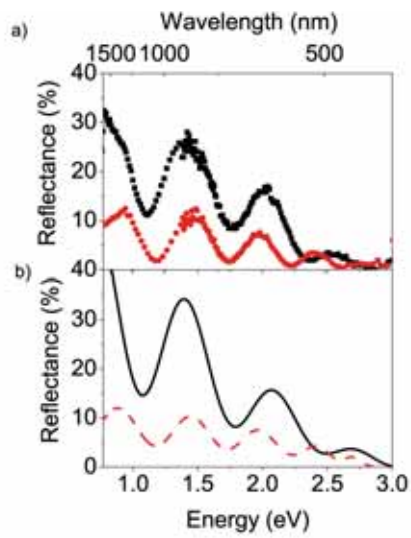
Figure 4.2: a) Measured specular reflectance spectra from a layer of GaP nanowires using s- (black squares) and p-polarized white light (red circles) for an angle of incidence of 60° and b) calculations of the specular reflection using Jones calculus for an angle of incidence of 60° for s- (black solid curve) and p-polarized (red dashed curve) light. The nanowire layer has a thickness of 1.26 ± 0.1 μm, and the nanowires have an average diameter of 40 ± 25 nm.

cillations visible in both measurements, we can conclude that the nanowire layer acts as an optical cavity due to the contrast of refractive indices at the air-nanowire and the nanowire-substrate interfaces. The reflection is reduced for photon energies above 1.77 eV (λ = 700 nm) due to scattering in the layer [96]. For energies above 2.25 eV (λ = 550 nm), the reflection is further reduced due to absorption in GaP. The noise in the measurements at wavelengths around 900 nm is related to the low quantum efficiency of the Si- and InGaAs-detectors in this wavelength range. Due to birefringence, the nanowire layer exhibits a larger optical thickness for p-polarized light than for s-polarized light, i.e., the effective refractive index for p-polarized light is larger than for s-polarized light. This difference in path length is apparent in the different period of the Fabry-Pérot oscillations of Figure 4.2. Figure 4.2b shows a calculation of the reflectance for s- (black solid curve) and p-polarization (red dashed curve) performed using Jones calculus [80]. For fitting the decrease in reflectance for higher photon energies, surface roughness and bulk scattering are included into the calculations. From these calculations, the ordinary, n_o, and extraordinary, n_e, refractive indices of the nanowire layer can be determined to vary from 1.10 to 1.12 and from 1.28 to 1.93, respectively, for photon energies ranging from 0.77 to 3.0 eV (1610 to 413 nm). The extinction coefficients are increasing for energies above 2.25 eV (550 nm) up to 0.0001 and 0.01 at 3 eV for n_o and n_e, respectively. The ordinary refractive index, n_o, corresponds to the refractive index for light polarized perpendicular to the nanowire long axis, while n_e describes the refractive index for light polarized parallel to this axis. A detailed discussion of the refractive indices, and the relation between the ordinary and the extraordinary refractive index and the refractive indices for s- and p-polarized light is given in Section 3.2 of Chapter 3. For an angle of incidence θ of 60°, n_s ranges from 1.10 to 1.12+0.0001i and n_p from 1.19 to 1.32+0.01i.

The Fabry-Pérot oscillations visible in Figure 4.2 can be modified by changing the optical thickness of the nanowire layer, e.g., by varying the physical thickness of the layer, or the nanowire diameter, or the nanowire density, or by filling the voids between the nanowires with a dielectric. Figures 4.3a and b display the measurements of specular reflection of s-polarized light from the uncoated nanowire sample and the sample with a thin shell of SiO_2, respectively, as a function of wavelength and angle of incidence. A shift of the Fabry-Pérot oscillations to larger wavelengths for the coated nanowires is visible. For clarity, Figures 4.3c and d show measurements performed at an angle of incidence of 60° for s- and p-polarization, respectively, for nanowire layers without (black solid curve) and with (red dashed curve) a layer of SiO_2. In both cases, a clear shift of the Fabry-Pérot oscillations to lower energies (longer wavelengths) is visible in the measurements of the sample with coated nanowires, due to the increased optical thickness of the nanowire layer. The shift of the Fabry-Pérot oscillations depends on the wavelength and is larger for s- than for p-polarization. For s-polarization and an angle of incidence of 60°, a shell of 12 nm of SiO_2 around the nanowires shifts the signal by 105 nm. This wavelength shift can be solely attributed to the larger optical thickness due to the shell of 12 nm of SiO_2 around the wires. The increase of the geometrical layer thickness because of the shell grown on top of the wires has a minor effect.

The difference between the specular reflectance measured on the nanowires with and without the SiO_2 coating is shown in Figure 4.4a for an angle of incidence of 60°, and

55
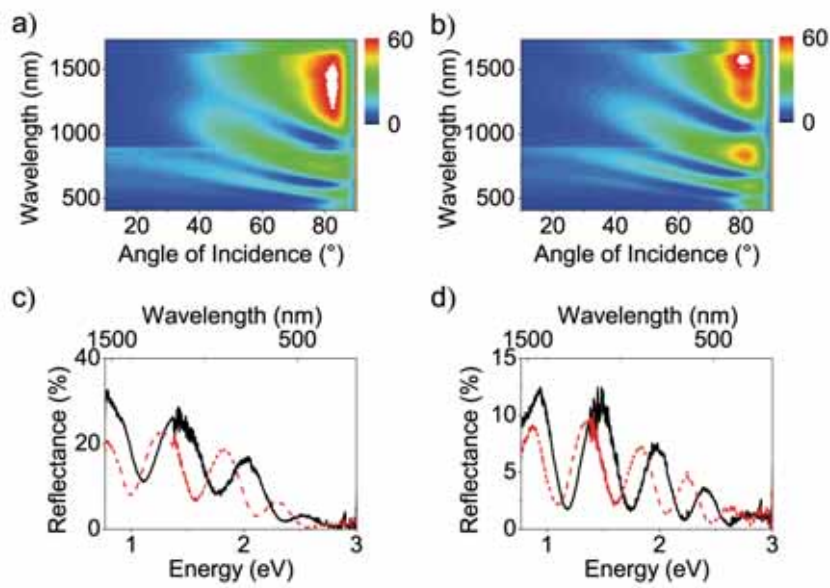
Figure 4.3: Measured specular reflectance spectra of sample I without a) and with b) a shell of 12 nm of SiO_2 around the nanowires using s-polarized white light as a function of the angle of incidence. Reflectance spectra measured at an angle of incidence of $60°$ for c) s- and d) p-polarized light without shell (black solid curve) and with shell (red dashed curve). The nanowire layer has a thickness of $1.26 \pm 0.1 \mu m$, and the nanowires have an average diameter of 40 ± 25 nm.

for s- (black squares) and p-polarized (red circles) light. This difference is larger for s-polarization indicating that this polarization is more sensitive to changes in the refractive index around the wires. Figure 4.4b displays calculations of the difference of the reflection spectra of a nanowire layer with and without SiO_2 shell. The calculations show a good agreement with the measurements confirming the enhanced sensitivity of s-polarization to changes in the surroundings of the nanowires.
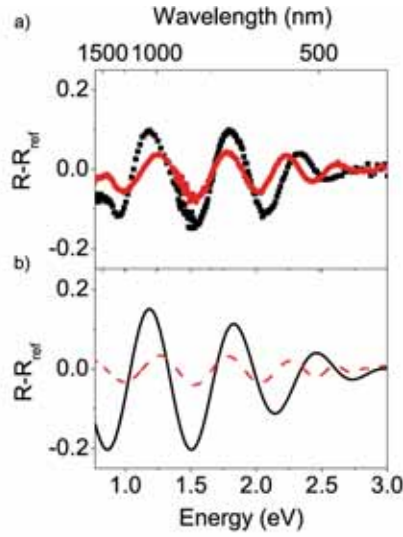

Figure 4.4: Difference between the specular reflectance spectrum of sample I coated with a shell of 12 nm of SiO_2 and the layer of nanowires without shell for a) s- (black squares) and p-polarized light (red circles) measured at $60°$ and b) calculations of this difference for s-polarization (black solid curve) and p-polarization (red dashed curve). The nanowire layer has a thickness of $1.26 \pm 0.1\mu m$, and the nanowires have an average diameter of 40 ± 25 nm.

4.2.3 Discussion

The larger wavelength shift of the reflection of s-polarized light compared to p-polarized light from layers of nanowires without and with a shell of SiO_2, can be described by calculating the effect of a shell surrounding the wires on the effective refractive indices of the layer. The refractive index of s-polarized light n_s, which equals the ordinary refractive index n_o, is calculated using the Maxwell-Garnett effective medium theory for core-shell cylinders, as described in Ref. [95]

$$n_s = n_o = \left[1 - \frac{2f_{cs}}{\gamma_1 + f_{cs}} \right]^{\frac{1}{2}},$$
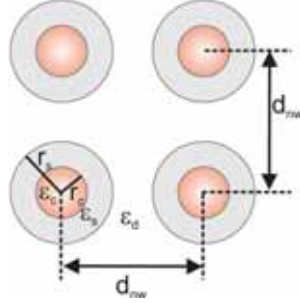
(4.1)

Figure 4.5: Schematic representation of a square array of core-shell nanowires. The radius of the core and of the core-shell nanowire are defined as r_c and r_s, respectively, and the distance between midpoints of two nanowires is d_{nw}. The permittivities of the core and shell material and the material surrounding the nanowire are ϵ_c, ϵ_s, and ϵ_d, respectively.

with

$$\gamma_1 = \frac{r_c^2(\epsilon_s - \epsilon_c)(\epsilon_d - \epsilon_s) + r_s^2(\epsilon_s + \epsilon_c)(\epsilon_d + \epsilon_s)}{r_c^2(\epsilon_s - \epsilon_c)(\epsilon_d + \epsilon_s) + r_s^2(\epsilon_s + \epsilon_c)(\epsilon_d - \epsilon_s)}. \tag{4.2}$$

The parameters used in these equations are illustrated in Figure 4.5: r_c is the radius and ϵ_c the permittivity of the core, r_s the radius of the core-shell nanowire and ϵ_s the permittivity of the shell, surrounded by a dielectric with the permittivity ϵ_d. The filling fraction of the coated nanowires is calculated using $f_{cs} = \pi r_s^2 / d_{nw}^2$ with d_{nw} the distance between the midpoints of two nanowires. The extraordinary refractive index is calculated as the geometrical average of the three media [25]

$$n_e = \sqrt{f_c\epsilon_c + f_s\epsilon_s + (1 - f_c - f_s)\epsilon_d}, \tag{4.3}$$

with $f_c = \pi r_c^2 / d_{nw}^2$ and $f_s = f_{cs} - f_c$.

From the ordinary, n_o, and the extraordinary, n_e, refractive indices, the refractive index for p-polarized light can be calculated with Equation (3.7) on page 36.

Figure 4.6a shows the refractive indices for s- (black solid curve) and p-polarized (red dashed curve) light as a function of the thickness of the shell. This calculation has been done considering d_{nw} = 120 nm, r_c = 20 nm, $\epsilon_s = n_{SiO_2}^2 = 2.1$, $\epsilon_c = n_{GaP}^2 = 10.9$, $\epsilon_d = 1$, and for an angle of incidence of 60°. These parameters describe the sample discussed in Section 4.2.2. Note that the values of n_s and n_p for the nanowire layer without shell (n_s = 1.07, n_p = 1.2 at 633 nm) obtained from this model deviate from the experimental values (n_s = 1.11, n_p = 1.21). The theoretical values are calculated assuming infinitely long and perfectly aligned cylinders. However, the nanowires used in our experiments are bent and finite in size (see Figure 4.1), which leads to a reduction of the birefringence [18, 97], i.e., the ordinary refractive index increases while the extraordinary refractive index decreases due to the misalignment of the nanowires. Figure 4.6b shows a calculation of the difference between the effective refractive index of a layer of nanowires with a SiO_2

shell and without a shell as a function of the SiO_2 thickness. From Figure 4.6b, we can conclude that the refractive index for s-polarized light is more sensitive to changes in the surrounding than the refractive index for p-polarization in layers of GaP nanowires with the parameters described above. For thicker shells, the difference in sensitivity of s- and p-polarized light increases. Furthermore, from Figure 4.6b we can estimate an increase of the effective refractive index for s-polarized light by 0.06 and for p-polarized light by 0.05 due to a 12 nm thick shell. As we have seen, these small changes have a strong impact on the specular reflection of light.
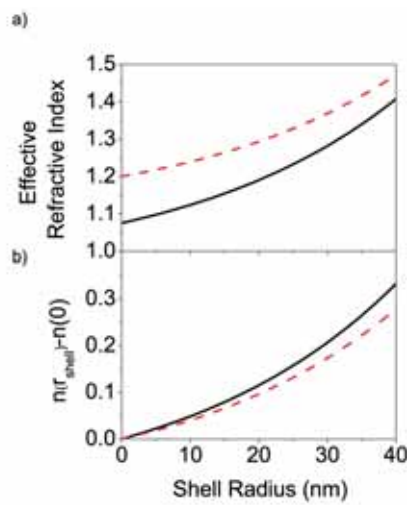

Figure 4.6: a) Effective refractive indices for s- (black solid curve) and p-polarization (red dashed curve) of a GaP nanowire layer with r_c = 20 nm and d_{nw} = 120 nm, as a function of the thickness of a shell around the nanowires with a refractive index of 1.45. The angle of incidence in this calculation is 60°. b) Difference between the refractive indices without and with a shell as a function of the shell thickness.

In conclusion, we have demonstrated that s- and p-polarized specularly reflected light from birefringent layers of semiconductor nanowires is significantly modified by a SiO_2 shell as thin as 12 nm. We have compared the modification of the reflection for s- and p-polarized light. Due to the large birefringence of the nanowire layer, s-polarized reflection is more affected by the thin shell.

4.3 Angular-dependent Modification of the Reflection Contrast

While in Section 4.2, we have analyzed the modification of the reflection on s- and p-polarized light of layers of nanowires due to a thin shell of SiO_2 around the nanowires, we focus here on the shift of the reflection contrast. The reflection contrast was defined in

Section 3.3.1 in Chapter 3 and describes the ratio of light reflected at an interface passing through a pair of crossed polarizer and analyzer to the light reflected passing through a pair of parallel aligned polarizer and analyzer. Due to the rotation of the polarization vector in birefringent materials and to Fabry-Pérot oscillations in the nanowire layer, large and narrow peaks appear in the reflection contrast. In this section, we investigate how sensitive these peaks are to changes in the refractive index of the surrounding of the nanowires.

This section is organized as follows. First, we explain the growth of the nanowires and the deposition of the SiO_2 shells. The measurement of the reflection contrast for different SiO_2 shell thicknesses varying between 10 and 30 nm is described in Section 4.3.2. The measurements are quantitatively described by calculations using Maxwell-Garnett effective medium theory and Jones calculus. We find that the reflection contrast peak shifts parabolically with increasing SiO_2 shell thickness.

4.3.1 Sample Fabrication

The experiment described in this section is performed on sample V (see Table 2.1 on page 29). The nanowires are grown during 1080 s using the VLS growth mechanism at a temperature of 420 °C and during 200 s in the lateral growth mode at 630 °C to increase the filling fraction of GaP in the layer. A detailed description of the growth process is given in Chapter 2. We determined by cross-sectional SEM images (Figure 4.7a) the thickness of the nanowire layer to be 1 ± 0.1 μm and the diameter of the nanowires to be 33 ± 9 nm. From top-view SEM images (Fig. 4.7b), we observe that the nanowires cluster together. The average distance between the nanowires is difficult to determine, but is in the range of 100 to 200 nm.
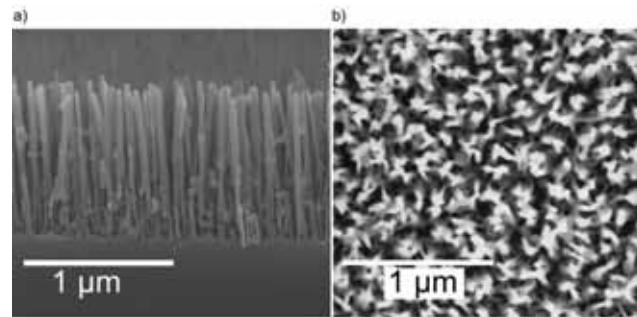
Figure 4.7: a) Side- and b) topview SEM image of sample V (see Table 2.1 on page 29).

We cleaved the sample into 5 pieces. On four pieces, SiO_2 with different layer thicknesses was evaporated by PECVD at a temperature of 300 °C and a pressure of 2.4 Torr during 4 s, 8 s, 15 s, and 20 s. The 5th sample was left unchanged as reference. Table 4.1 gives the evaporation times and evaporation modes and the resulting shell thicknesses around the nanowires. The first two samples were evaporated using a static mode, i.e.,

only one chamber of the PECVD system has been used. For the last two samples, a dynamic evaporation mode has been chosen to get a more homogeneous shell. In this mode 5 chambers are used.

Table 4.1: Evaporation times and modes of the SiO$_2$ shell and resulting shell thicknesses.

Sample	Evaporation time [s]	Evaporation mode	Shell Thickness [nm]
V	0	-	0
VA	4	static	10.3 ±1.3
VB	8	static	16.7 ±2
VC	15	dynamic	18.6 ±1.1
VD	20	dynamic	29.3 ±4.7

4.3.2 Optical Experiments

The angularly resolved reflection contrast is measured using the setup described in Chapter 3 in Section 3.3.1 with a diode laser emitting at a wavelength of 532 nm and a silicon photodetector. The incident polarization is set to 45° with respect to the plane of incidence. Two measurements are performed to determine the reflection contrast: One with the analyzer aligned almost parallel and the other with the analyzer aligned almost perpendicular to the incident polarization. To increase the amplitude of the reflection contrast, the analyzer is optimized to achieve a minimum intensity for parallel alignment and a maximum intensity for crossed alignment. Figure 4.8a shows the reflection contrast of Sample V measured using a beam size smaller than 1 mm on the sample. The measured reflection contrast has a maximum of 2450 at an angle of 53.99°, and a full-width at half maximum (FWHM) of 0.63°. For calculating the reflection contrast using the Jones calculus [80] and Maxwell-Garnett effective medium theory [95] using Equations. (4.1)-(4.3) (page 57), the core radius and the distance between the nanowires needs to be defined. A calculation of the reflection contrast is included in Figure 4.8a using a core radius, r_c = 19.65 nm, a distance between the nanowires, d_{nw} = 160 nm, a nanowire layer thickness of 1 μm, and the analyzer set to -56.4° for the calculation of $I_\parallel$ and 45° for the calculation of $I_\perp$.

The very sharp and narrow peak in the reflection contrast is not only very sensitive to changes in the surrounding of the nanowires, but also to inhomogeneities in the sample. To give an indication of the large sensitivity of this contrast, Figure 4.8b shows a calculation of the reflection contrast for three different radii of nanowires, namely 19.6 nm (black curve), 19.7 nm (red curve), and 19.8 nm (blue curve). A difference of 0.2 nm in the radius of the nanowires leads to an angular shift of 0.3°.

While this high sensitivity is very promising for future sensing devices, in which the reflection contrast on one sample is measured before and after infiltration with an analyte, the inhomogeneities in the samples will strongly influence the reflection contrast measured on different samples. These changes in reflection contrast due to inhomogeneities on the different samples will lead to large errors on the estimation of the shift of the peak
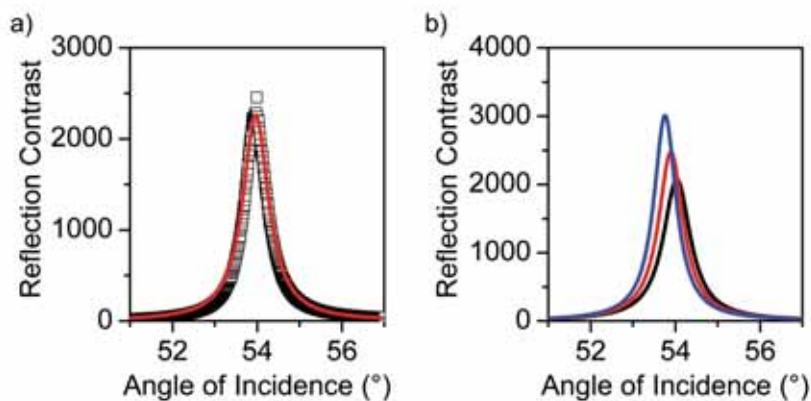
Figure 4.8: a) Measured (black squares) and calculated (red curve) reflection contrast of sample V (see Table 2.1 on page 29) as a function of the angle of incidence. For the calculations, we consider a radius of the nanowires r_c = 19.65 nm, an average distance between nanowires of d_{nw} = 160 nm, and a nanowire layer thickness of 1 μm. b) calculation of the reflection contrast for different nanowire radii: r_c = 19.6 nm (black curve), 19.7 nm (red curve), and 19.8 nm (blue curve).

in the reflection contrast due to the SiO_2 shell. To average out these inhomogeneities, the measurements are performed with a beam size $\sim$ 2 mm. This beam covers nearly the complete sample. The averaging leads to a reduced reflection contrast peak and a larger FWHM. Figure 4.9 shows the measurement performed on sample V and a calculation using the following parameters: r_c = 19.4 nm, d_{nw} = 160 nm, and the analyzer set to -53.4° for determining $I_\parallel$. The maximum reflection contrast for this sample is 162 and the FWHM is 1.8°.

Fig. 4.10a shows the measured reflection contrast of the five samples, while Fig. 4.10b shows a calculation for nanowires covered with the same SiO_2 thicknesses. The calculations are in excellent agreement with the measurements. Both measurements and calculations show that a SiO_2 shell with a thickness of $\sim$ 10 nm shifts the peak of the reflection contrast by $\sim$ 1°. Figure 4.11 displays the measured (black squares) and calculated (open circles) shifts of the peaks as a function of SiO_2 shell thickness. The fit of the peak shift (solid curve) shows a parabolical increase of the reflection contrast with SiO_2 shell thickness.

Considering that the refractive index of SiO_2 is close to that of biomolecules such as DNA and proteins, and that the size of these biomolecules can be in the order of a few nanometers to tens of nanometers, these measurements and calculations indicate that ensembles of nanowires might form a very sensitive platform for sensing. The high sensitivity of the reflection contrast to a medium surrounding the nanowires is further analyzed with respect to gas and bio-sensing in Chapter 9 and compared to a surface plasmon resonance sensor.
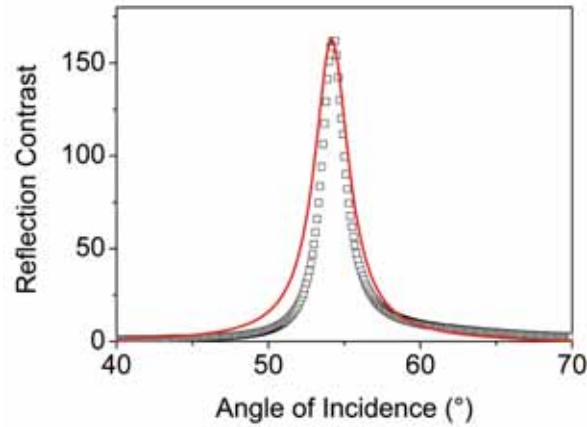
Figure 4.9: Measured reflection contrast of sample V using a large beam on the sample (black squares) and fit to the measurement (red curve) for a 1 μm thick nanowire layer with r_c = 19.4 nm and d_{nw} = 160 nm as fitting parameters.
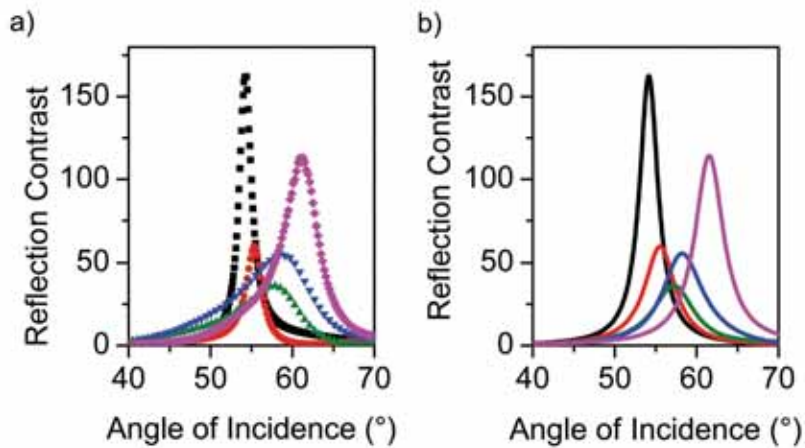
Figure 4.10: a) Measured reflection contrast of sample V (black squares), VA (red circles), VB (green up triangles), VC (blue down triangles) and VD (magenta diamonds) as a function of the angle of incidence and b) calculations of the reflection contrast for nanowires without shell (black curve) and shell thicknesses of 9 nm (red curve), 18 nm (green curve), 19.7 nm (blue curve), and 30 nm (magenta curve) for a 1 μm thick nanowire layer with r_c = 19.4 nm and d_{nw} = 160 nm.

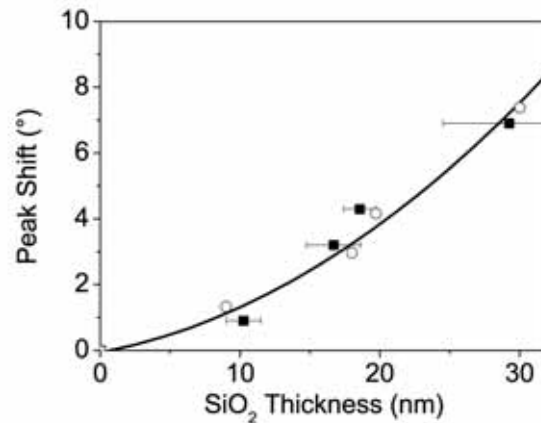**Figure 4.11:** Measured peak shift of the reflection contrast as a function of the SiO_2 thickness (black filled squares) and calculated peak shift of the reflection contrast for optimized polarization (black open circles).

4.4 Conclusions

We have demonstrated that the specular reflectance from birefringent layers of semiconductor nanowires can be significantly modified by a SiO_2 shell as thin as 10 nm. We have compared the modification of the reflection for s- and p-polarized light as a function of wavelength. Due to the large birefringence of the nanowire layer, s-polarized reflection is more affected by the thin shell. This result is explained with Maxwell-Garnett effective medium theory for coated cylinders. Further, we have demonstrated that the reflection contrast measured on layers of nanowires is very sensitive to changes in the surrounding of the nanowires. A change in radius of the nanowires as small as 0.2 nm results in a shift of the reflection contrast of 0.3°. The reflection contrast peak is shifted by shells of SiO_2 with different thicknesses. A shell with a thickness of ~ 10 nm shifts the reflection contrast by ~ 1°. The large and narrow peaks in the reflection contrast and their shift with the SiO_2 shell are measured and modeled using the Jones calculus and Maxwell-Garnett effective medium theory.

IN-PLANE BIREFRINGENCE OF ENSEMBLES OF GaP NANOWIRES

GaP nanowires grown on a (100) substrate are aligned forming an angle of 35° with respect to the substrate. Due to this alignment, dense ensembles of GaP nanowires form biaxial media. We determine the in-plane birefringence of layers of nanowires with different nanowire diameter by measuring the transmission contrast.

5.1   Introduction

The morphology of nanowires does not only depend on the growth parameters, such as temperature or gas pressure in the metal-organic vapor phase epitaxy reactor, but is strongly related to the crystallographic structure of the substrate on which they are grown [98]. While the nanowires described in Chapters 3 and 4 are grown on (111) GaP substrates, resulting in vertically aligned nanowires with a large birefringence, we focus here on nanowires grown on (100) substrates. As the preferential growth direction of nanowires is the <111>B direction [60], the growth of nanowires on (100) substrates results in nanowires with a preferential direction forming an angle of 35° with respect to the substrate. The geometrical anisotropy of nanowires together with the preferential growth directions of dense ensembles of nanowires results in a biaxial medium, with three distinct permittivities. In this chapter, we explain biaxial media and determine the in-plane birefringence, i.e., the difference in refractive indices for light polarized along and perpendicular to the nanowire axis, of layers of nanowires with different nanowire diameter grown on (100) substrates. While the in-plane birefringence of porous media has been studied extensively [65, 69, 72], the optical properties of nanowires grown on (100) substrates are described here for the first time.

The chapter is organized as follows: The fabrication of the nanowire layers is explained in Section 5.2. The in-plane birefringence of layers of nanowires grown on (100) substrates is explained in Section 5.3. In Section 5.4 the in-plane birefringence of layers of nanowires grown on (100) substrates is experimentally determined for samples of nanowires with different diameters.

5.2   Fabrication

The GaP nanowires were grown on (100) GaP substrates during 1020 s with the VLS growth mechanism. A detailed description of the growth of GaP nanowires on (100) substrates is given in Chapter 2 in Figure 2.6 on page 26. To vary the filling fraction of GaP in the nanowire layer, the diameter of the nanowires has been increased by switching to the lateral growth mode. The growth parameters of these samples are given in Table 2.1 on page 29 (see samples VI-IX). A cross-sectional scanning electron micrograph of sample VII is given in Figure 5.1. The majority of the nanowires are grown at an angle of 35° with respect to the substrate, corresponding to the <111> direction. The top-view SEM images displayed in Figures 5.1b and c show that the nanowires grow preferentially along the horizontal direction in the SEM image, indicating that the nanowires only grow into the expected <111>B direction. The Fourier transform of Figure 5.1c, shown in Figure 5.1d, confirms that the majority of the nanowires are grown along the horizontal direction. This anisotropic growth is apparent from the vertical line in the Fourier image. However, some nanowires are oriented in the vertical direction of the SEM image, resulting in the horizontal broadening of the Fourier image.
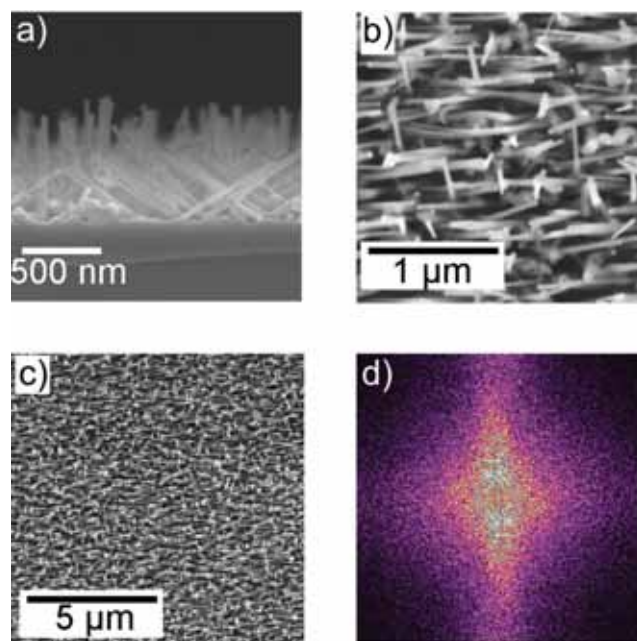
Figure 5.1: Scanning electron micrographs of ensembles of GaP nanowires grown on a GaP (100) substrate. a) Cross-section, b) top-view c) top-view with lower magnification than b), and d) Fourier transform of c). The Fourier image shows a vertical line indicating that the nanowires grow preferentially along one direction, the broadening of the line is due to a minority of nanowires that grow in a direction perpendicular to the major nanowire growth direction.

5.3   Theoretical Background

If the preferential growth direction of the nanowires is not perpendicular to the substrate, and if the nanowires grow along a distinct direction, as in the case of nanowires grown on a (100) substrate, the layer of nanowires form a biaxial material with a permittivity tensor given by

$$\epsilon = \left(\begin{array}{ccc} \epsilon_{\text{slow}} & 0 & 0 \\ 0 & \epsilon_{\text{fast}} & 0 \\ 0 & 0 & \epsilon_{\text{z}} \end{array} \right). \tag{5.1}$$

The effective permittivities of the biaxial medium are defined as follows: a slow permittivity, ϵ_{slow}, is defined for light polarized along the nanowire elongation and a fast permittivity, ϵ_{fast}, for light polarized perpendicular to this direction (see Fig. 5.2). The third permittivity, ϵ_{z}, for light polarized along the nanowire layer, is not probed in this study. The refractive indices along the 3 principal axes are given by the square root of the permittivities. The in-plane birefringence of ensembles of nanowires grown on a (100) substrate can be determined by measuring the transmission through the nanowire layer. Therefore, incident light is polarized linearly and the transmitted intensity is measured with an analyzer with a polarization state that is either perpendicular, $I_\perp$, or parallel, $I_\parallel$, to the incident polarization. The ratio of the two signals, $I_\perp / I_\parallel$, defines the transmission contrast. A schematic representation of the experimental setup is shown in Figure 5.2.
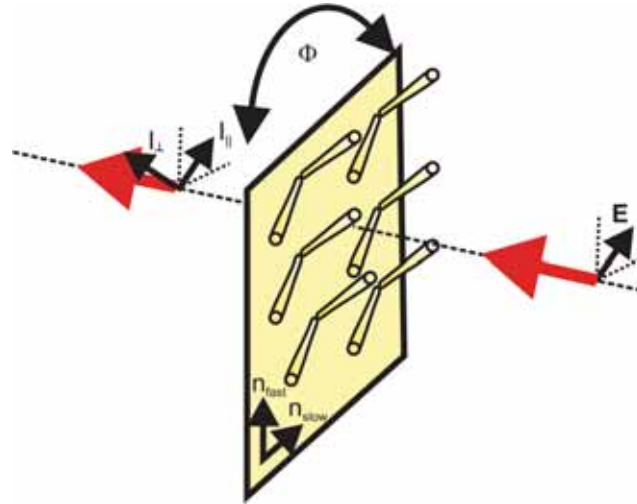
Figure 5.2: Experimental setup to determine the birefringence of nanowires grown on a (100) substrate. Linearly polarized light is incident onto the sample and the transmission is measured using a perpendicular and parallel analyzer to the incident polarization. The ratio of transmissions is measured as a function of the azimuthal angle Φ.

According to Figure 5.3 the in-plane birefringence can be determined from the transmission contrast. The two in-plane polarization axes in the biaxial medium, i.e., the slow

and the fast axes, which are orthogonal to each other, are plotted together with the transmission axes of the polarizer and analyzer [63]. The polarization state passing through the polarizer is given by the vector **OP**, while the polarization state passing through the analyzer is given by the vector **OA**. The incident polarization forms the angle Φ with the slow axis, while χ is the angle between the incident polarization and the transmission axis of the analyzer. Using this definition, we deduce the intensity of linearly polarized light traveling through a birefringent medium with an analyzer aligned parallel or perpendicular to the incident polarization. The amplitude of the incident field is given by the vector **OE**[1], which is parallel to **OP**. To relate the incident electric field **E** to the two axes of the biaxial medium, we determine the components along the slow and fast axes:

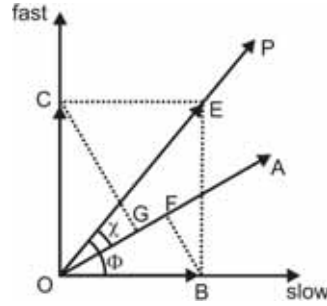$$OB = |\mathbf{E}| \cos\Phi, \; OC = |\mathbf{E}| \sin\Phi. \tag{5.2}$$

Figure 5.3: Construction of the polarization components transmitted by a polarizer and analyzer [63].

Only the components parallel to OA are transmitted through the analyzer, with amplitudes

$$OF = |\mathbf{E}| \cos\Phi \cos(\Phi - \chi), \; OG = |\mathbf{E}| \sin\Phi \sin(\Phi - \chi). \tag{5.3}$$

After traveling through the birefringent medium, a phase difference $\delta = \frac{2\pi}{\lambda} \Delta n L$ is built up between the two components, OB and OC, with λ and L the vacuum wavelength and the thickness of the nanowire layer, respectively, and the birefringence parameter $\Delta n = n_{\text{slow}} - n_{\text{fast}}$. The intensity of two monochromatic waves with phase difference δ interfering with each other is given by

$$I = I_1 + I_2 + 2\sqrt{I_1 I_2} \cos\delta \tag{5.4}$$

with I_1 and I_2 the intensities or squared amplitudes of the two beams. The interference of the two beams with the amplitudes OF and OG is given by Equations (5.3) and (5.4), resulting in

$$I = |\mathbf{E}|^2 \left(\cos^2\chi - \sin(2\Phi) \sin(\Phi - \chi) \sin^2\frac{\delta}{2} \right). \tag{5.5}$$

The second term in Equation (5.5) is introduced by the birefringence. For a non-birefringent medium, i.e., $\delta = 0$, the intensity would be $I = |\mathbf{E}|^2 \cos^2\chi$.

---

[1]For simplicity and consistency with the notation, we will refer to the field amplitude **OE** as **E**

To obtain the in-plane birefringence parameter Δn from measurements of the transmission contrast, we determine the maximum contrast $\frac{I_\perp}{I_\parallel}$. To obtain the maximum contrast, the intensity of light passing through parallel aligned polarizer and analyzer, $I_\parallel$, must be minimum, while the intensity for crossed polarizer and analyzer, $I_\perp$, must be maximum. If the polarizer and analyzer are parallel to each other, i.e., $\chi = 0$, Equation 5.5 reduces to

$$I_\parallel = |\mathbf{E}|^2 \left(1 - \sin^2(2\Phi)\sin^2\frac{\delta}{2}\right). \tag{5.6}$$

Maximum transmission is achieved when $\Phi = 0, \frac{\pi}{2}, \pi, ...$, thus when the transmission axis of the analyzer coincides with one of the axes of the birefringent medium, i.e., if the light is polarized along or perpendicular to the nanowire elongation. A minimum in transmission for parallel polarizer and analyzer is obtained if $\Phi = \frac{\pi}{4}, \frac{3\pi}{4}, \frac{5\pi}{4}, ...$ resulting in

$$I_{\parallel\mathrm{min}} = |\mathbf{E}|^2 \left(1 - \sin^2\frac{\delta}{2}\right) = E^2 \cos^2\frac{\delta}{2}. \tag{5.7}$$

If the polarizer and analyzer are perpendicular to each other, i.e., $\chi = \pi/2$, the intensity is given by

$$I_\perp = |\mathbf{E}|^2 \sin^2(2\Phi)\sin^2\frac{\delta}{2}. \tag{5.8}$$

In this case, the minima and maxima occur for the same angles of Φ, that resulted in maxima or minima for parallel polarizer and analyzer. The maximum intensity is

$$I_{\perp\mathrm{max}} = |\mathbf{E}|^2 \sin^2\frac{\delta}{2}. \tag{5.9}$$

From Equations (5.7) and (5.9), the maximum of the transmission contrast is determined to be

$$\frac{I_{\perp\mathrm{max}}}{I_{\parallel\mathrm{min}}} = \tan\left(\frac{\pi\Delta n L}{\lambda}\right). \tag{5.10}$$

The birefringence parameter Δn can be determined by measuring the transmission contrast from Equation (5.10).

5.4 Experimental Results

The in-plane birefringence of nanowires grown on a (100) substrate is determined by measuring the transmission of linearly polarized light from a diode laser with a wavelength of 690 nm through the nanowire layer. The transmission is measured for parallel, $I_\parallel$, and crossed, $I_\perp$, polarizer and analyzer and the sample is rotated azimuthally around the normal of the sample surface (see Fig. 5.2). The transmission contrast $I_\perp/I_\parallel$ is displayed for sample VI (squares), VII (circles), VIII (triangles), and IX (diamonds) (see Table 5.1) in Figure 5.4 as a function of the azimuthal angle. For azimuthal angles from 0° to 180° a two-fold symmetry in $I_\perp/I_\parallel$ is visible indicating an in-plane birefringence of all samples. At 45° and -45° the nanowires are aligned perpendicular or parallel to the incident polarization, and the light travels with a phase velocity according to n_{slow} or n_{fast}. In this

Table 5.1: List of the samples including average diameter, length of the wires, GaP filling fraction and birefringence parameter Δn.

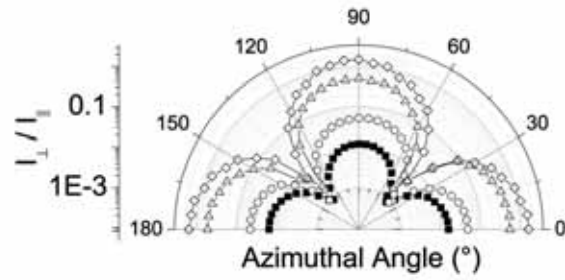| Sample	Average diameter [nm]	Nanowire layer thickness [μm]	GaP filling fraction [%]	Birefringence parameter Δn
VI	22 ± 4	1.2 ± 0.1	7 ± 4	$(3 \pm 0.3) \cdot 10^{-3}$
VII	31 ± 3	1.3 ± 0.1	15 ± 5	$(1.1 \pm 0.1) \cdot 10^{-2}$
VIII	43 ± 10	1.4 ± 0.2	25 ± 5	$(9.9 \pm 1) \cdot 10^{-2}$
IX	72 ± 19	1.5 ± 0.2	35 ± 5	$(2 \pm 0.2) \cdot 10^{-1}$

Figure 5.4: Transmission contrast $I_\perp / I_\parallel$ as a function of the azimuthal orientation of the nanowires measured at a wavelength of 690 nm, for the sample with a nanowire filling fraction of 7 % (black squares), 15 % (open circles), 25 % (open triangles), and 35 % (open diamonds).

case, no retardation takes place, resulting in a low transmission contrast. At $0°$, $90°$, and $180°$, the nanowires are aligned at $45°$ with respect to the polarization direction. In this case, the light has a component parallel to the slow axis and a component parallel to the fast axis. These two components travel with a different phase velocity resulting to retardation and leading to a maximum contrast. For the thinner wires, the retardation is small, corresponding to a low maximum value of the contrast. With increasing nanowire diameter and GaP filling fraction, the maximum value of the contrast increases. For the sample with the highest GaP filling fraction, the transmission contrast becomes larger than unity, indicating that linearly polarized incident light is converted into circularly polarized light, i.e., the light intensity contributions passing through crossed and parallel aligned polarizer and analyzer are equal. From the measured transmission contrast, the in-plane birefringence parameter of the nanowire samples can be determined using Equation 5.10. The birefringence parameters are displayed in Table 5.1, together with the average nanowire diameter, layer thickness, and the GaP filling fraction of the layer. For the highest filling fraction sample, with a maximum contrast of 1.5, a retardation $\Delta = \Delta n L$ of $\lambda/4$ is calculated. This layer behaves as a quarter-wavelength plate for a wavelength of 690 nm. The in-plane birefringence of this layer is comparable to that measured in porous media [69, 72].

5.5   Conclusions

We have shown that GaP nanowires grown on a (100) substrate form a biaxial medium due to the preferential growth direction. The in-plane birefringence of layers of nanowires with different filling fractions was determined experimentally. Layers of GaP nanowires can form a $\lambda/4$-waveplate at a wavelength of 690 nm.

SCATTERING OF LIGHT IN ENSEMBLES OF GaP NANOWIRES

The scattering of light by nanowires depends strongly on their diameter. In this chapter, we determine the scattering mean free path of light in layers of vertically aligned nanowires. We show that the scattering is anisotropic and that the scattering mean free path varies with the angle of incidence due to the alignment of the nanowires. GaP nanowires grown on (100) substrates form a stronger scattering medium than vertically aligned nanowires.

6.1   Introduction

Looking by eye at ensembles of nanowires with different diameters already reveals interesting phenomena: Figure 6.1 shows a photograph of a bare GaP substrate and of GaP substrates covered with ensembles of nanowires with the same density and length, but with different diameters. While the GaP substrate, as well as the layers of nanowires with small nanowire diameter are transparent for wavelengths longer than the electronic bandgap wavelength of GaP (λ_{gap} = 549 nm), the layers with thicker nanowires are opaque. The opacity of these layers results from the multiple scattering of light.
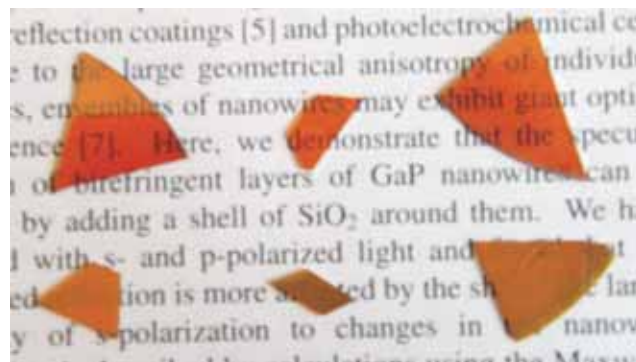

Figure 6.1: Photograph of different GaP nanowire samples. From left to right and top to bottom: GaP substrate, and samples X, XI, XII, XIV, and XV (see Table 2.1 on page 29), with an average nanowire diameter of 12 nm, 30 nm, 60 nm, 90 nm, and 110 nm, respectively. With increasing nanowire diameter, the samples become opaque.

Light propagates in a homogeneous medium, such as a GaP substrate, in straight trajectories. If inhomogeneities are added to this medium, such as nanowires grown on top of the substrate, the propagation of light gets disturbed, and the direction of propagation changes. As more inhomogeneities are added to the medium, or as the inhomogeneities scatter light more strongly, the medium becomes opaque. A schematic of light propagating in a multiple scattering medium is given in Figure 6.2. The average distance between two scattering events is called scattering mean free path l_{s} and describes the scattering strength of the medium.

Scattering of light is an everyday phenomenon. For example, the color of a blue sky on a sunny day is due to wavelength dependent scattering of light by molecules in the atmosphere. A gastronomic example of the transition between a transparent and a opaque medium is the white of an egg: If this part of the egg is untouched, it is transparent, while after whipping, air bubbles are introduced that scatter visible light resulting in a white and opaque medium.

Scattering of light can be classified into three different types: Rayleigh scattering, Mie scattering, and geometrical-optics scattering. Rayleigh scattering represents the limit of scatterers with dimensions much smaller than the wavelength of light. The blue sky described above is due to Rayleigh scattering by molecules in the atmosphere. The scattering
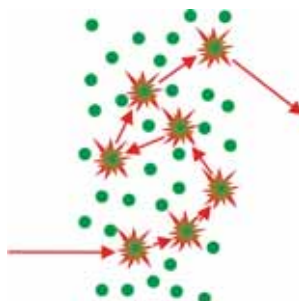
Figure 6.2: Light in a medium consisting of scatterers (green circles) does not travel along a straight trajectory. Multiple scattering samples are characterized by the average distance between two scattering events, i.e., the scattering mean free path l_s. The red arrows represent the **k**-vector of light. For simplicity, we represent a scattering event as a change in the direction of the **k**-vector. In reality, the scatterers are local sources of scattered radiation emitting in many direction.

cross section of a scatterer is a hypothetical area which describes the likelihood of light being scattered. In the Rayleigh scattering limit, this cross section depends on the wavelength by $\sigma_s \propto \lambda^{-4}$. In the geometrical optics regime, the scatterers are much bigger than the wavelength of light. In this regime the well-known equations for reflection and refraction (Fresnel's laws and Snell's law) can be applied. In the intermediate regime, called Mie scattering regime, the size of the scatterers is of the same order than the wavelength. In this regime, the scattering cross section exhibits multiple resonances that depend on the size and geometry of the scatterers.

Strongly scattering media are studied intensely with respect to Anderson localization [99], i.e., an inhibition of the transport of light due to interference of the multiply scattered waves. In the case of isotropic scatterers, the Anderson transition between extended and localized states takes place when $kl_s \sim 1$ (Ioffe-Regel criterion), where $k = 2\pi n_{eff}/\lambda$, with n_{eff} the effective refractive index of the medium, λ the vacuum wavelength, and l_s the scattering mean free path. The strongest scattering media to date are GaAs powder with $kl_s \leq 1$ [99], porous GaP with $kl_s \sim 2$ [100], and TiO_2 powder with $kl_s = 2.5$ [101]. The very low value of kl_s in GaAs powder has been questioned by the possible presence of absorption [102]. As a result of the research presented here, we have to add to this list GaP nanowires with $kl_s \sim 2.4$.

Scattering of light in layers of nanowires is not only interesting from a fundamental point of view. Intensive research is currently done with ensembles of nanowires for increasing the photovoltaic efficiency of solar cells [23, 103] and the emission efficiency of LEDs [104]. This research has focused so far on the material properties, while multiple scattering plays a prominent role in absorption and extraction of light by ensembles of nanowires. Therefore, for optimizing these applications, a thorough understanding of light propagating in layers of nanowires has to be obtained.

We determine in this chapter the scattering mean free path of ensembles of vertically aligned GaP nanowires depending on polarization and angle of incidence. For layers of

nanowires grown on (100) substrates, we find that the scattering mean free path depends on the nanowire orientation. This is a consequence of the geometrical anisotropy of these nanostructures. We model the scattering mean free path using Mie scattering theory for infinitely long cylinders. The smallest value of kl_s that we have measured is 2.4.

This chapter is organized as follows. A short introduction to Mie theory of infinitely long cylinders and multiple scattering is given in Section 6.2. Section 6.3 describes the measurements of the scattering mean free path in ensembles of vertically aligned nanowires. The scattering mean free path of nanowires grown on (100) GaP substrates is discussed in Section 6.4.

6.2   Mie Theory of Scattering of Light

As we have shown in Chapters 3-5, the interaction of light with nanowires is strongly anisotropic, resulting in a large birefringence of ensembles of nanowires. The birefringence described in those chapters refers to the propagation of the coherent beam or the beam scattered in the forward direction. Therefore, we made use of an effective medium model to describe the ensemble of nanowires. However, the presence of discrete scatterers removes intensity from the coherent beam. If the scattering is strong enough, the medium becomes opaque and multiple scattering dominates the transport of light.

In this section, we describe first anisotropic scattering by single nanowires, before we extend this description to anisotropic scattering of light in ensembles of nanowires. A typical measure of the scattering strength of light by a scatterer is the scattering efficiency, Q_{sc}, i.e., the ratio of the scattering cross section and the geometrical cross section. The scattering mean free path is, in a first approximation, inversely proportional to the density of scatterers and their scattering cross section.

To determine the scattering efficiency of an infinitely long nanowire, we define the incident electric field according to Figure 6.3, with a nanowire with diameter d and refractive index n_c embedded in a medium with refractive index n_d. The scattering efficiency is given by the ratio of the total power, $W_{sc,s,p}$, that is scattered by the nanowire for s- and p-polarized incident light within a closed imaginary concentric surface with radius r and unit length l around the cylinder, and the incident irradiance I_i,

$$Q_{sc,s,p} = \frac{W_{sc,s,p}}{dlI_i}, \tag{6.1}$$

where $W_{sc,s,p}$ is given by

$$W_{sc,s,p} = rl \int_o^{2\pi} (S_{sc,s,p})_r d\phi \tag{6.2}$$

with $(S_{sc,s,p})_r$ being the radial component of the Poynting vector $S_{sc,s,p} = \frac{1}{2}\Re(\mathbf{E}_{sc,s,p} \times \mathbf{H}^*_{sc,s,p})$. The incident and scattered electric and magnetic fields are expanded in cylindrical harmonics and the electromagnetic boundary conditions are applied to determine the fields inside and outside the cylinder. These fields will depend on the angle of incidence, wavelength and on the polarization of the fields. A detailed derivation of the scattered
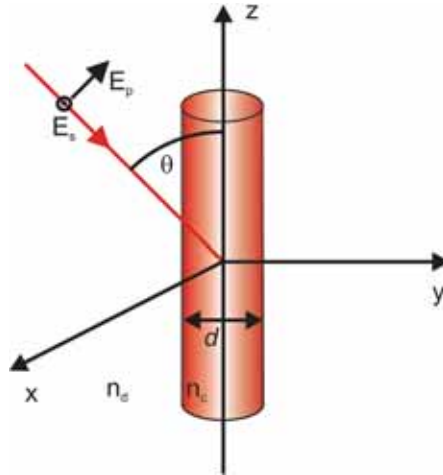
Figure 6.3: Schematic of light impinging from a medium with refractive index n_d with an angle θ onto an infinitely long cylinder with diameter d and refractive index n_c.

fields by infinitely long cylinders is given in Ref. [24] on pages 194-208. This derivation is tedious, but it provides analytical expressions in the form of infinite series for the scattering efficiencies of cylinders with arbitrary diameter. The lack of translational symmetry along the cylinder axis for finite length cylinders complicates tremendously these calculations and it is only possible to obtain numerical solutions of the scattered fields.

The scattering anisotropy of thin nanowires becomes apparent when considering the scattering efficiency of a single nanowire embedded in air as depicted in Figure 6.4 for an angle of incidence $\theta = 90°$. These calculations have been done for a refractive index of the nanowires of $n_c = 3.26$, which corresponds to the refractive index of GaP at $\lambda = 690$ nm. The scattering efficiency in Figure 6.4 is plotted as a function of the dimensionless size parameter $kr = \frac{\pi}{\lambda} d n_d$, where r is the radius of the nanowire, d is the diameter of the nanowire and n_d the refractive index of the dielectric surrounding the nanowire. For small size parameters, i.e., small nanowire diameters compared to the wavelength, p-polarized light (black solid curve) is scattered more efficiently than s-polarized light (red dashed curve). The ratio of the two scattering efficiencies is depicted in Figure 6.4b. For $kr = 0.23$, the ratio reveals a pronounced maximum of 140. For larger diameters, the ratio converges to 1, meaning equal scattering efficiency for incident light polarized parallel or perpendicular to the long axis.

While Mie theory for infinitely long cylinders can be used to describe the scattering anisotropy of nanowires for angles of incidence θ off the normal, it is not possible to calculate the scattering efficiency for an angle of incidence of 0°. Due to the infinite length of the nanowire, for this angle of incidence the cross sections diverge.

The parameter characterizing the scattering strength of light in a random medium is the scattering mean free path, l_s, i.e., the average distance between two scattering events
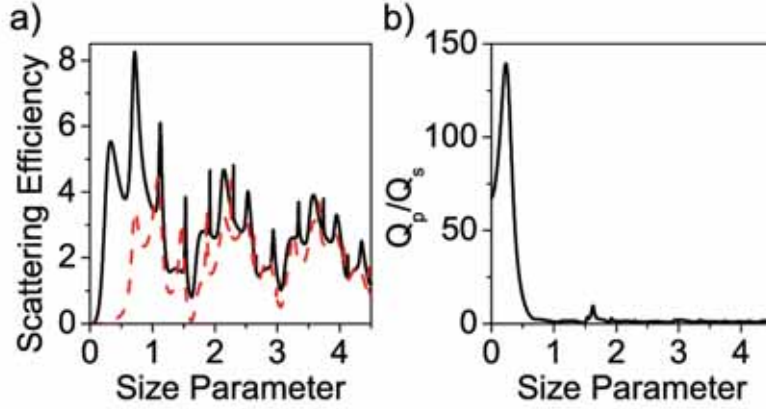
Figure 6.4: a) Scattering efficiency as a function of size parameter of an infinitely long GaP nanowire with refractive index $n = 3.26$ embedded in air for light polarized parallel (solid black curve) and perpendicular (red dashed curve) to the nanowire long axis. b) Ratio of the two scattering efficiencies.

(see Fig. 6.2), multiplied by the effective wavenumber of the medium, $k = \frac{2\pi}{\lambda} n_{\mathrm{eff}}$. A large value of kl_{s} means a long scattering mean free path compared to the wavelength, thus a weak scattering strength. The scattering mean free path of a medium consisting of randomly placed scatterers is related to the scattering cross section of the individual scatterer, σ_{s}, and the density of scatterers, ρ, by $l_{\mathrm{s}} = (\rho \sigma_{\mathrm{s}})^{-1}$. The scattering mean free path of the medium and therewith the scattering cross section of the individual scatterers can be obtained by measuring the decay of coherent transmission or the scattered intensity in the forward direction. This transmission is also known as the zero-order transmission, as it is the transmission in the same direction as the incident light beam. The zero-order transmission of light T through a scattering layer is related to the optical path length L' and the scattering mean free path l_{s} by Lambert-Beer's law

$$T = T_0 \mathrm{e}^{-\frac{L'}{l_{\mathrm{s}}}} = T_0 \mathrm{e}^{-L'\sigma_{\mathrm{s}}\rho}. \tag{6.3}$$

T_0 accounts for the Fresnel transmission at the interfaces. For determining the scattering strength kl_{s}, the effective refractive index of the random medium, n_{eff}, needs to be determined first. This effective refractive index can be defined as we did in Chapter 3 on page 34, by using Equations (3.3a), (3.3b) and (3.7) on page 36.

6.3 Vertically aligned Nanowires

6.3.1 Fabrication

GaP nanowires are grown on GaP substrates using the vapor-liquid solid (VLS) mechanism by metal-organic vapor phase epitaxy (MOVPE). The growth of the nanowires using the VLS mechanism is described in detail in Chapter 2. Ensembles of nanowires are grown during 1020 s at a temperature of 420 °C. To increase the diameter of the nanowires, shells are grown around the nanowires at a temperature of 630 °C. The growth parameters of the nanowire samples are given in Table 2.1 on page 29.

6.3.2 Experiments

To determine the scattering anisotropy of ensembles of GaP nanowires, the zero-order transmitted intensity through the nanowire layer is measured. The measurements are performed using the angle-resolved setup explained in Chapter 3 on page 43 using a Fianium supercontinuum white light source and a fiber coupled spectrometer with Si detector (Ocean Optics, USB2000). The sample was rotated so that the angle of incidence was varied from normal incidence to 60° and the incident polarization was chosen to be either s- or p-polarized (see Figure 6.5). For s-polarization, the electric field is always perpendicular to the nanowire axis, while for p-polarization and for angles of incidence larger than normal incidence, a component of the electric field is along the nanowire elongation.
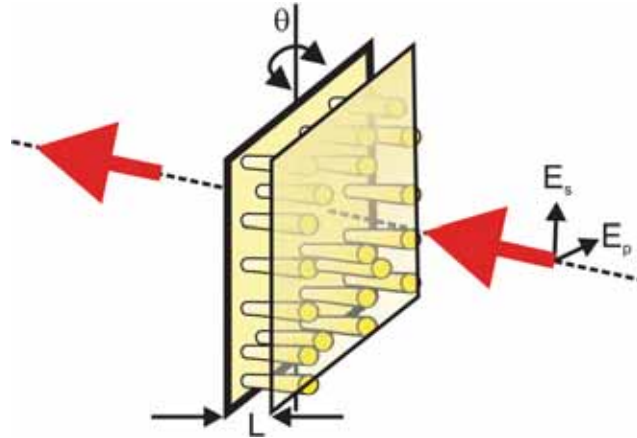

Figure 6.5: Schematic representation of the experimental setup for determining the scattering mean free path of a layer of nanowires with thickness L. A polarized plane wave is incident onto the sample of thickness L, which can be rotated along an axis perpendicular to the incident **k**-vector.

We have performed transmission measurements for normal incidence through layers of nanowires with different average diameters (12 nm, 81 nm, 90 nm, and 110 nm) as a function of wavelength. Figure 6.6 shows the transmission measurement through layers

of nanowires with d = 12 ± 4 nm (sample X, black squares), 81 ± 16 nm (XIII, red circles), 90 ± 16 nm (XIV, blue triangles), and 110 ± 18 nm (XV, olive diamonds), normalized to the transmission through a bare GaP substrate. The transmission through the nanowire layer consisting of thick nanowires is strongly reduced for shorter wavelengths, while the layer of thin nanowires is transparent for all measured wavelengths. Mie theory for infinitely long cylinders cannot be used to describe the scattering efficiency and therefore the scattering mean free path for normal incidence. However, as the nanowire diameter is much smaller than the wavelength of light, we can try to fit the transmission considering Rayleigh scattering. In the Rayleigh scattering approximation, σ_s is proportional to λ^{-4} and can be defined as

$$\sigma_s = \frac{2\pi^5}{3} \frac{d^6}{\lambda^4} \left(\frac{n_c^2 - 1}{n_c^2 + 2} \right)^2 \propto \frac{1}{\lambda^4}, \tag{6.4}$$

with d, n_c, and λ being the diameter and the refractive index of the nanowires, and the vacuum wavelength, respectively [105]. Using Equation (6.3) and σ_s obtained from Equation (6.4), the measured transmission can be fit using the nanowire density ρ as fitting parameter. We assume in these fits that the Fresnel transmission at the interfaces of the nanowire sample and the GaP substrate are similar, resulting in $T_0 = 1$. These fits are shown in Figure 6.6 with curves, where we find a good agreement for long wavelengths. While the measurements of sample XIII (red circles), XIV (blue triangles), and XV (olive diamonds) follow qualitatively the λ^{-4} trend, discrepancies between measurements and calculation are visible. For the samples with thicker nanowires (d = 110 nm, diamonds) and at wavelengths below 800 nm deviations between measurements and fits arise because of the breakdown of the Rayleigh scattering approximation. The breakdown of the approximation occurs at different wavelengths, depending on the diameter of the wires. The measurements deviate from Rayleigh scattering for wavelengths below 700 nm for the layer of nanowires with an average diameter of 90 nm. For nanowires with an average diameter of 110 nm, the measurements deviate from Rayleigh scattering for wavelengths below 800 nm. These discrepancies are not only due to a breakdown of the Rayleigh scattering approximation, but also to the nanowire elongation. The Rayleigh scattering approximation is valid when all dimensions of the scatterers are smaller than the wavelength. The diameter of the nanowires is smaller than the wavelength, but the length of the nanowires is around 1 μm and is therefore comparable to the wavelength. The transmitted intensity through the layer with nanowires with an average diameter of 12 nm normalized to the transmitted intensity through a GaP substrate is wavelength independent with a value of 50 %. For this layer, scattering is negligible as $l_s \gg L$. The reduction of the transmission is due to Fresnel reflections at the interfaces.

While we have illustrated the breakdown of the Rayleigh scattering approximation in Figure 6.6, we describe in Figure 6.7 the angular dependence of scattering in layers of nanowires. Figure 6.7 shows the measured transmission through sample XV normalized by the transmission of a bare GaP substrate for s-polarization (Fig. 6.7a) and p-polarization (Fig. 6.7b). These measurements have been done at normal incidence (black squares) and for angles of incidence of 20° (red circles), 40° (blue triangles), and 60° (olive diamonds). From the measurement and the fit assuming Rayleigh scattering in Figure 6.6, we conclude that the Rayleigh scattering approximation for normal incidence works fine
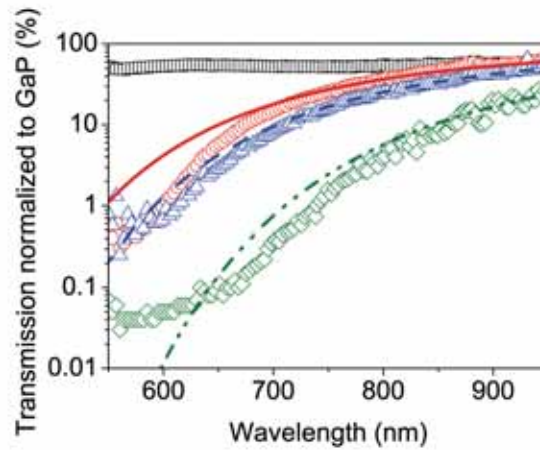
Figure 6.6: Transmitted intensity measured through sample X (black squares), XIII (red circles), XIV (blue triangles), and XV (olive diamonds) normalized to the transmitted intensity through a bare GaP substrate. The average diameter of the nanowires are 12 nm, 81 nm, 90 nm, and 110 nm, respectively. The average layer thickness are 1 μm for sample X and 1.1 μm for the three other samples. The curves are fits using Rayleigh scattering.
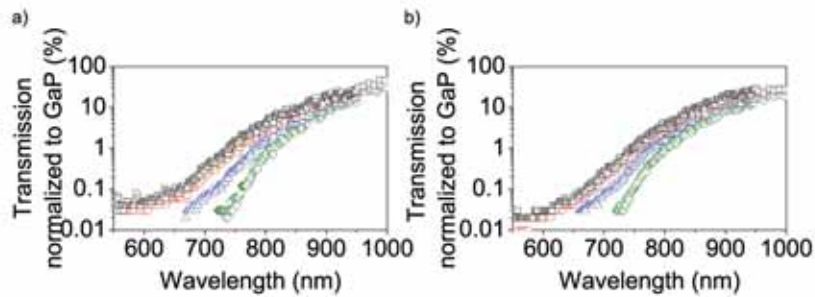

Figure 6.7: Measured transmitted intensity through sample XV normalized to the transmission through a GaP substrate as a function of wavelength for normal incidence (black squares) and angles of incidence of 20° (red circles), 40° (blue triangles), and 60° (olive diamonds) for a) s-polarization and b) p-polarization. The average diameter of the nanowires is 110 nm and the length 1.1 μm.

for wavelengths longer than 800 nm. For shorter wavelengths, the condition for Rayleigh scattering, namely that the size of the scatterers is much smaller than the wavelength, is not fulfilled. For larger angles of incidence, the transmission is further reduced. This reduction is the consequence of the longer optical path inside the sample and the shorter mean free path which results from the larger scattering cross section at larger angles of incidence. Because of the limited dynamic range of the spectrometer, trustworthy intensities of transmitted light could only be obtained for values above 0.02 %. Therefore, the measurements are cut below this value.

Using Equation (6.3), the scattering mean free path can be obtained from the measurements of Figure 6.7. The optical path length of the light traveling in the nanowire layer is $L' = L \cos \theta'$, where the internal angle θ' is determined using Snell's law and the refractive index of the the GaP nanowire layer with a GaP filling fraction of 0.6. This effective refractive index can be estimated from Maxwell-Garnett effective medium theory (Equation (3.3b) on page 34 for s-polarization and Equation (3.7) on page 36 for p-polarization). The scattering mean free path determined from the transmission measurements is given in Figure 6.8 for s- (Fig. 6.8a) and p- (Fig. 6.8b) polarization for angles of incidence of 0° (black squares), 20° (red circles), 40° (blue triangles), and 60° (olive diamonds). The scattering mean free path varies in the wavelength range of the measurements from 0.15 μm at 550 nm to around 0.8 μm at 950 nm for both polarizations. To compare the scattering strength of the GaP nanowire layer with that of strongly scattering media reported in literature [99–101], we estimate kl_s to vary in this wavelength range from 3 ± 0.4 to 9 ± 1. These values of kl_s are small, being amongst the strongest scattering samples reported so far.
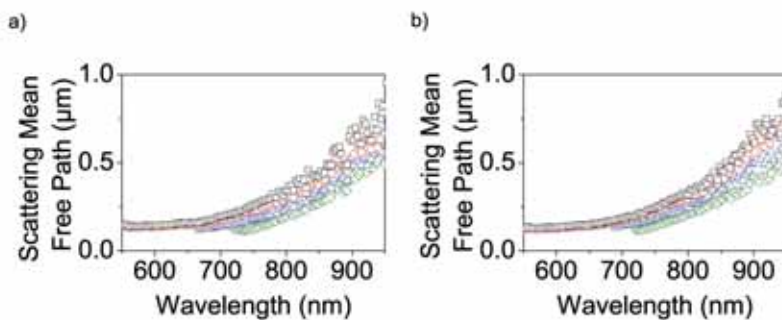

Figure 6.8: Scattering mean free path of sample XV path as a function of wavelength for normal incidence (black squares) and angles of incidence of 20° (red circles), 40° (blue triangles), and 60° (olive diamonds) for a) s-polarization and b) p-polarization.

The angle dependence of the scattering mean free path is depicted in Figure 6.9a for s- (black symbols) and p-polarization (red symbols), for wavelengths of 750 nm (circles) and 800 nm (squares), and for internal angles from normal incidence to 30°. The scattering mean free path for normally incident light at $\lambda = 750$ nm is 0.23 ± 0.01 μm, while at

λ = 800 nm it is 0.33 ± 0.01 μm. These scattering mean free paths correspond to kl_s of 3.6 ± 0.4 and 4.7 ± 0.5, respectively. The difference in the scattering mean free path of s- and p-polarization at normal incidence is due to an error in determination of the effective refractive index. While for normal incidence the calculated effective refractive index for s- and p-polarization are identical, the bending of the wires explained in Chapter 3 on page 43 might result in a slightly different refractive index for both polarizations. For larger angles of incidence, the scattering mean free path gets shorter, due to stronger scattering of light. Surprisingly, even for an internal angle of 30°, the scattering mean free path for s- and p-polarized incident light are similar.
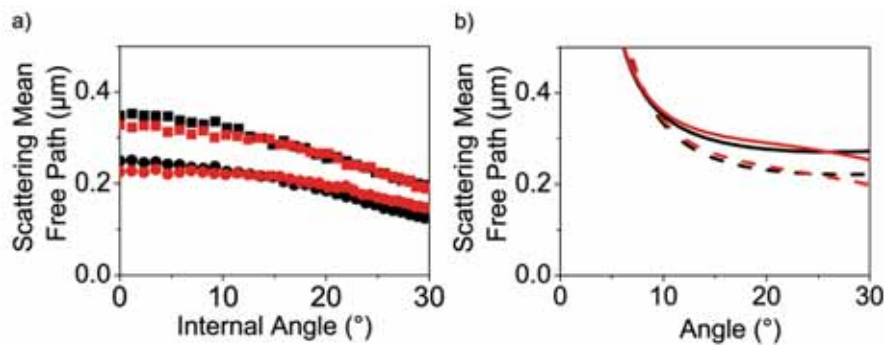

Figure 6.9: a) Measured and b) calculated scattering mean free paths of sample XV for a wavelength of 750 nm (circles, dashed curves) and 800 nm (squares, solid curves) as a function of internal angle for s-(black) and p-(red) polarization. The calculation is performed for cylinders embedded in a medium with a refractive index that varies with the angle of incidence for p-polarized light and is constant for s-polarized and using a density of nanowires of 63 μm^{-2}.

Figure 6.9b shows the calculations of the scattering mean free path for s- (black curves) and p-polarized light (red curves) for a wavelength of 750 nm (dashed curves) and 800 nm (solid curves). To determine the scattering mean free path, the scattering cross section per unit length is calculated from the scattering efficiency defined in Ref. [24] and the geometrical cross section per unit length, $\sigma_{geo} = d \sin \theta$. For this calculation we need to know the refractive index of the effective medium surrounding the nanowire. These refractive indices for light polarized parallel to the nanowire axis varies with the angle of incidence according to Equation (3.7) from 1.71 at 0° to 1.87 at 30°. The refractive index for light polarized perpendicular to the nanowire axis is 1.71 independent of the angle. These values of the refractive indices correspond to the indices used to calculate the internal angle in Figure 6.9a. The scattering mean free path is calculated using Equation (6.3) assuming a nanowire density of 63 μm^{-2}. This density is derived from the average nanowire diameter of 110 nm and a filling fraction of 0.6. The calculations also confirm that the scattering mean free paths for s- and p-polarized light are similar. On a first glance, this might be contradictory to the calculations displayed in Figure 6.4, in which a large scattering anisotropy is predicted. However, the calculations in Figure 6.4

are performed for an infinitely long GaP nanowire surrounded by air, while the nanowires in the experiment are in an effective medium with a refractive index ~ 1.7, which strongly reduces the anisotropy.

The calculations of the scattering mean free path displayed in Figure 6.9b show a small difference for both polarizations. For angles of incidence close to 0°, the calculation deviates from the measurements. Mie theory cannot be used to describe scattering by ensembles of nanowires for small angles. However, good agreement between measurements and calculations is found for angles larger than 10°. This is a remarkable result owing to the finite length of the nanowires.

In conclusion, we have presented in this section results on scattering of light by vertically aligned nanowires. We have determined the scattering mean free path from zero-order transmission measurements as a function of angle of incidence at λ = 750 nm and 800 nm. The measured scattering mean free path is confirmed for angles of incidence larger than 10° by Mie theory calculations. From the scattering mean free path, the scattering strength kl_s is determined to be 3.6 ± 0.4 and 4.7 ± 0.5 at 750 nm and 800 nm, respectively.

6.4 Nanowires grown on (100) Substrates

6.4.1 Fabrication

We have grown GaP nanowires on a (100) GaP substrate using a gold film of 0.3 nm as catalyst. The growth of the nanowires using the VLS mechanism is described in detail in Chapter 2. The nanowires on sample XVI (see page 29) are grown during 1020 s at a temperature of 420 °C. To increase the diameter of the nanowires, a shell is grown around the nanowires during 1700 s at a temperature of 630 °C.

Figure 6.10a shows a top-view scanning electron micrograph of the layer of nanowires. In principle, nanowires grown on a (100) substrate should be aligned along distinct directions since the preferred growth direction of nanowires is the <111>B direction [60]. We observe these distinct growth directions when the nanowires are grown with a short lateral growth time. Figure 5.1 on page 67 displays such a nanowire layer. However, the top-view SEM image from sample XVI (Fig.6.10a), does not reveal any preferential growth direction. The SEM image in Figure 6.10b taken under an angle of 30° shows that some nanowires grow vertical or nearly vertical, but other nanowires have a direction in the horizontal plane of the image. This discrepancy between the expected growth into the <111>B direction and the observed growth directions might be due to the long lateral growth time (1700 s) at an elevated temperature of 630 °C, at which different growth directions can be activated.

While from the SEM images it is not possible to determine a preferential nanowire direction, a measurement of the transmission contrast shows a four-fold symmetry indicating that a preferential growth direction exist. A detailed analysis of the transmission contrast is given in Chapter 5, where we have shown that the in-plane birefringence of ensembles of thin nanowires that are grown on (100) substrates can be determined by mea-

suring the transmission contrast. A minimum in transmission contrast occurs, when there is no optical retardation in the medium, i.e., when the incident polarization is aligned parallel or perpendicular to the preferential orientation of the nanowire elongation. A maximum contrast occurs, when the incident light has a component of the electric field parallel and a component perpendicular to this preferential direction. If this is the case, there is an optical retardation between both components of the electric field. The low values of the contrast for azimuthal angles of 0°, 90°, 180°, and 270° indicate that the preferential growth direction is along or perpendicular to these angles. The value of the birefringence parameter that we derive from the measurements is 0.09 ± 0.01 at 900 nm. This low value of the birefringence is in agreement with the SEM photos that do not show a clear preferential nanowire direction.
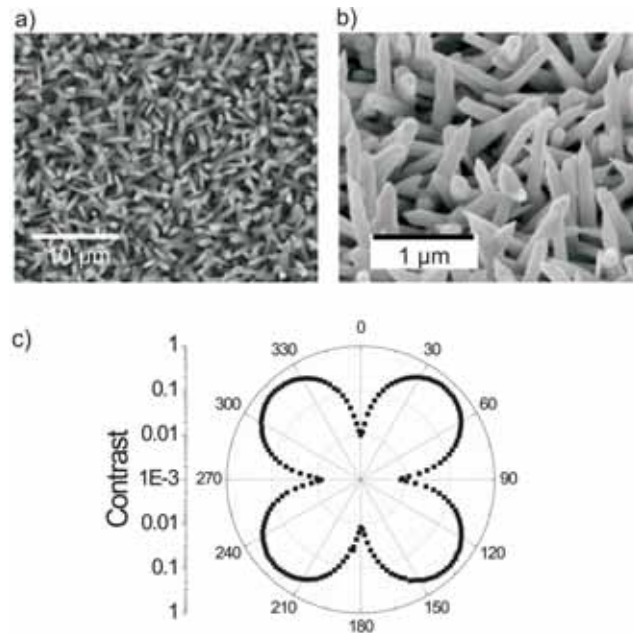

Figure 6.10: a) Top-view scanning electron micrograph of sample XVI (see Table 2.1 page 29). The nanowires are grown on a (100) substrate. b) Tilted-view scanning electron micrograph with a higher magnification taken at an angle of 30°. c) Transmission contrast as a function of the azimuthal angle of the same sample at λ = 900 nm.

6.4.2 Experimental Results: Scattering Mean Free Path

To determine the scattering mean free path of nanowires grown on a (100) substrate, the zero-order transmitted intensity is measured using a Fianium supercontinuum white light source and a fiber-coupled spectrometer. A schematic of the experimental setup is given

in Figure 6.11. The incident light is linearly polarized and the sample is rotated around its normal direction to change the azimuthal angle between the polarization-vector of the incident light and the nanowire elongation.
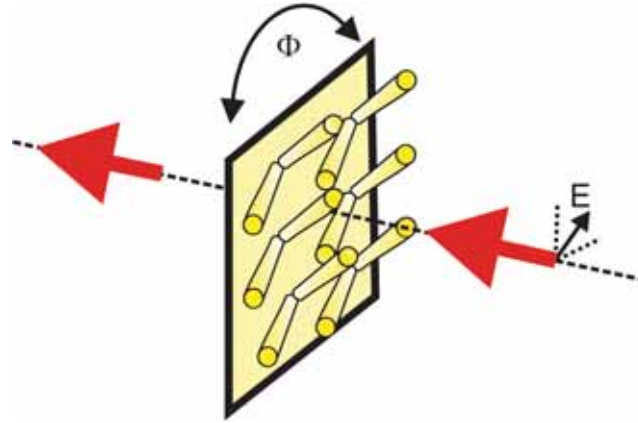

Figure 6.11: Experimental setup for measuring the zero-order transmitted light through a layer of nanowires. The incident light is linearly polarized and the sample is rotated around its normal to vary the azimuthal angle.

Figure 6.12 shows the transmission spectra of the nanowire sample normalized to the transmission through a bare GaP substrate for an azimuthal angle of 0° and 90°. Figure 6.12a and b show the same measurements in logarithmic scale and linear scale, respectively. The transmission is measured for the azimuthal angles of 0° (black curve) and 90° (red curve), at which the transmission contrast is minimum, i.e., the angles at which the the incident polarization is either along or perpendicular to the main growth direction of the nanowires. The transmission for both angles is similar, increasing for longer wavelength and with a weak oscillation that is more pronounced for $\Phi = 0°$.

Analogous to Section 6.3, we have calculated the transmission using Lambert-Beer's law (Eq. (6.3)). For this calculation, we need to define the scattering efficiency of the nanowires, the effective refractive index of the medium surrounding the nanowires, and the density of nanowires. The scattering efficiency (see Eq. (6.1)) of an individual nanowire depends on its diameter and the angle of incidence. We have fit the transmission measurements using Lambert-Beers's law and Mie theory for calculating the scattering cross section using the diameter distribution of the nanowires and the angle of the nanowires with respect to the substrate normal as fitting parameters. As we have concluded from the SEM images (Fig. 6.10) that there is not a clear preferential growth direction of the nanowires, we fit the measurements by averaging the calculation for s- and p-polarized light. From the fits we obtain a distribution of diameters in the range from 115 nm to 155 nm and we find that the angle of the nanowires with respect to the substrate normal varies from 10° to 50 °. In Figure 6.13 the calculations are shown for s-polarized (dotted curve) and p-polarized light (dashed curve) and the average of the two curves (solid curve) which is used

for fitting the measurements. For comparison the measurements for an azimuthal angle of 0° (black squares) and 90° (red circles) are included in the Figure. We find relative good agreement between the calculation of the average transmission and the measurements. However, the calculations do not reproduce well the kinks in the transmission that are observed mainly at $\Phi = 0°$. A possible origin of this discrepancy is the finite length of the nanowires. This finite length is not considered in the calculations, which were based on Mie theory for infinitely long cylinders.
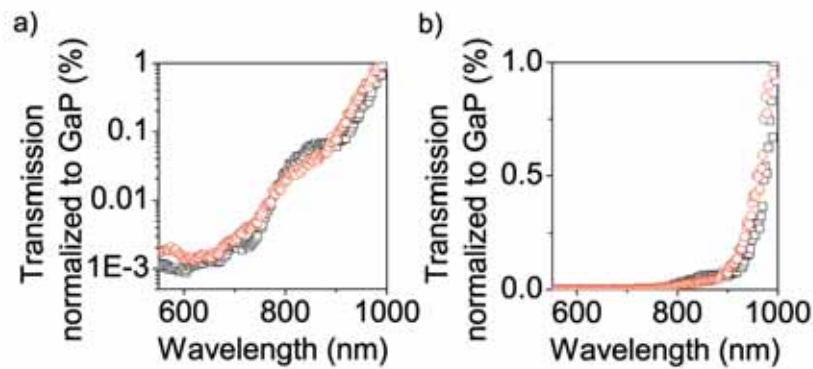

Figure 6.12: a) Measured transmitted intensity through a nanowire layer with a thickness of 1.6 μm grown on a (100) GaP substrate (sample XVI on page 29) for azimuthal angles of 0° (black curve) and 90° (red curve) normalized to the transmitted intensity through a bare GaP substrate. a) logarithmic scale and b) linear scale.

Considering that we see kinks in the transmission measurements as a function of wavelength mainly for $\Phi = 0°$, we have had a closer look at the azimuthal angle dependence of the transmission. Figure 6.14 shows the measured transmission as a function of this angle for $\lambda = 750$ nm (filled squares), 800 nm (open circles), 850 nm (open triangles), and 900 nm (open diamonds). While the measurements at $\lambda = 800$ nm and 850 nm show a maximum in transmission for 0° and 180°, the transmission at $\lambda = 900$ nm has a minimum at these angles and the maxima are shifted by 90°. As mentioned before, we attribute these variations of the transmission with azimuthal angle to the finite size of the nanowires, that cannot be explained by Mie theory.

We can determine the scattering mean free path from the transmission measurements (Fig. 6.13) by applying Lambert-Beer's law (Eq. (6.3)). Figure 6.15a shows the scattering mean free path as a function of wavelength for $\Phi = 0°$ (black squares) and 90° (red circles). The difference in scattering mean free path between both measurements is small. From the scattering mean free path, the scattering strength can be determined. Assuming an effective refractive index of the nanowire layer of 1.4, we determine kl_s to be 2.4 for $\lambda = 550$ nm. This scattering strength is smaller than that determined for normal incidence of vertically aligned nanowires and is similar to that of the strongest scattering samples to
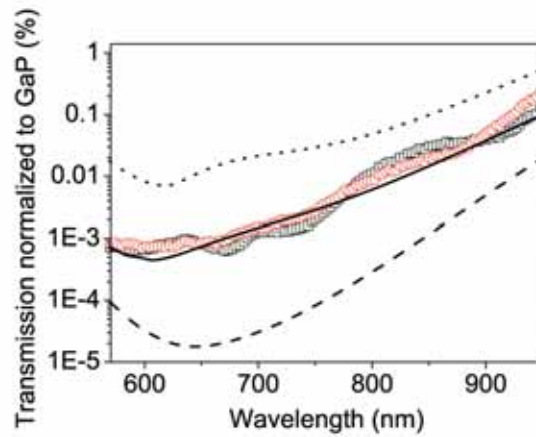
Figure 6.13: Measured transmitted intensity through a nanowire layer with a thickness of 1.6 μm grown on a (100) GaP substrate (sample XVI on page 29) for azimuthal angles of 0° (black squares) and 90° (red circles) normalized to the transmitted intensity through a bare GaP substrate. The calculations of the transmission for a nanowire diameter distribution varying between 115 nm to 155 nm and the angle of incidence varying between 10° and 50° are included for s-polarized (dotted curve) and p-polarized (dashed curve) light. The average of the two calculations is displayed with the solid curve.
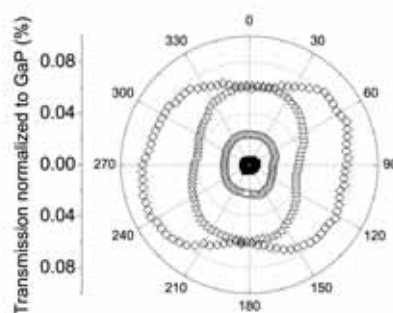

Figure 6.14: Measured transmission through a nanowire layer with a thickness of 1.6 μm grown on a (100) GaP substrate (sample XVI on page 29) normalized to the transmission through a bare GaP substrate as a function of azimuthal angle for a wavelength of 750 nm (filled squares), 800 nm (open circles), 850 nm (open triangles), 900 nm (open diamonds).

date. In Figure 6.15b the scattering mean free path is given as a function of azimuthal angle for the measurements at wavelengths of 750 nm (filled squares), 800 nm (open circles), 850 nm (open triangles), and 900 nm (open diamonds). The scattering mean free path changes slightly as a function of angle, showing that the scattering anisotropy is small in these layers.
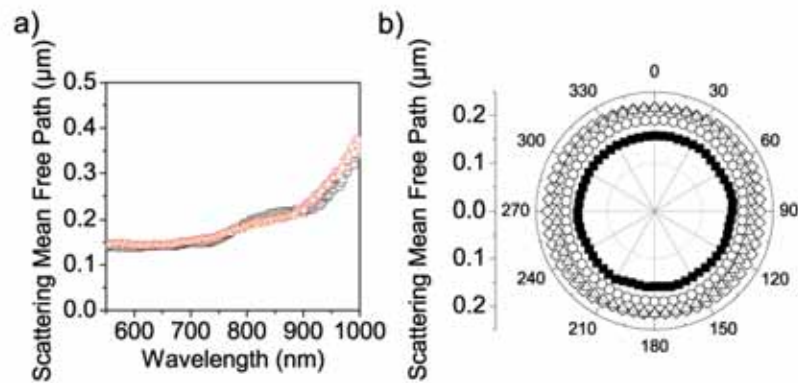

Figure 6.15: Scattering mean free path determined from the transmission measurements as a function of a) wavelength for $\Phi = 0°$ (black squares) and $90°$ (red circles) and b) azimuthal angle for a wavelength of 750 nm (filled squares), 800 nm (open circles), 850 nm (open triangles), and 900 nm (open diamonds) of sample XVI with a nanowire layer thickness of 1.6 μm.

6.5   Conclusions

We have shown that the scattering of light by nanowires is strongly dependent on their diameter. The scattering mean free path is determined in layers of vertically aligned nanowires, varying between 0.15 μm and 0.8 μm for normal incidence in the wavelength range from 550 nm to 950 nm. These mean free paths corresponds to a scattering strength kl_s of 3 ± 0.4 and 9 ± 1. For larger angles of incidence, the scattering mean free path increases. For nanowires grown on a (100) substrate, even shorter scattering mean free paths are measured with a scattering strength kl_s of 2.4, making these samples one of the strongest scattering media to date.

BROADBAND AND OMNIDIRECTIONAL ANTI-REFLECTION COATING BASED ON GaP NANORODS

Graded refractive index layers reduce the reflection and increase the coupling of light into a substrate by optical impedance matching at the interfaces. We show that ensembles of GaP nanorods form graded refractive index layers when they are conically shaped due to the increase of GaP filling fraction from the top to the bottom of the layer. Alternatively, a graded refractive index can be obtained using cylindrically shaped nanorods with a non-uniform length, which also leads to an increased GaP filling fraction at the bottom of the layer. Graded index layers can be modeled using a transfer-matrix method for isotropic layered media. We show theoretically that the light coupling efficiency into silicon can be higher than 95% over a broad wavelength range and for angles up to 60° by having a graded index layer with a refractive index increasing parabolically from the top to the bottom of the layer.

7.1   Introduction

Since Bernhard reported in 1967 that the eyes of moths are covered with nanostructures that improve the light coupling [106], the effect of these nanostructures has been investigated intensely theoretically [107–110]. Nanostructures, like the one shown in Figure 7.1 improve the light coupling into the eyes of night-seeing moths by forming a layer with graded refractive index varying from a value close to 1 at the air-nanostructure interface to the refractive index of the eye. While it was known that graded refractive index coatings can reduce the reflection and therefore improve the coupling efficiency into high index materials, fabrication of layers with a refractive index close to the refractive index of air remained challenging. Nowadays, nanostructuring techniques allow the fabrication of subwavelength structures which exhibit a very low effective refractive index when packed densely together [22, 111–123].
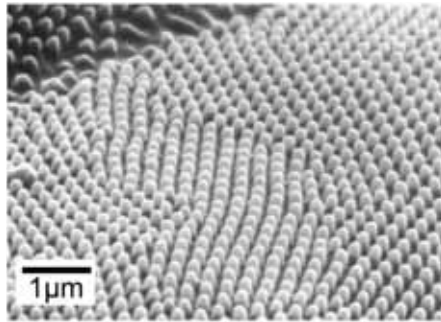

Figure 7.1: Scanning electron micrograph of nanostructures that cover the eye of a moth. P. Vukusic, Univ. of Exeter [124].

Antireflective layers can be classified into two different types: I) homogeneous layers or step index layers and II) inhomogeneous layers or graded index layers [108]. Step-index layers reduce the reflection due to destructive interference of light reflected at different interfaces [63]. The working principle of the step index layers is illustrated in Figure 7.2a. While the fabrication of single antireflection layers is well known for decades [125], the layer thickness and material have to be chosen carefully for each wavelength, angle, and substrate. The bandwidth of these coatings is lower than one octave, for example, 400-700 nm or 800-1100 nm and the angle of incidence is limited to 30° [126]. In contrast to step index layers, graded refractive index layers reduce the reflection due to a gradually increasing refractive index from the top to the bottom. This gradual increase of the refractive index leads to optical impedance matching at the interfaces and does not allow for reflections (see Figure 7.2b). Theoretically, a drastic reduction of the reflection for angles up to 80° and for a wavelength range of one order of magnitude is possible, e.g., from 400 nm to 4 μm [109].

Recently, a graded-refractive-index structure was fabricated in a bottom-up process using SiO_2 and TiO_2 nanorods deposited on AlN [117]. Using this technique, a graded index is achieved by varying the filling fraction of nanorods from one layer to the next, and
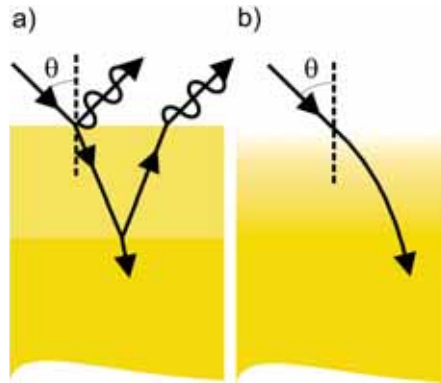
Figure 7.2: a) Step index antireflection layers reduce the reflection due to destructive interference of light reflected at different interfaces. b) Graded index coatings refract the light gradually into the substrate without allowing for reflections.

by changing the material from a low-index material at the top (SiO_2) to a material with a higher refractive index at the bottom (TiO_2). Therefore, the evaporation of two materials is necessary for these coatings. A different bottom-up approach based on chemical vapor deposition has led to recent demonstrations of antireflection coatings consisting of single materials [22]. These coatings are formed by ZnO nanowires grown on a Si substrate. The use of silicon substrates in Ref. [22] did not allow transmission measurements for visible wavelengths, and the effects of light scattering by the nanowires on the reduction of the reflection could not be determined. With top-down nanostructuring processes, the reflection of Si has been reduced by etching different kinds of nanostructures into the substrate [118–121]. With these etching techniques, very low values of the zeroth-order or specular reflection have been reported. However, it has not been unambiguously demonstrated whether this reduced reflection occurs due to light scattering by the nanostructures, to an enhanced absorption in the antireflection layer, to refractive index matching to the substrate, or to a combination of these phenomena. An important limitation of etched silicon surfaces is that the antireflection layer is also absorbing. The fabrication of nonabsorbing antireflection layers on top of absorbing substrates is thus impossible by etching. It is also worth mentioning that ultralow reflection was recently reported for layers of carbon nanotubes [127, 128]. This reduced reflection was mainly caused by absorption.

We show in this chapter that conically and cylindrically shaped nanorods form antireflection layers. We have chosen to work with GaP nanorods on top of a GaP substrate because the electronic band gap of GaP has an energy of 2.26 eV (λ = 548 nm), and transmission measurements are possible for the red and near-infrared parts of the spectrum. By measuring the transmittance and reflectance of GaP nanorods on top of a GaP substrate we unambiguously demonstrate that the reduction of the reflectance in these layers is mainly caused by a graded refractive index coating and interference in the nanorod layer, and that the role of scattering losses and absorption by the nanorod layer is secondary. The broadband reduction of the reflection is demonstrated by zeroth-order or

direct transmittance and specular reflectance measurements at wavelengths in the visible and near-infrared regions, and by angle-integrated total reflectance and transmittance measurements. To investigate the omnidirectionality of the antireflection coating, transmittance and reflectance measurements are performed for angles up to 60°.

This chapter is organized as follows. In Section 7.2 we explain the theory that describes the propagation of light through graded refractive index layers. This theory is based on the transfer-matrix method for isotropic layers. The fabrication of antireflection layers using nanorods is described in Section 7.3 together with angle-resolved transmittance and reflectance measurements and angle-integrated measurements of layers of GaP nanorods grown on top of GaP substrates.

7.2   Theoretical Background

A transfer-matrix method for isotropic layered media is used for modeling the antireflection layers [129]. This is in contrast to Chapters 3 and 4, where we modeled the birefringence of ensembles of nanowires using a transfer-matrix method for anisotropic layers based on Jones formalism. The choice for the transfer-matrix method for isotropic layered media is based on the fact that the nanorods described in this chapter have a length of 200 nm, resulting in a small aspect ratio. Due to the small aspect ratio, a small optical anisotropy is expected and confirmed by measurements of the reflection contrast (a more detailed explanation of the reflection contrast is given in Ch. 3) that show the same behavior as measured for bulk GaP. [1]
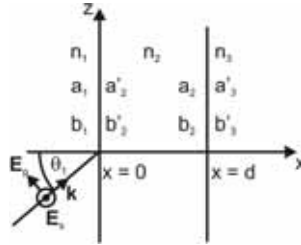

Figure 7.3: A three layer system consisting of three materials with refractive indices n_1, n_2, and n_3, respectively. The field amplitudes at the interfaces are given by a_1, a'_2, a_2, a'_3, for the right traveling waves and b_1, b'_2, b_2, b'_3 for the left traveling wave. The incident light beam with the wavevector **k** and the angle of incidence θ_1 is defined in medium 1.

In the following, we shortly introduce the transfer-matrix method. Let's consider a three layer system as the one depicted in Figure 7.3. The electric field of an electromagnetic plane wave of angular frequency ω propagating with the z-component of the wavevector k_z in the xz plane is given by

$$\mathbf{E} = \mathbf{E}(x)e^{i(\omega t - k_z z)}. \tag{7.1}$$

---

[1] GaP is a non-birefringent material.

For a detailed derivation of each component of the field see Ref. [63]. Further, we assume that the light is linearly polarized, either s-polarized, i.e., $\mathbf{E} \parallel \mathbf{y}$ or $E_x = E_z = 0$, or p-polarized, i.e., $\mathbf{H} \parallel \mathbf{y}$ or $E_y = 0$. If we assume that light is only impinging on the three layer system from medium 1, the electric field in layer 1 and 2 consists of a right- and left-traveling wave and can be written as

$$E(x) = a\mathrm{e}^{-ik_x x} + b\mathrm{e}^{ik_x x} \equiv a(x) + b(x),\tag{7.2}$$

where $\pm k_x$ are the x-components of the wave vector given by $k_x = n_\alpha \frac{2\pi}{\lambda} \cos\theta'_\alpha$ in medium α with refractive index n_α and angle inside the medium θ'_α. a and b are constant in each homogeneous layer. The amplitude of the wave traveling to the right is represented by $a(x)$, while the left traveling component is described by $b(x)$. We define the various amplitudes at the interfaces between the different media as

$$\begin{aligned}
a_1 &= a(0^-), \\
b_1 &= b(0^-), \\
a'_2 &= a(0^+), \\
b'_2 &= b(0^+), \\
a_2 &= a(d^-), \\
b_2 &= b(d^-), \\
a'_3 &= a(d^+), \\
b'_3 &= b(d^+) = 0,
\end{aligned}\tag{7.3}$$

where 0^- represents the left side and 0^+ the right side of the interface at $x = 0$. Similarly, d^- and d^+ represent the left and right side of the interface at $x = d$ (see Fig. 7.3). If we represent the left and right traveling components of the electric field as column vectors, the vectors at each side of the interface are related by

$$\begin{pmatrix} a_1 \\ b_1 \end{pmatrix} = \mathbf{D}_{1,2} \begin{pmatrix} a'_2 \\ b'_2 \end{pmatrix},\tag{7.4}$$

$$\begin{pmatrix} a'_2 \\ b'_2 \end{pmatrix} = \mathbf{P}_2 \begin{pmatrix} a_2 \\ b_2 \end{pmatrix},\tag{7.5}$$

$$\begin{pmatrix} a_2 \\ b_2 \end{pmatrix} = \mathbf{D}_{2,3} \begin{pmatrix} a'_3 \\ b'_3 \end{pmatrix}\tag{7.6}$$

where $\mathbf{D}_{1,2}$, and $\mathbf{D}_{2,3}$ are the so-called transmission matrices and $\mathbf{P}_2$ the propagation matrices that accounts for the propagation in the layer. The matrices are defined for layer α as follows:

$$\mathbf{D}_{\alpha,\alpha+1} = \frac{1}{t_{\alpha,\alpha+1}} \begin{pmatrix} 1 & r_{\alpha,\alpha+1} \\ r_{\alpha,\alpha+1} & 1 \end{pmatrix}\tag{7.7}$$

and

$$\mathbf{P}_\alpha = \begin{pmatrix} \mathrm{e}^{i\phi_\alpha} & 0 \\ 0 & \mathrm{e}^{-i\phi_\alpha} \end{pmatrix},\tag{7.8}$$

where $t_{\alpha,\alpha+1}$ and $r_{\alpha,\alpha+1}$ are the Fresnel amplitude reflection and transmission coefficients for the interface and $\phi_\alpha = \frac{2\pi}{\lambda} n_\alpha \cos\theta'_\alpha L$ is the phase change of light traveling through the layer, with L the thickness of the layer, λ the vacuum wavelength, and n_α and θ'_α the refractive index of the layer and the angle inside the layer, respectively.

From Equations (7.4)-(7.6), the amplitudes a_1, b_1, and a'_3 and b'_3 are related by the multiplication of the transmission matrix and the propagation matrix

$$
\begin{aligned}
\begin{pmatrix} a_1 \\ b_1 \end{pmatrix} &= \mathbf{D}_{1,2}\mathbf{P}_2\mathbf{D}_{2,3} \begin{pmatrix} a'_3 \\ b'_3 \end{pmatrix} \\
&= \begin{pmatrix} M_{11} & M_{12} \\ M_{21} & M_{22} \end{pmatrix} \begin{pmatrix} a'_3 \\ b'_3 \end{pmatrix} \\
&= \mathbf{M} \begin{pmatrix} a'_3 \\ b'_3 \end{pmatrix}.
\end{aligned}
\tag{7.9}
$$

The multiplication of the matrices can be represented by the matrix $\mathbf{M}$ consisting of the four elements M_{11}, M_{12}, M_{21}, and M_{22}.

The reflection and transmission of a plane wave through the three layer structure for light coming from layer 1 are defined as

$$
r = \left(\frac{b_1}{a_1} \right)_{b'_3=0}
\tag{7.10}
$$

and

$$
t = \left(\frac{a'_3}{a_1} \right)_{b'_3=0},
\tag{7.11}
$$

respectively. Using Equation (7.9), the amplitude reflection and transmission coefficients of the layered system are given by

$$
r = \frac{M_{21}}{M_{11}}
\tag{7.12}
$$

and

$$
t = \frac{1}{M_{11}}.
\tag{7.13}
$$

The reflectance R for the case that the medium of layer 1 is lossless is defined as

$$
R = |r|^2 = \left| \frac{M_{21}}{M_{11}} \right|^2.
\tag{7.14}
$$

If the bounding layers, 1 and 3, are both dielectrics, with real n_1 and n_3, the transmission T for a wave indicent with an angle θ_1 is given by

$$
T = \frac{n_3 \cos\theta'_3}{n_1 \cos\theta_1} |t|^2 = \frac{n_3 \cos\theta'_3}{n_1 \cos\theta_1} \left| \frac{1}{M_{11}} \right|^2,
\tag{7.15}
$$

with θ_3' the angle the light forms with the x axis in the third layer related to θ_1 by Snell's law.

While we explained above the transfer-matrix method for three layers, the formalism for a multi-layer structure can be easily deduced by multiplying the transmission and propagation matrices for each layer involved.

For modeling the graded refractive index of the nanorod layer, the nanorod layer is "sliced" into sublayers, each having a slightly increased refractive index with respect to the preceding layer. This slicing of the layers is illustrated in Figure 7.4.
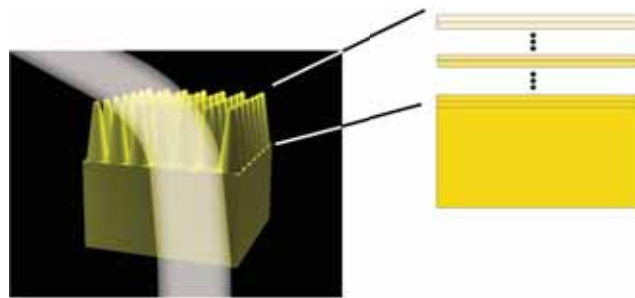

Figure 7.4: The graded refractive index of conical nanorods is modeled by "slicing" the nanorod layer into sublayers, each having a slightly increased refractive index than the layer before, indicated by the gradient in color.

Theoretically, a layer with a modified quintic refractive index profile exhibits the lowest reflection over a broad spectral and angular range [107]. However, fabrication of modified index profiles using nanorods is not trivial. We expect a quadratic index profile from conical nanorods, since the refractive index is proportional to the nanorod filling fraction and the filling fraction scales with the area. To keep the calculations as close as possible to the experiment, these calculations of the coupling efficiency into a silicon substrate are performed assuming a quadratic refractive index profile. This profile can be fabricated by growing tapered nanorods on top of a silicon substrate.

We have calculated the light coupling efficiency for bulk Si and for Si covered with a graded index coating with a quadratic index profile varying from 1.1 to 3.3, assuming that the Si substrate is completely covered with tapered nanorods. The thickness of the layer is 1 μm. For the calculations, the nanorod layer is sliced into sublayers, each having a thickness of 20 nm. The refractive index of Si varies from 3.45 to 4.25-0.044i over the calculated wavelength range from 2000 nm to 500 nm. The calculations of the graded refractive index coating for normal incidence (red solid curve) and an angle of incidence of 60° (red dashed curve) are shown in Figure 7.5 compared to calculations of the light coupling efficiency of bulk silicon (black curves) for both angles and to a standard single layer antireflection coating[2] (blue curves). The calculations of the graded refractive index show that over the

---

[2]The standard single antireflection layer with a refractive index of 1.97 and a thickness of 89 nm is plotted [130]. The thickness of the layer is chosen so that it forms a $\lambda/4$ layer at a wavelength of 700 nm for normally incident light.
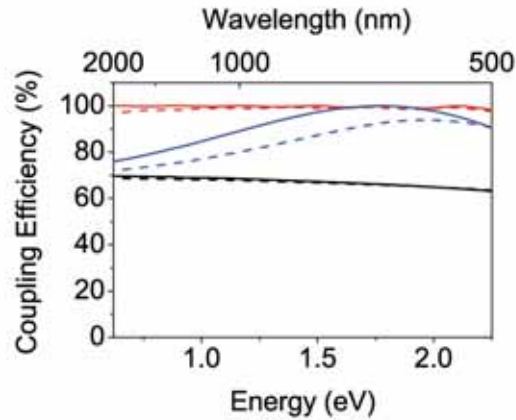
Figure 7.5: Calculated coupling efficiency of light into bulk silicon (black curves), silicon covered with a 1 μm thick graded index layer with a parabolically increasing refractive index from 1.1 to 3.3 (red curves) and silicon covered with a single layer Si_3N_4 antireflection layer with a refractive index of 1.97 and a thickness of 89 nm (blue curves) for normal incidence (solid curves) and an angle of incidence of 60° (dashed curves).

whole spectral range and also for angles up to 60° the coupling efficiency is higher than 95 %. The graded index layer increases the coupling efficiency of light into Si over a larger wavelength range and also for larger angles than the standard single antireflection layer.

7.3 Experiments

We have investigated the antireflection properties of two types of nanorods, namely conically and cylindrically shaped rods. A graded refractive index layer can be achieved in ensembles of conically shaped nanorods, due to the variation of the filling fraction of GaP along the growth direction of the rods. The layer of cylindrical nanorods shows an antireflection behavior due to a distribution of nanorod lengths which leads to a reduced GaP density toward the top of the layer.

The investigated layers of nanorods were fabricated on double-side polished GaP substrates with a thickness of 500 μm. A film of SiO_2 with a thickness of 500 nm was deposited on the backside of the substrate to avoid etching of this surface during a surface cleaning process before the growth. A more detailed description of the fabrication is given in Chapter 2. The morphology of the nanorods can be controlled by adjusting the temperature of the substrate during growth, in such a way that either vertically aligned cylindrical nanorods or conically shaped nanorods can be fabricated. The initial diameter of the nanorods is determined by the size of gold particles used to catalyze the growth, and thus determines the diameter at the top of the rod. During the vertical growth, it is also possible to induce a side-wall growth, when the temperature exceeds the critical value [37]. For one of the samples investigated, sample XVII (Table 2.1 on page 29 and Table 7.1),

the temperature was such that lateral growth is significant. The base of the nanorods is exposed to the side-wall growth for the longest time. The diameter is the largest at the base, and it gradually decreases toward the top of the rod. The apex angle of the conical shape can be adjusted, as the lateral growth is more pronounced with respect to the vertical growth at higher temperatures [37]. The other sample, sample XVIII (Tables 2.1 and 7.1), is grown at a lower temperature, where vertical growth is dominating, leading to non-tapered vertically aligned rods.

Table 7.1: Growth time and temperature of GaP nanorods. Sample XVII consists of conically shaped nanorods, while sample XVIII is formed by cylindrical structures. The averaged nanorod length and diameter at the top and bottom part of the nanorods are also listed. These values were obtained from SEM images.

Sample	Growth time [s]	Growth temperature [°C]	Length [nm]	Top diameter [nm]	Bottom diameter [nm]
XVII	600	570	178 ±25	28 ±7	63 ±9
XVIII	320	420	208 ±50	27 ±5	27±5

Figures 7.6a and c show scanning electron microscopy (SEM) images of samples XVII and XVIII, respectively. Due to tapering of the nanorods for sample XVII, the GaP filling fraction increases from the top to the bottom of the layer. For sample XVIII, an increase in GaP filling fraction occurs because of the distribution in length of the nanorods. Figures 7.6b and d show top-view SEM images of samples XVII and XVIII, respectively. The density of nanorods for sample XVIII is larger than for sample XVII, while the nanorods in sample XVII have a larger diameter at the bottom. The difference in density between both samples is due to different growth conditions, namely the gold film of sample XVII was annealed for 10 min at 570 °C; while for sample XVIII this step was left out. Variations in rod density and diameter lead to a distribution in the lengths of the rods [31]. A histogram representing the length distribution of sample XVIII is given in Figure 7.6e. This distribution was obtained by measuring the length of 56 nanorods from SEM images such as Figure 7.6c. The length of the rods varies from 50 to 250 nm, while the majority of rods have a length of 250 nm. The growth parameters and the characteristic dimensions for both samples are summarized in Table 7.1.

To further verify the structure of the nanorods, we have performed transmission electron microscopy (TEM). Figures 7.7a and b show TEM images of both types of rods. The gold particle on top is visible. The darker and lighter regions of the rods are related to twinning defects [96]. These defects do not have a significant effect on the nanorod refractive index and do not modify the reflection characteristics of a nanorod layer [18, 96]. Figures 7.7a and b show a clear difference between the conically shaped (Fig. 7.7a) and cylindrical (Fig. 7.7b) rods. For the conical rods, a tapering angle of ∼ 3° can be estimated.

We have measured the broad-band specular reflectance from and direct transmittance through the samples using the setup described in Chapter 3 on page 43. The transmittance was measured at normal incidence, while the reflectance was measured at an angle of incidence of 6° with respect to the surface normal. The resulting transmittance and
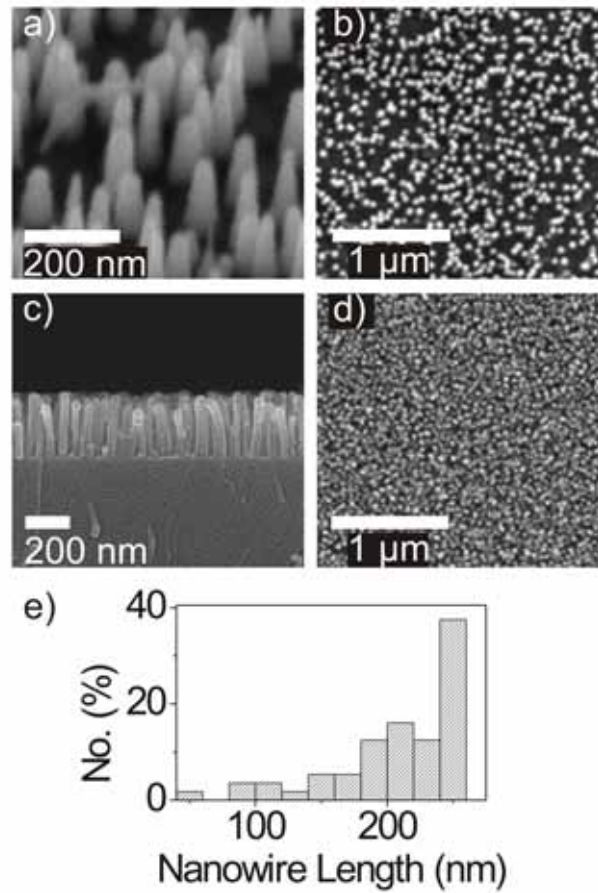
Figure 7.6: a) Scanning electron micrographs of layers of GaP nanorods. a) Tilted view and b) top-view of conically shaped nanorods (sample XVII), and c) side-view and d) top-view of cylindrical nanorods (sample XVIII). The SEM image in a) is magnified to show the tapering of the nanorods, and the image in c) shows more nanorods to display their distribution in length. e) Length distribution of the nanorods of sample XVIII.
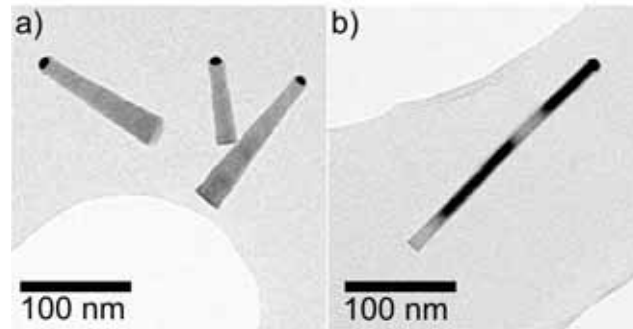
Figure 7.7: TEM images of a) conical nanorods (sample XVII) and b) cylindrical nanorods (sample XVIII).

reflectance spectra are displayed in Figures 7.8a and c, respectively, with blue circles for sample XVII and red triangles for sample XVIII. For comparison, we also plot the transmittance and reflectance measurements of a bare GaP substrate with a layer of 500 nm of SiO_2 at the backside (black squares). The sharp absorption edge visible for all samples at 2.26 eV (λ = 548 nm) corresponds to the electronic band gap of GaP. The small dip in the transmittance and the maximum in the reflectance of the GaP substrate around 1.76 eV (λ = 700 nm) are due to a Fabry-Pérot resonance in the SiO_2 layer at the backside of the GaP substrate. The scattering losses of the samples can be estimated by adding the transmittance and reflectance measurements (see Fig. 7.8e). For the GaP substrate (black squares), the transmittance plus reflectance is 100 % for energies below 2.26 eV. As expected, there are no losses in the substrate below the band gap energy of GaP. Interband absorption has a dominant influence at higher energies. For sample XVII, the transmittance is not increased with respect to the transmittance through the bare GaP substrate from $\sim$ 1.88 eV (λ = 660 nm) to 2.3 eV (550 nm). At these energies, Rayleigh scattering by the nanorods reduces the transmittance and cancels its enhancement due to the antireflection.[96] However, the transmittance increases for lower energies as scattering losses become negligible. The transmittance of sample XVII at 1.38 eV (λ = 900 nm), is increased by 20 % compared to the substrate. The small shift of the dip in transmittance and the peak in reflectance at $\sim$ 1.85 eV (670 nm), compared to the transmittance and reflectance of the substrate, is related to a Fabry-Pérot interference in the nanorod layer, which is superimposed to the reflection in the back SiO_2 layer.

The sum of reflectance and transmittance (Fig. 7.8e) for sample XVII (blue circles) increases from 85 % at 2.15 eV (λ = 575 nm) to $\sim$ 95 % at 1.38 eV (λ = 900 nm). The small reduction of the sum of reflectance and transmittance when increasing the energy can be attributed to light scattering in the nanorod layer. From the transmittance measurement of sample XVIII (red triangles in Fig. 7.8a), we can estimate an increase in the transmittance of $\sim$ 13 % relative to the bare GaP substrate for energies below the electronic band gap. This nanorod antireflection layer consists of thinner nanorods than sample XVII (see Table 7.1), so Rayleigh scattering is less pronounced in the range of wavelengths
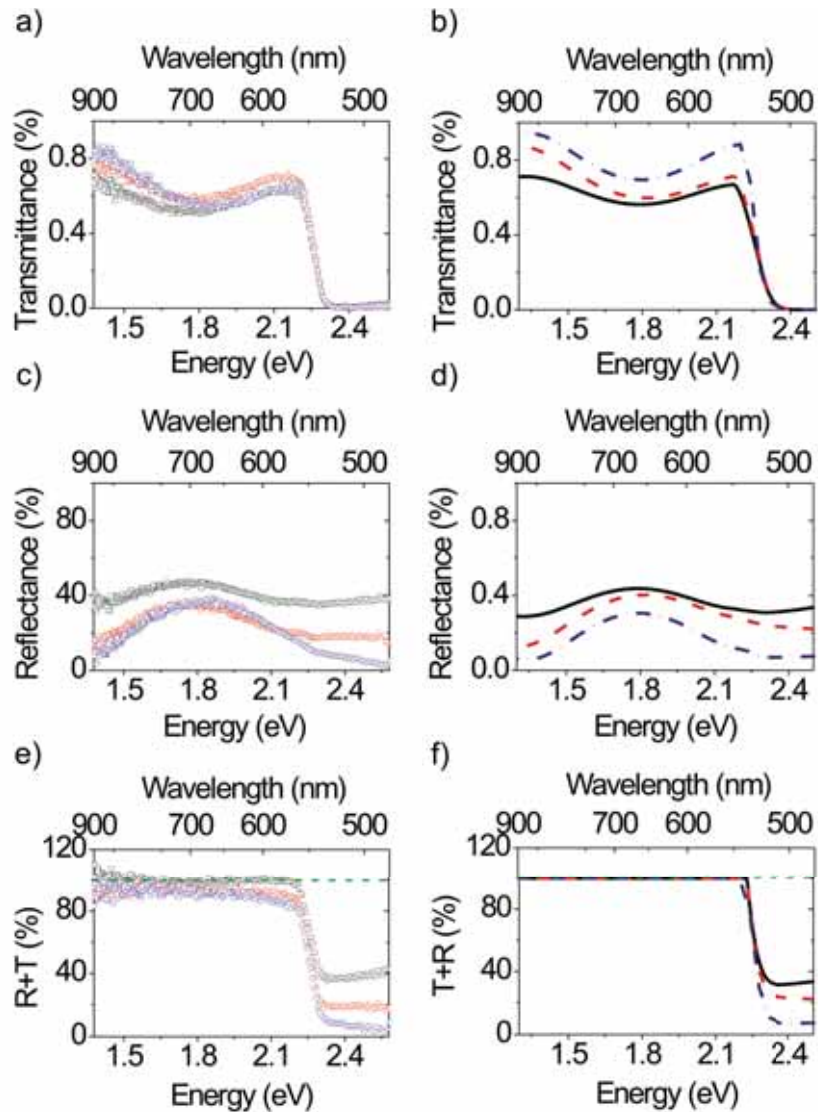
Figure 7.8: a) Measured transmittance and b) calculated transmittance for normal incidence, c) measured reflectance and d) calculated reflectance at an angle of incidence of 6°, e) the sum of measured reflectance and transmittance, and f) the sum of calculated reflectance and transmittance. The measurements (calculations) for a bare GaP substrate with one side covered by a 500 nm (490 nm) layer of SiO_2 are shown as black squares (black solid curve). The blue circles (blue dashed-dotted curve) and the red triangles (red dashed curve) correspond to the measurements (calculations) of sample XVII and XVIII, respectively.

considered. For this sample, the sum of reflectance and transmittance (red triangles in Fig. 7.8e) shows a flat wavelength response of around 95 %. The sum of reflectance and transmittance measured slightly lower than 100 % can be assigned to residual scattering in the nanorod layer and to surface roughness, due to the length distribution of the wires. We can conclude that the enhanced transmittance measurements of Figure 7.8a demonstrate that the reduction in specular reflectance reported in Figure 7.8c is not only due to surface roughness or scattering in the nanorod layer, but also to the refractive-index matching that the nanorod layer provides between air and GaP.

Figure 7.8b, d, and f show calculations of the transmittance and reflectance, done with the transfer-matrix method described in Section 7.2, of sample XVII (blue dashed-dotted curve), sample XVIII (red dashed curve), and a bare GaP substrate covered on one side with a SiO$_2$ layer with a thickness of 490 nm (black solid curve). The calculated system consists of five layers: air, nanorod layer, GaP substrate, SiO$_2$, and air. The nanorod layer is sliced into 50 horizontal sublayers, each of them having a thickness of 5 nm. We assume for sample XVII that the refractive index per sublayer increases quadratically with the length of the nanorods. This quadratic increase is based on the assumption that the filling fraction is proportional to the square of the diameter of the rods, and that the effective refractive index is proportional to the GaP filling fraction. From the calculations, we have determined a variation of the refractive index over the nanorod layer length from 1.1 up to 2.1. The length distribution of the rods of sample XVIII is determined from SEM images (Fig. 7.6e). From this length distribution, we can estimate a refractive index profile, which results in a third-order polynomial as a function of depth. The refractive index in this layer is varied from 1.1 to 1.4 over the nanorod-layer length. The calculations (Figs. 7.8b, d, and f) show the same trend as the measurements (Figs. 7.8a, c, and e). The small discrepancies can be attributed to the aforementioned scattering, which is not included in the calculations. Both measurement and calculation show a reduction for the sum of transmittance and reflectance (Figs. 7.8e and f) with respect to the bare GaP substrate for energies higher than the electronic band gap of GaP. This reduction can be attributed to an enhanced absorption in GaP due to the antireflection coating.

To determine the effect of the antireflection layer independently of the reflections in the substrate, we have performed calculations of the reflectance and transmittance of a nanorod layer on top of an infinitely thick GaP substrate (black curves, Fig. 7.9). These calculations are compared in Figures 7.9a and b to the reflectance and transmittance of a similar nanorod layer on top of a 500 μm thick GaP substrate covered with 490 nm SiO$_2$ on the backside (red curves). While there is a minor oscillation visible in the calculation assuming an infinite substrate, the calculations of the same antireflection layer on top of 500 μm GaP covered with 490 nm of SiO$_2$ on the backside show large variations in the transmittance and reflectance as a function of wavelength. Comparing both calculations, we can conclude that the modulation of the transmittance and reflectance through samples XVII and XVIII are due to Fabry-Pérot resonances in the SiO$_2$ layer in the bottom of the wafer and on the nanorod film on top. The minor oscillations in the calculation of the antireflection layer on top of the infinitely thick GaP substrate, indicates that the nanorod layer acts both as a graded-refractive-index coating and a single-layer interference coating.
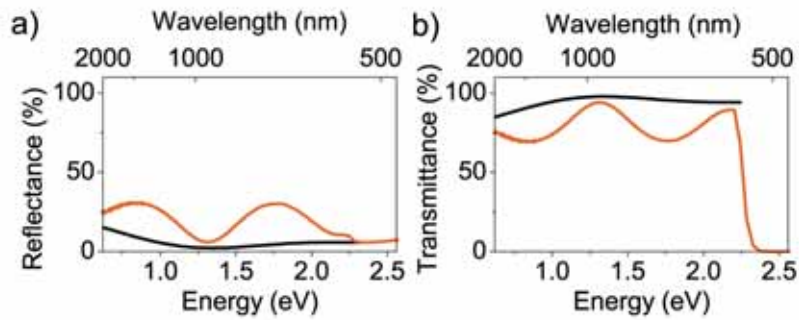
Figure 7.9: a) Calculated reflectance and b) transmittance for a graded refractive index layer with a parabolically increasing refractive index on top of an infinite GaP substrate (black curve) and on a GaP substrate with a 490 nm thick SiO_2 layer on the backside (red curve). The graded index layer has a thickness of 250 nm and the refractive index is varied from 1.1 at the top to 2.1 at the bottom.
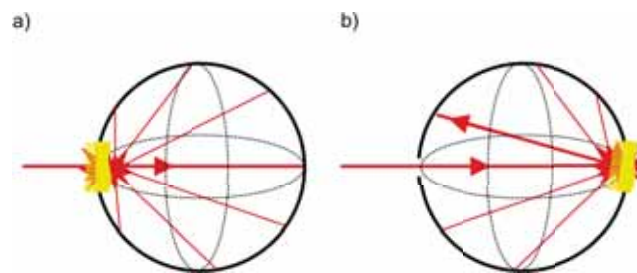

Figure 7.10: Schematic of the integrating sphere used for a) total transmittance measurements and b) for total reflectance measurements. The direct transmitted or reflected beam and the diffuse transmitted or reflected beam can be measured simultaneously by using the integrating sphere. For the reflectance measurement, the sample is mounted with an angle of $8°$ with respect to the incident light so that the specularly reflected beam does not escape from the sphere.
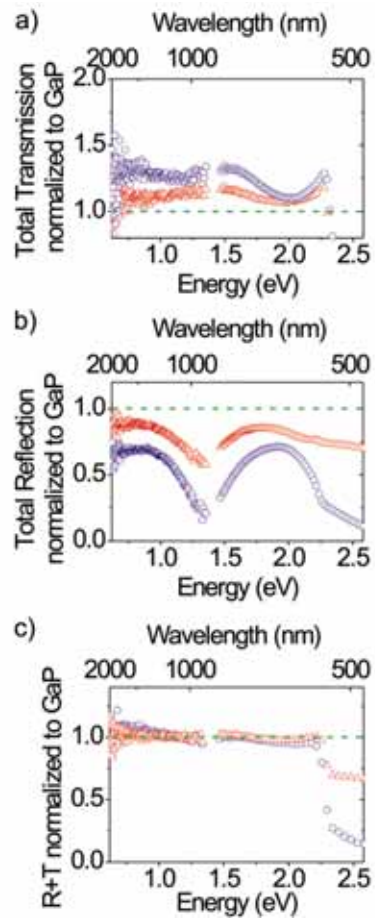
Figure 7.11: a) Total transmittance and b) total reflectance of sample XVII (blue circles) and XVIII (red triangles) normalized to the measurements on a GaP substrate. c) Sums of the total reflectance and transmittance of samples XVII (blue circles) and XVIII (red triangles) normalized to the total reflectance and transmittance of a bare GaP substrate.

In addition to direct transmittance and specular reflectance measurements, we have performed angle-integrated total reflectance and transmittance measurements for energies between 0.62 eV (λ = 2000 nm) and 2.58 eV (λ = 480 nm) using the integrating sphere PerkinElmer Lambda 950 commercial setup. The Perkin Elmer Lambda 950 spectrometer consists of a tungsten-halogen and a deuterium lamp, in combination with an integrating sphere, a photomultiplier for visible, and a PbS detector for infrared light. For the transmittance measurements, the sample was mounted in front of the integrating sphere, so that all transmitted light was collected. For the reflectance measurements, the sample was mounted at the backside of the integrating sphere with its surface normal at an angle of 8° with respect to the incident light beam, so that all the reflected light from the sample could be collected and detected. The working principle of an integrating sphere is described in Figure 7.10a in transmission and in Figure 7.10b in reflection. The integrating sphere is coated at the inside with a diffusive coating. Specularly reflected or transmitted light and the diffusely reflected or transmitted light are randomized and the intensity is equally distributed over the sphere. Measuring the intensity on each point of the sphere will lead to the same result.

Figure 7.11a shows the total transmittance of samples XVII (blue circles) and XVIII (red triangles), while Figure 7.11b displays the total reflectance measurement of both samples. These total transmittance and reflectance spectra have been normalized by reference measurements on a GaP substrate. The measurements show an increase of the total reflection for both samples with respect to bulk GaP for energies below the electronic bandgap. The overall reduction of the total reflection with respect to the substrate (Fig. 7.11b) demonstrates that the reduction of the specular reflectance of Figure 7.8c is not due to light scattering in the nanorod film; if the reduction of the specular reflectance had been caused by scattering, the angle-integrated total reflectance measurement would not have shown a decreased reflectance with respect to the GaP reference. The dip in the normalized angle-integrated reflectance at around 1.35 eV (λ = 900 nm) is caused by the aforementioned combination of a Fabry-Pérot oscillation in the SiO_2 layer at the backside of the GaP substrate and in the nanorod film. As can be seen in Figure 7.11c, the sum of total transmittance and total reflectance with respect to the bare GaP substrate is 1 for energies less than 2.26 eV, which demonstrates that there are no absorption losses at these energies. Above the electronic band gap of GaP, there is a reduction of the total transmittance plus reflectance of the nanorod layer with respect to the bare GaP substrate (see Fig. 7.11c). This reduction suggests an enhanced absorption in the nanorod antireflection layer or in the underlying substrate. In summary, these measurements show that layers of nanorods form broad-band antireflection layers that reduce the total reflectance and enhance the total transmittance from 2.25 eV (λ = 550 nm) to at least 0.62 eV (λ = 2000 nm).

To investigate the omnidirectional characteristics of these antireflection layers, we have performed direct transmittance and specular reflectance measurements of sample XVIII as a function of the wavelength in the range from 550 to 900 nm and for angles of incidence varying from 0° to 60°. This angular range was limited by our experimental setup. Figure 7.12a shows a contour image of the transmission of the nanorod sample normalized to the transmission of the GaP substrate. For all wavelengths, and at all angles, a normalized transmission exceeding 1 is observed. Figure 7.12b shows a cut to
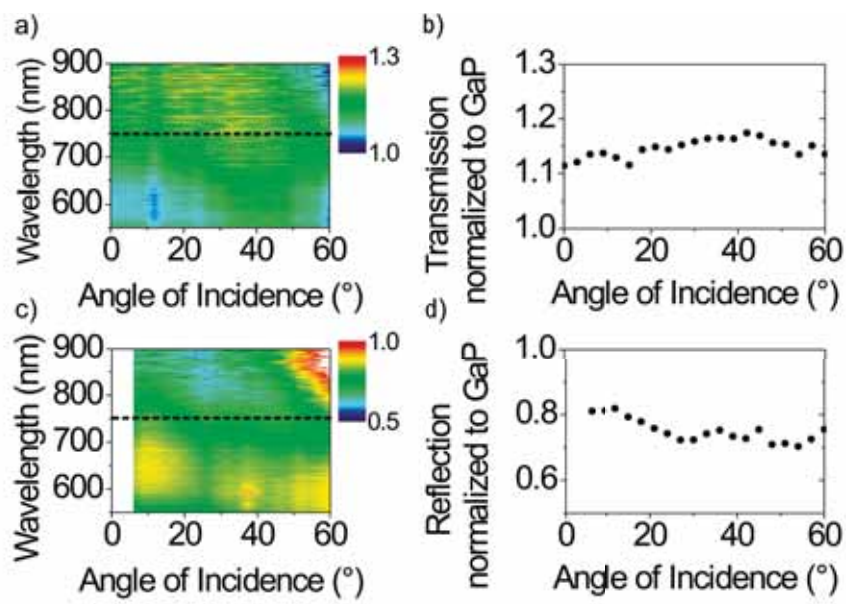
Figure 7.12: a) Angular-dependent transmission and c) reflection of a layer of GaP nanorods of sample XVIII, normalized to the transmission and reflection of a bare GaP substrate. b, d) Transmission and reflection measurements at 750 nm (along the dotted lines of a) and c)).

the transmission contour plot for a wavelength of 750 nm, taken along the black dotted line in Figure 7.12a. Figure 7.12c and d shows the reflection of sample XVIII normalized to the reflection of the GaP reference. The normalized reflection is less than 1 for all wavelengths and in the investigated angular range. Based on these measurements, we conclude that the nanorod layers act as broad-band and omnidirectional antireflection coatings.

7.4   Conclusions

In conclusion, we have investigated the anti-reflective properties of layers of GaP nanorods using wavelength- and angle-dependent transmittance and reflectance measurements. The reflectance and transmittance of graded refractive index layers are described quantitatively using a transfer-matrix method for isotropic layered media. We have shown that in theory a graded index layer with a parabolic increase of refractive index from 1 to 3.3 increases the coupling efficiency into Si to above 95 %. GaP nanorods have been fabricated by chemical vapor deposition using the VLS mechanism and we have shown that the enhanced transmittance and corresponding reduced reflectance of these layers is related to a graded refractive index in the nanorod layer. The enhanced direct transmittance and the total transmittance and reflectance presented here show that scattering and absorption are weak in these layers. The antireflection behavior over a broad wavelength and angular range, and the low amount of light scattered, renders these nanorod antireflection layers a very promising material for enhancing light coupling into solar cells or for more efficient light extraction from LEDs. This concept is further developed in Chapter 9 "Applications and Outlook".

EXTRAORDINARY BROADBAND AND OMNIDIRECTIONAL ABSORPTION IN ARRAYS OF BASE-TAPERED SEMICONDUCTOR NANOWIRES

Large-area arrays of InP nanowires are grown using arrays of gold nanoparticles patterned by substrate conformal imprint lithography. Low, omnidirectional and broadband specular and total reflectance are measured. This low reflectance is attributed to different effects due to the geometry of the nanowires, namely index of refraction matching at the air-nanowire interface, strong absorption due to the large absorption coefficient of InP, and coupling to guided modes in the tapered bottom part of the nanowires. Importantly, the coupling to guided modes for wavelengths above the electronic bandgap of InP results in enhanced light coupling into the substrate.

8.1 Introduction

In contrast to Chapter 3-6, in which we describe the propagation of light in random ensembles of GaP nanowires with a broad distribution of diameters and lengths, we demonstrate in this chapter the growth and the propagation of light in ordered arrays of InP nanowires with a well defined diameter and length. Arrays of nanowires are of great interest for different reasons. The growth rate of individual nanowires is strongly influenced by the presence of nanowires in their vicinity [31]. Such a variation in the growth rate can result in non-uniform optical or electrical properties. Besides the axial growth rate, most probably also the radial (shell) growth is affected by the catalyst density. Hence, in order to improve the nanowire uniformity, it is important to control the position and density of the catalyst particles on the substrate. While the reasons stated above consider the growth and the uniformity of the nanowires, growing ordered arrays of nanowires is also important from a purely optical point of view. The possibility of growing ordered arrays of nanowires with control of the lattice structure, the lattice constant and the diameter of the nanowires allows, for example, to design nanowire based photonic crystals. In this chapter, we describe the growth of heterostructured InP/InAsP/InP nanowire arrays and we show that optical absorption is enhanced in these layers.

Advances in nanostructuring techniques have resulted in an increased interest in enhancing the absorption in photovoltaic cells by means of nanostructures [16, 17, 22, 23, 131–139]. Increasing absorption is of great importance to improve the performance and reduce the cost of photovoltaic cells, as it allows for the reduction of the active material while maintaining efficiency. In the race towards the realization of the perfect absorber, semiconductor nanowires are promising building blocks [140]. Semiconductor nanowires have demonstrated their potential for next generation solar cells [17, 23, 40, 131, 139, 141]. Bottom-up growth techniques allow for the fabrication of nanowires hetero-epitaxially and control of the doping composition and concentration radially and axially [10, 41]. Photosensitive devices based on single nanowires and ensembles of nanowires have been demonstrated recently [17, 23, 40, 103, 131, 139]. Ensembles of nanowires are studied in relation to photovoltaics using different approaches. On the one hand, dense ensembles of nanowires forming graded refractive index layers, can be used as an antireflecting layer to couple light very efficiently into high index semiconductors [16, 22, 135]. Using this approach, the nanowires could be grown on top of solar cells as a passive antireflection layer (see Chapter 9 on page 134). On the other hand, the strong interaction of nanowires with light can be utilized to enhance the absorption in the nanowire layer. Random ensembles of vertically aligned nanowires have been demonstrated as efficient absorber material due to a reduction of specular reflectance at the interface and an increase of the optical path length in the nanowire layer by multiple scattering [136]. Solar cells based on random ensembles of non-epitaxially grown Si nanowires have been reported with a peak external quantum efficiency of 12 % [23]. Ordered arrays of dual-diameter nanopillars [137] and crystalline-core/amorphous-shell nanoneedle arrays [138] have been presented for increasing absorption in Ge. Due to the low absorption coefficient of Ge, a high nanowire density and Ge filling fraction is required for high absorption in these systems.

We demonstrate in this Chapter that it is possible to unify the strong light-nanowire

interaction and the antireflection concepts by designing a layer of nanowires with a tapered base. In particular, we demonstrate nearly perfect broadband and omnidirectional optical absorption in arrays of base-tapered InP nanowires on top of an InP substrate. Broadband and omnidirectional enhanced absorption are two of the required characteristics for improving the efficiency of solar cells. The enhancement of the absorption occurs due to the geometry of the nanowires that results in a refractive index close to unity at the top. This low refractive index increases the coupling of light into the nanowire layer due to refractive index matching with air. For wavelengths well below the electronic bandgap of InP, light is predominantly absorbed in the nanowire layer. For wavelengths close to and above the bandgap, at which the absorption is weak or absent, light is very efficiently coupled into guided modes in the tapered base and it is transferred to the substrate. In contrast to random ensembles of nanowires [136], multiple scattering of light is negligible in the ordered arrays of nanowires resulting in a very low diffuse reflectance. The measurements are described by transfer-matrix calculations and by finite-difference time-domain (FDTD) simulations.

We have chosen to work with InP because of its electronic bandgap energy of 1.344 eV (922 nm), which allows for absorption in the visible and near-infrared, where the solar irradiance is high. Further, InP is a direct bandgap semiconductor with strong optical absorption in thin layers and commonly used for photovoltaic cells [142].

In this chapter, we describe the growth of arrays of InP/InAsP/InP nanowires. For determining the effect of the InP growth time on the nanowire dimensions, we have grown three different samples with different InP growth times. We demonstrate experimentally a very low specular and total reflectance in Section 8.3 and we describe the measurements by transfer-matrix calculations and by finite difference in time domain (FDTD) simulations. In Section 8.4 we explain the occurrence of the strong absorption by analyzing the electric field and electric displacement along the nanowire.

8.2 Fabrication

We have grown arrays of InP/InAsP/InP nanowires on (111)B InP substrates using the vapor-liquid-solid (VLS) growth mechanism [26] by metal-organic vapor phase epitaxy (MOVPE). The VLS growth mechanism requires a metal catalyst particle. To achieve arrays of nanowires, we have utilized substrate conformal imprint lithography (SCIL) for patterning gold nanoparticles. A detailed description of SCIL and the nanowire growth process is given in Chapter 2. Using SCIL allows for the fabrication of large-area arrays of nanowires in a low-cost process with a high reproducibility.

For determining the effect of the InP growth time on the dimensions of the nanowires, such as the length, the diameter, and the tapering of the base, we have grown three different nanowire samples with different InP growth times. The growth parameters, the length of the nanowires, and the diameter of the bottom and top section are summarized in Table 8.1. All nanowires have a small InAsP heterostructure along the growth direction. A detailed description of the heterostructure is given in the Appendix to this chapter.

Figure 8.1 shows a top-view scanning electron micrograph of sample XIX (a) and three

Table 8.1: Parameters of arrays of InP nanowires including growth time of InP and InAsP, length of the tapered and straight part of the wire, and diameter at the base and top.

Sample	Growth time InP-InAsP-InP [s]	Length tapered part [μm]	Length straight part [μm]	Base diameter [nm]	Top diameter [nm]
XIX	1800-10-1800	1± 0.1	2± 0.1	270 ± 20	90 ± 5
XX	5400-50-5400	2.5± 0.1	2.5± 0.1	413 ± 16	99 ± 2
XXI	7200-50-7200	total length: 7.5± 0.5		-	130 ± 5

SEM images with different magnifications where the sample was tilted by 30°. The top-view image (Fig. 8.1a) shows the square lattice of the nanowires with a pitch of 513 nm. The hexagonal shape of the nanowires reveals the crystallographic structure of the nanowires. The tilted-view image with the lowest magnification (Fig. 8.1b) shows a periodic pattern over a large region, but also some missing wires. By counting the missing wires, the defect rate is estimated to be 2.3 %. The two tilted-views with higher magnification (Fig. 8.1c and d) show that the nanowires grow with a tapered base and a straight top part. The diameter of the base and the top part are given in Table 8.1. The tapering of the nanowires results in an increase of InP filling fraction from around 2.3 % at the top to 21 % at the bottom. We attribute the tapering of the bottom section to a short surface diffusion length of the precursors (see Fig. 2.4 on page 24), induced by a high temperature annealing step before the growth of the wires.
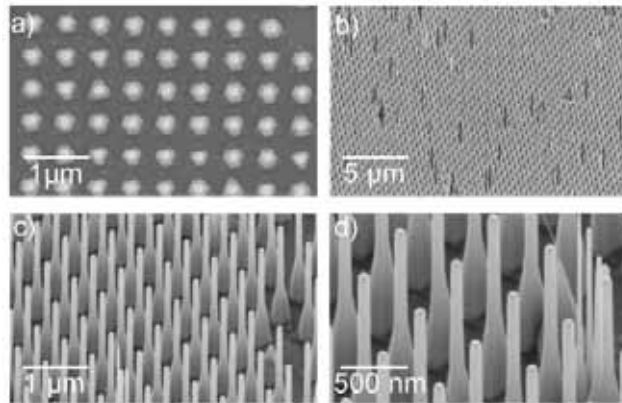
Figure 8.1: Scanning electron micrographs of sample XIX a) top-view, b), c) and d) tilted views with different magnifications.

Sample XX is fabricated with a longer InP growth time and a longer heterostructure growth time than sample XIX. From the cross-sectional SEM image in Figure 8.2a, the length of the nanowires can be estimated to be 5 μm ± 0.2 μm. Similar like sample XIX, the base is tapered and the top part is straight. A few nanowires are longer than the

majority. The tilted-view image in Figure 8.2b shows that some nanowires are kinked, i.e., the bottom section of the nanowire grows along the <111> direction but during growth the nanowire growth direction changes. In this sample, 5.5 % of the wires are missing. The tilted view image with higher magnification shows that the nanowires have a straight top part, while the tapered part is hardly visibly due to the long length of the nanowires.
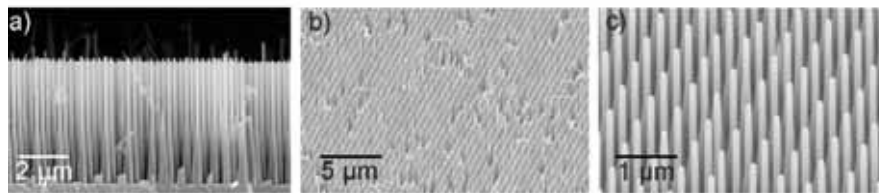

Figure 8.2: Scanning electron micrographs of sample XX a) cross-section, b), and c) tilted views with different magnifications.

Increasing the growth time further to 14450 s results in nanowires with a length of 7.5 μm $\pm$ 0.5 μm. The side-view image of sample XXI (Fig. 8.3a) shows that the nanowires cluster together at the top. The nanowires in the front of the image are broken. Most probably the wires broke while cleaving the sample. The top-view SEM image (Fig. 8.3b) shows kinking of the nanowires, but the periodic pattern is still visible. The kinking of the wires is also visible in the tilted-view image (Fig. 8.3c). More than 14 % of the wires of this sample are missing or kinked. From these SEM images, the diameter of the bottom part could not be determined. The increase of the number of kinks with longer nanowire growth time can be attributed to different surface diffusion lengths of TMIn and PH_3. When the distance of the catalyst particle to the substrate increases, the III/V ratio of precursors changes, resulting in a change of the growth condition.
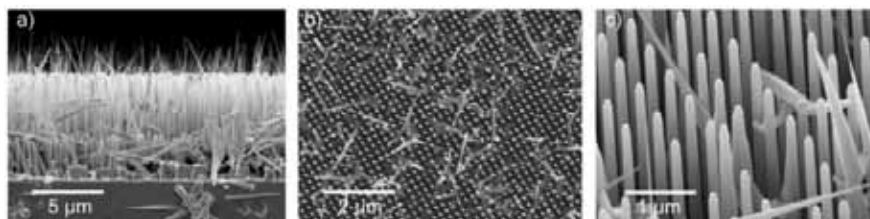

Figure 8.3: Scanning electron micrographs of sample XXI a) cross-section, b) top-view, c) tilted view.

We have studied the optical properties of sample XIX more in detail. This is the most homogeneous sample. For the following measurements, the heterostructure is not relevant, as the absorption introduced by this heterostructure is negligible. However, the presence of the heterostructure allows for different measurements, such as measurements of the modification of the emission of light sources embedded in arrays of nanowires. These measurements are not discussed further in this thesis.

8.3   Optical Experiments and FDTD Simulations

Looking by eye at the array of base-tapered InP nanowires already reveals interesting physics. Figure 8.4 shows a photograph of sample XIX. The region of the sample where the nanowires are grown is black, indicating a high absorption. The shiny InP substrate is visible at the edge, where no nanowires are grown.
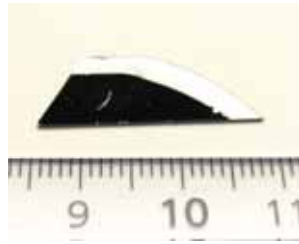

Figure 8.4: Photograph of sample XIX (see Table 8.1). The region covered with nanowires is black, indicating high absorption. No nanowires are grown on the side of the sample and the shiny InP substrate is visible.
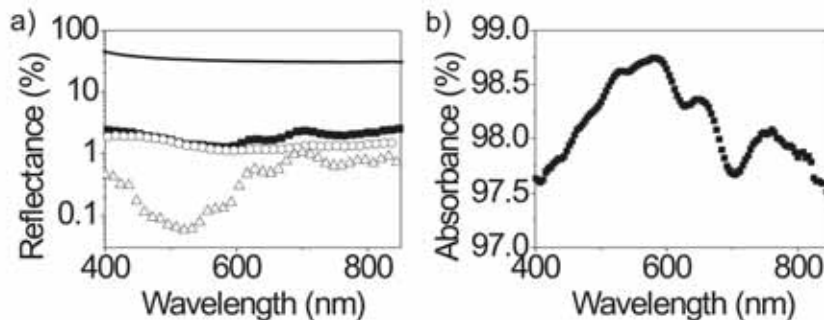
Figure 8.5: a) Measured total reflectance (squares), non-specular reflectance (circles), and specular reflectance (triangles) of sample XIX (see Table 8.1) as a function of wavelength for an angle of incidence of 8°. The solid curve shows the measured total reflectance of bulk InP for comparison. b) Absorbance in sample XIX determined from the reflectance measurements.

For a quantitative analysis of the total absorbance of the base-tapered InP nanowire array, we have measured the angle-integrated or total reflectance of the nanowire layer using the integrating sphere setup described in Chapter 7 on page 104. We have measured the total reflectance of sample XIX and that of an InP substrate for wavelengths between 400 nm and 850 nm. These measurements are normalized by the reflection of a white-standard to obtain the absolute reflectance of the array. The total reflectance measurement on the InP substrate shows that around 40 % of the incident light is reflected by

the InP (black curve in Fig. 8.5). This measured reflectance is in agreement with that determined from calculating the Fresnel reflectance at the air/InP interface for an angle of incidence of 8°. The total reflectance measurement of sample XIX (Fig. 8.5a, squares) shows an overall reduction of the reflectance with respect to a bulk InP substrate (black curve in Fig. 8.5a) with a minimum reflectance of 1.25 % at a wavelength of 580 nm. Additionally, we have measured the non-specular reflectance of sample XIX (circles in Fig. 8.5a) by making a small opening in the integrating sphere in such a way that the specularly reflected light escapes from the sphere. The difference of the total and the non-specular reflectance measurement provides the zero-order or the specular reflectance (triangles in Fig. 8.5a). The specular reflectance achieves values as low as 0.05 % at a wavelength around 510 nm. The non-specular reflectance for the wavelength range between 400 nm and 600 nm can be attributed to diffraction of the incident light into higher reflection orders due to the regular pattern and to diffuse reflection due to defects in the array.

Because InP absorbs in the measured wavelength range, and as the InP nanowires are grown on top of a 300 μm thick InP substrate, we can determine the total absorbance A_T of the sample by $A_T(\%) = 100\% - R_T(\%)$, with R_T the measured total reflectance. The total absorbance is displayed in Figure 8.5b, and it is higher than 97.5 % in the measured spectral range with a maximum of 98.7 % at 580 nm.
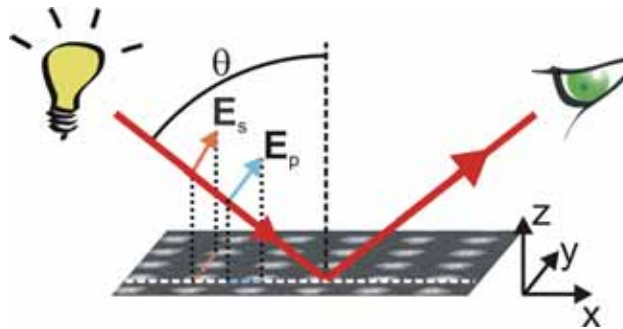

Figure 8.6: Schematic representation of the specular reflection measurement setup. The polarization of the incident light is defined with respect to the pattern of the nanowire layer. S-polarized light has only an electric field component along the y-direction, while p-polarized light has a component along the x-direction.

To study the low reflectance in more detail for a wider range of angles, we have measured the angle-resolved specular reflectance for angles of incidence from 6° to 60°. This measurement is performed using the angle resolved measurement setup described in Chapter 3 on page 43. A schematic representation of the measurement configuration is given in Figure 8.6 illustrating the alignment of the polarization of the incident light with the pattern of the sample. The sample was illuminated using a collimated beam of a fiber-coupled supercontinuum light source (Fianium SC400-PP), and the spectra were obtained using a fiber-coupled Si spectrometer (Ocean Optics, USB2000) for the visible and a fiber-coupled InGaAs spectrometer (Andor iDus) for the near-infrared.

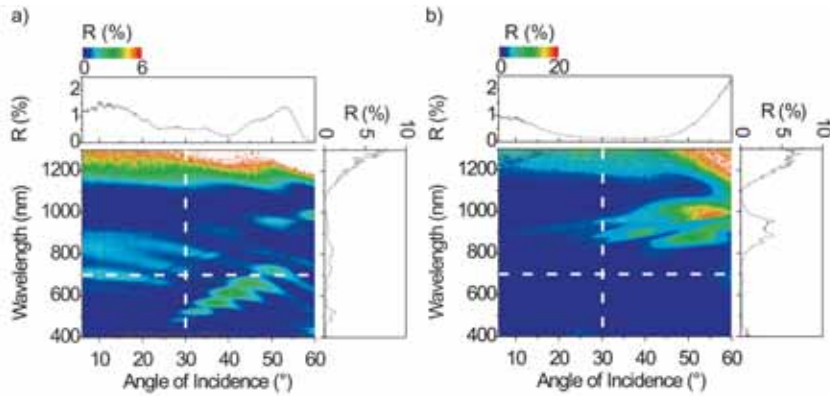We have measured the reflectance for s- and p-polarized incident light. Figure 8.7a

Figure 8.7: Measured specular reflectance of sample XIX for a) s-polarized light and b) p-polarized light as a function of angle of incidence and wavelength. The curves correspond to cuts along the dashed lines.

shows the measurement for s-polarization, while Figure 8.7b shows the measurement for p-polarization as a function of the angle of incidence and wavelength. A very low reflectance is measured for both polarizations. For s-polarization, the reflectance is low over the whole measured spectral and angular range, with a maximum reflectance of 4 % at 40° and 650 nm. The reflectance shows Fabry-Pérot oscillations due to the finite thickness of the nanowire layer. Surprisingly, the reflectance is also very low for all angles in the wavelength range between 900 nm and 1100 nm. Considering that the wavelengths in this range are longer than the electronic bandgap of InP, the low reflection cannot be attributed to absorption but to an increased transmission into the substrate.

For p-polarization (Fig 8.7b), a comparable low reflectance is measured. The dip for wavelengths between 900 nm and 1100 nm is visible, but does not cover the complete angular range measured. Overall, the reflectance shows maxima and minima for different wavelengths and angles than the s-polarized reflectance.

While we have measured a very low reflectance for both polarizations, we focus on the analysis of the s-polarized reflectance. In the following, we describe the maxima and minima in the measurements using transfer-matrix calculations and FDTD simulations.

We have performed transfer-matrix calculations [129] of a 4-layer system consisting of air, the straight part of the nanowires, the tapered part of the nanowires with a graded refractive index, and the InP substrate. These calculations, which are used to fit the Fabry-Pérot oscillations, assume that the nanowire layer is a homogenous medium with an effective refractive index and extinction coefficient. For describing the tapered part of the nanowire layer, the layer was "sliced" into sublayers with a thickness of 20 nm and a gradually increasing refractive index and extinction coefficient according to the method described in Chapter 7 on page 97. The refractive index is obtained by fitting the period of the Fabry-Pérot oscillations, while the extinction coefficient is obtained from the intensity of the reflectance. The extinction coefficient includes all losses of the specular reflection,
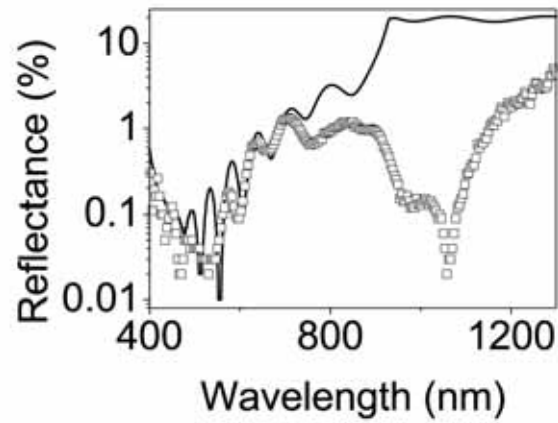
Figure 8.8: Measured (symbols) specular reflectance of sample XIX and fit using the transfer matrix method (curve) for an angle of incidence of $8°$.
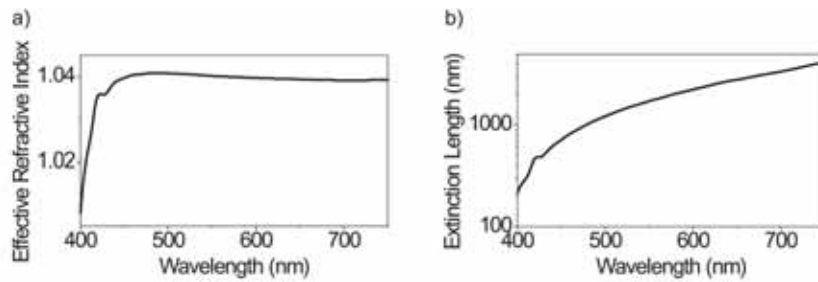

Figure 8.9: a) Effective refractive index and b) extinction length of the InP nanowire layer obtained from transfer-matrix fits to the measurements.

117

i.e., absorption, diffraction, and diffuse scattering of the nanowire layer. Figure 8.8 shows the measured reflectance (symbols) for an angle of incidence of 8° together with the calculated reflectance (curve) using the transfer-matrix method. The effective refractive index and the extinction length, defined as $\frac{\lambda}{4\pi k_{\mathrm{eff}}}$, where k_{eff} is the extinction coefficient, are displayed in Figure 8.9a and 8.9b, respectively. The effective refractive index of the straight part of the nanowires is lower than 1.04 over the measured wavelength range resulting in nearly perfect refractive index matching at the interface and very efficient coupling of light into the nanowire layer. The effective extinction length increases with wavelength because of a decrease of the absorption coefficient of InP. For wavelengths longer than 800 nm the transfer-matrix method fails in describing the measurement and the low specular reflectance for wavelength between 900 nm and 1100 nm is not reproduced in the calculation. The disagreement at long wavelengths between the measurement and the transfer-matrix calculation is, as we will show later, due to the coupling of the incident light into guided modes supported by the tapered part of the nanowires. This coupling cannot be taken into account by the effective medium used in the transfer-matrix model.
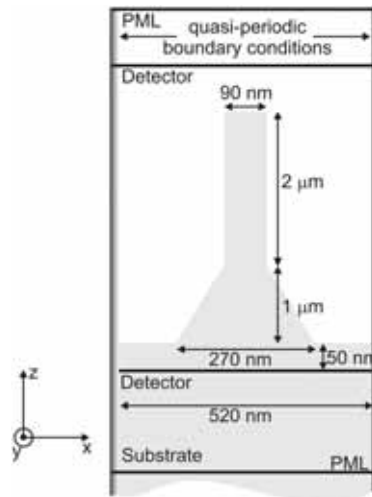

Figure 8.10: Schematic representation of the design and dimensions used for the FDTD simulations.

To understand the effect of the base-tapered nanowire geometry and the periodicity of the nanowires on the reflectance, we have performed FDTD simulations. The simulations were performed as follows: We have used an in-house developed FDTD program [143] on a computational domain consisting of a nanowire on a semi-infinite substrate (see Fig. 8.10). The domain has quasiperiodic boundary conditions [144] in the horizontal directions and absorbing perfectly matched layers (PML) boundaries [145] in the vertical directions. The dispersion of the permittivity of InP is taken into account by fitting the refractive index of InP with a Lorentz model above and below the bandgap [146], separately. The spectral response of the nanowire layer is obtained by using a short 0.5 fs
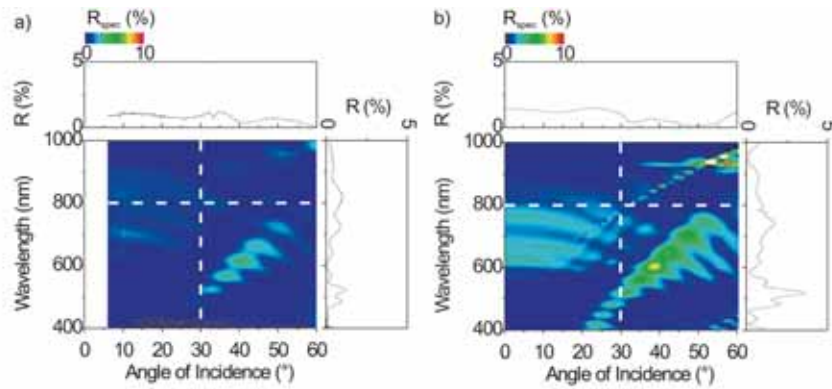
Figure 8.11: a) Measured s-polarized reflectance of sample XIX and b) FDTD simulation of the specular reflectance of the nanowire layer. The curves correspond to cuts along the dashed lines.

incident pulse with constant transverse wavenumber and Fourier transforming the simulated time-domain data. The reflectance and transmittance are computed from the fields in a plane above the nanowire and 50 nm in the substrate, respectively. The FDTD simulation of the specular reflectance as a function of wavelength and angle of incidence is shown in Figure 8.11b. For comparison, Figure 8.11a shows the s-polarized reflectance measurement. A good qualitative agreement between measurements and simulations is obtained, reproducing the Fabry-Pérot oscillations, the low reflectance in the wavelength range between 900 - 1000 nm, and the band of higher reflection for angles of incidence between 20° and 55° and wavelengths between 450 nm and 800 nm. This band can be attributed to the periodicity of the nanowire array as FDTD simulations for different nanowire periods (not shown here) show a shift of the band. The small qualitative differences between measurement and FDTD simulation can be assigned to the following reasons: i) The values of complex permittivity of InP used in the simulations are those of zinc-blende InP [146], while the nanowires grow with wurtzite structure. ii) The minor disorder of the nanowire layer, which is not included in the simulations, gives rise to non-specular reflection (see Figure 8.5) resulting in a reduction of the measured specular reflection. iii) The nanowires are approximated to a cylindrical shape with conical base, while the nanowires have a hexagonal shape. We have chosen this approximation because the hexagonal shape changes from nanowire to nanowire (see Figure 8.1) .

Since we have performed measurements using InP nanowires grown on an InP substrate, we cannot conclude from the measurements if the strong absorbance and the reduced reflectance are solely due to enhanced absorption in the nanowire layer or also to enhanced light coupling into the substrate. Therefore, we have simulated the total reflectance using FDTD in the same way as described above by assuming a substrate with an identical real part of the refractive index of InP, but by ignoring absorption. In Figure 8.12a, we present the angle-integrated simulated reflectance (black solid curve) and transmit-

tance (red dashed curve) of nanowires on top of a non-absorbing substrate. Fabry-Pérot oscillations are visible in both simulations. The pronounced dip in the reflectance at a wavelength of 540 nm is due to the Rayleigh anomaly, i.e., the angle and wavelength at which a diffracted order of the structure becomes evanescent. The sharp increase of the transmittance at 920 nm is due to the absence of absorption in the nanowire layer for wavelengths longer than the electronic bandgap of InP. Figure 8.12b displays the absorbance in the nanowire layer obtained from the simulated reflectance and transmittance. We estimate from Figure 8.12 that around 80 % of the light is absorbed by the base-tapered nanowire layer at wavelengths between 550 nm and 900 nm and more than 90 % is absorbed for shorter wavelengths. For wavelengths longer than the electronic bandgap, the absorption drops to very low values. This residual absorption in the simulation is due to the definition of the material constants in the FDTD simulation. Comparing the wavelength-integrated absorbance in the layer of base-tapered nanowires to that in a layer with the same InP volume as the base-tapered nanowires, we obtain that the absorbance is enhanced by 40 % for wavelengths between 400 nm and 900 nm.
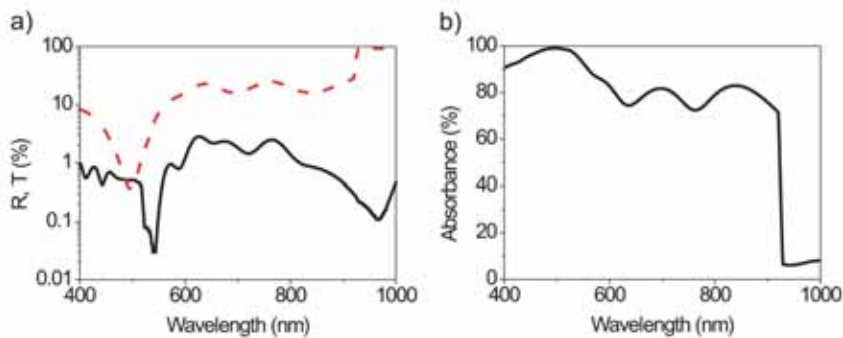

Figure 8.12: a) Simulated angle-integrated reflectance (black solid curve) and transmittance (red dashed curve) of InP nanowires on top of a non-absorbing substrate at normal incidence. b) Simulated absorbance of the nanowire layer. For wavelengths longer than 920 nm, at which InP does not absorb, more than 90% of the incident light is coupled into the underlying substrate. The calculated absorbance shows that around 80 % of the incident light is absorbed by the base-tapered nanowire layer.

8.4 Near-field Analysis

The origin of the broadband low reflectance and the maxima and minima occurring in the measurement can be found by analyzing the electric and displacement field in the nanowire layer. These fields have been obtained from the FDTD simulations and are displayed in Figure 8.13. The field component in this figure corresponds to the y-component, which is dominant in the nanowire layer. The angle of incidence is set to 40° and the simulations are performed at four different wavelengths, namely 505 nm (Figures 8.13a and e), 605 nm
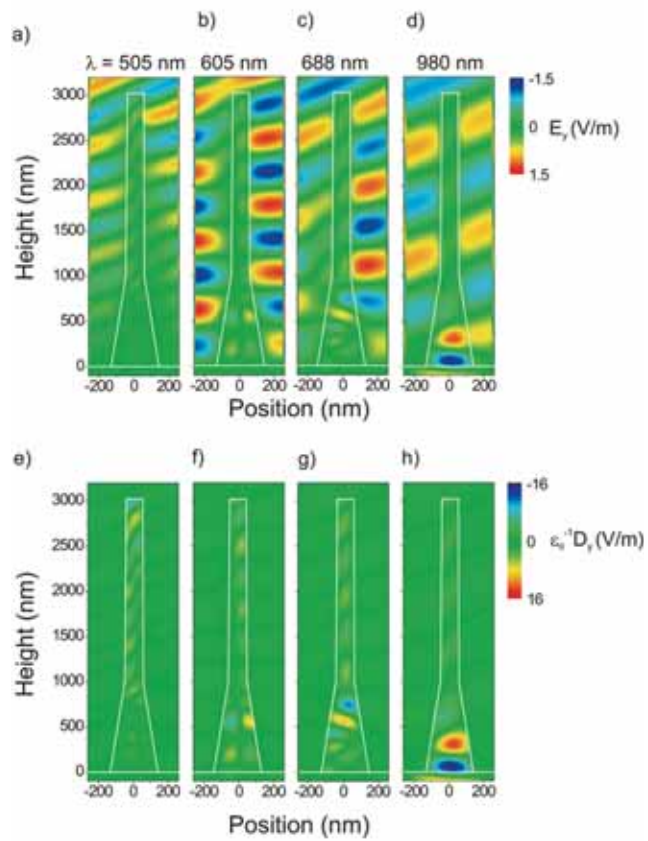
Figure 8.13: Simulated electric field and electric displacement field in a plane along the nanowire axis for an angle of incidence of 40° for wavelengths of 505 nm (a,e), 605 nm (b,f), 688 nm (c,g), and 980 nm (d,h).

(Figures 8.13b and f), 688 nm (Figures 8.13c and g), and 980 nm (Figures 8.13d and h). The displacement field is useful to visualize the field inside the nanowires, as this field is magnified by a factor given by the permittivity of InP. At 505 nm (Figure 8.13a), InP absorbs strongly and the electric field does not reach the substrate. At this wavelength, the displacement field is concentrated at the top of the nanowire (Figure 8.13e), indicating that most of the absorption occurs at the top. From the equal tilt of the wave fronts above and inside the nanowire layer we can conclude that the light is transmitted into the layer with negligible refraction. This absence of refraction confirms that the nanowire layer has a low effective refractive index with a value close to 1, as it was determined from transfer-matrix fits to the measurements. The combination of strong absorption and low refraction explains the low reflectance from the sample at short wavelengths. At 605 nm (Figure 8.13b) and 688 nm (Figure 8.13c), InP absorbs only moderately [146]. The displacement field (Figures 8.13f and g) shows that next to some absorption in the straight part of the wire, the tapered region plays an important role in the high absorbance and low reflectance of the sample. Light is efficiently coupled to guided modes in the tapered InP region, resulting in high internal fields in this part of the nanowires. Below the bandgap energy of InP, at a wavelength of 980 nm, there is no absorption. At this wavelength, the reflectance is remarkably low. The calculation of the fields (Figures 8.13d and h) reveals that the incident light couples very efficiently to the lowest order waveguide mode in the tapered region and it is fully transmitted into the InP substrate. Therefore, from the near-field simulations, we can conclude that for short wavelengths light is absorbed in the straight part of the wires, while the tapering of the nanowires is essential for the strong absorption at longer wavelengths. In the wavelength range between 900 nm and 1000 nm, where a very low reflectance is measured, the incident light is guided efficiently into the substrate by the tapered part of the nanowires.
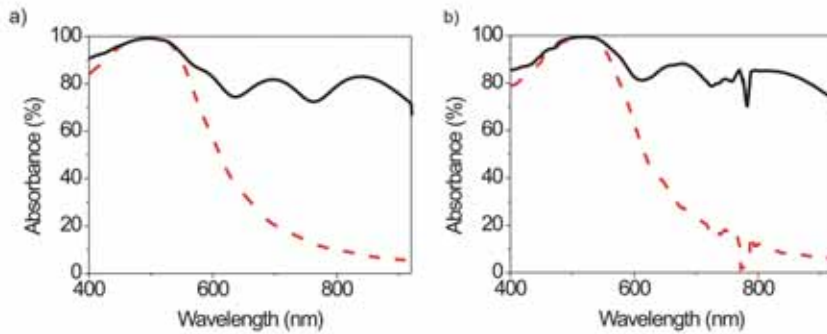

Figure 8.14: Simulated absorbance of base-tapered nanowires (black solid curve) and straight nanowires (red dashed curve) for a) normal incidence and b) an angle of incidence of 30°.

Once we have established the relevance of the tapered section of the nanowires for the optical behavior of the layer, we compare the simulations of the absorbance of a layer

of base-tapered nanowires and a layer of straight nanowires for normal incidence (Figure 8.14a) and for an angle of incidence of 30° (Figure 8.14b). The straight wires have a diameter of 90 nm and a length of 3 μm and the base-tapered nanowires have the same geometry as before, i.e., a straight top section with a length of 2 μm and a nanowire diameter of 90 nm and a tapered bottom section with a length of 1 μm. The bottom diameter of the base-tapered nanowires is 270 nm. For both angles and for wavelengths below 550 nm the absorbance in the layer of straight nanowires (red dashed curve) and the layer of base-tapered nanowires (black solid curve) is almost identical, indicating that the geometry of the nanowires does not have a significant influence in the absorbance at these wavelengths. This large absorbance at short wavelengths even for straight wires agrees with the near-field data of Figure 8.13, where we found that most of the light is absorbed in the straight top of the wires. For both angles and longer wavelengths the absorbance in the layer of base-tapered nanowires is strongly enhanced compared to the absorbance of the layer of straight nanowires. At these wavelengths, light is absorbed by the tapered part, due to the higher material filling fraction and the coupling of light to guided modes in the nanowire. The dips in the absorbance at an angle of incidence of 30° and at 780 nm are due to the Rayleigh anomaly.

8.5 Conclusions

We have demonstrated the growth of arrays of heterostructured InP nanowires. The gold catalyst particles are patterned by substrate conformal imprint lithography resulting in homogenous large-area arrays of nanowires. We have demonstrated enhanced broadband and omnidirectional absorbance in arrays of base-tapered InP nanowires grown by the vapor-liquid-solid mechanism on top of an InP substrate. Measurements of the total reflectance reveal that the optical absorbance in the structure is around 97 %. The strong optical absorption is described by finite-difference time-domain simulations. Different mechanisms are responsible for this absorption. First, the low effective refractive index of the nanowire layer allows for a nearly perfect coupling of the incident light into the layer. Second, the strong absorption in InP has a major role at short wavelengths, while for longer wavelengths the light is efficiently coupled to guided modes in the tapered part of the nanowires. The low reflectance and the high absorbance in arrays of InP nanowires render these structures as promising building block for next generation solar cells.

Appendix

To confirm the high reproducibility of the growth of the nanowires, we analyzed the InAsP heterostructure of sample XIX by transmission electron microscopy (TEM). Figure 8.15a shows a TEM image of a representative nanowire and Figure 8.15b shows a TEM image with a higher magnification showing the InAsP heterostructure in the InP wire. The distance of the heterostructure from the top of the nanowires is determined from three nanowires being 1.08 μm $\pm$ 0.2 μm. That the heterostructure is not positioned in the middle of the nanowire length indicates that either the growth rate of InP is influenced

by the presence of the InAsP heterostructure or that the growth rate decreases during growth when the distance between the gold catalyst and the substrate increases. Energy-dispersive X-ray spectroscopy (EDX) of the heterostructure along the growth direction of the nanowire gives a value of the arsenic concentration of 10 % in the heterostructure and the length of the heterostructure of 20 nm. The arsenic concentration and the length of the heterostructure is indeed very homogeneous at least for the three analyzed nanowires, indicating that the control of position of the gold catalyst allows for control of the growth. High resolution TEM images of the top section of the nanowires reveal that the crystal structure of the nanowires is wurtzite (Figs. 8.15d and e).
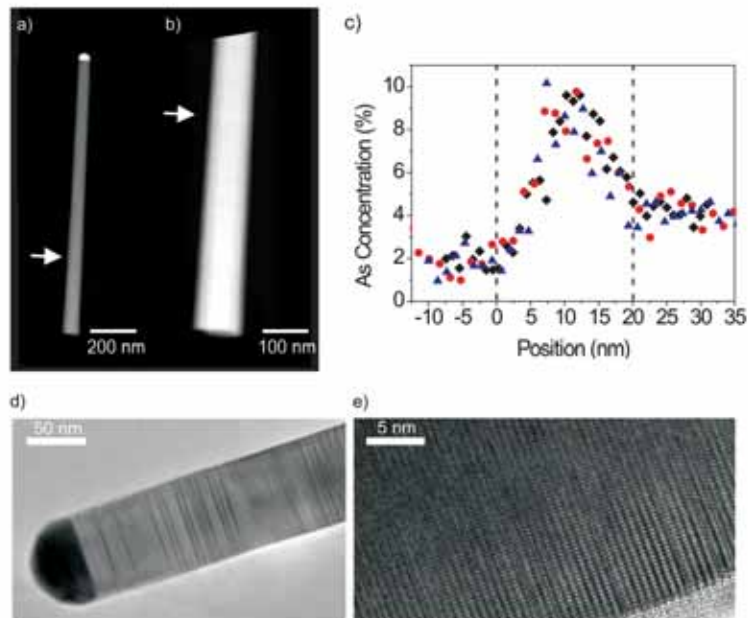

Figure 8.15: Transmission electron micrographs of a nanowire removed from sample XIX a) low resolution and b) zoom-in to the heterostructure. c) EDX linescans from three wires of the same sample along the heterostructure. d) low resolution and e) high resolution TEM images of the top part of the wire. In d) the gold particle that catalyzes the growth of the nanowire is visible. The high resolution TEM image in e) reveals the wurtzite crystal structure of the nanowires.

CHAPTER 9

APPLICATIONS AND OUTLOOK

The applications of semiconductor nanowires are numerous, depending on their morphology. In this chapter, we propose a gas and bio-sensor based on the reflection contrast of dense ensembles of nanowires and we compare its sensitivity to that of a surface plasmon resonance sensor. Further, we propose a graded refractive index antireflection layer based on tapered nanowires for enhancing light coupling into multi-junction solar cells. A novel design for a photovoltaic cell is proposed based on tapered nanowire arrays.

9.1   Introduction

Research on semiconductor nanowires has diverted into different possible applications. While single nanowires have been intensely studied with respect to electrical sensing of biomolecules [147], chemicals [148] and gases [149], ensembles of nanowires have been investigated in relation to LED's [41] and solar cells [17].

Within the FOM-Philips Industrial Partnership Program "Microphotonic Light Sources", we perform fundamental research on ensembles of nanowires and devise the potential use of these structures for optical sensing (Chapter 4) and as anti-reflective surfaces for high index semiconductors (Chapter 7). In Chapter 8 we describe that the optical absorption in arrays of InP nanowire is enhanced due to their geometry. In this chapter, we describe four concrete applications: i) optical gas sensing, ii) optical bio-sensing, iii) increased light coupling into III/V multi-junction solar cells, and iv) a novel nanowire based solar cell design.

i) Gas sensing, and especially NO_2 sensing, has received a lot of attention during the last years. The World Health Organization defines NO_2 as a toxic gas with significant health effects if the short term concentration exceeds 200 μg/m^3 or a long term concentration exceeds 40 μg/m^3 [150]. Developing sensitive NO_2 sensors will significantly help in monitoring the NO_2 concentration in air, and will facilitate taking precautions for increasing the air quality. We have investigated the possibility of using ensembles of nanowires as sensitive sensors of NO_2.

ii) For stimulating innovations that combine fundamental and applied research, AMOLF has organized an invention contest. Twenty-three groups consisting of four persons with different scientific background and from different groups at AMOLF participated in the contest. Our team[1] has investigated the possibility of using semiconductor nanowires as sensing platform of a point-of-care optical bio-sensor. Different diseases such as AIDS, hepatitis, or lung cancer can be detected by the presence of antibodies in the blood. Nowadays, pregnant women are screened standardly for the presence of different antibodies with a world-wide market of approximately 1 billion euros (20 million euros in the Netherlands) [151]. Improving detection systems of antibodies is thus of high relevance and nanowires can provide an appropriate platform for this detection. The invention resulted in a shared 1$^{\text{st}}$ prize of the contest obtained from jury members that evaluated both the scientific as well as economic relevance.

iii) Solar cells have received a lot of interest especially during the last few years as sustainable energy resource. Globally, the photovoltaic capacity has been increasing since the year 2000 at an annual average growth rate of more than 40 %. The Technology Roadmap envisions that by 2050, 11 % of the global electricity production will be provided by photovoltaics [152]. In 2009 the sales value of solar energy in Germany alone was 14000 million euro [153], with Germany being the world's biggest solar cell market. The solar cell market is split into different technologies with Si as standard absorber material. However, III/V solar cells form an emerging market for concentrator solar cells. Within a collaboration with the group of John Schermer from the Radboud University Nijmegen, we have investigated

---

[1]Our team was formed by Brian Gentry (Group Biological Softmatter), Arjan Gijsbertsen (Group XUV Physics), Iwert Mijnders (Group Photon Scattering) and the author of this thesis (Group Surface Photonics).

nanowire graded refractive index antireflection layers for III/V solar cells.

iv) Instead of using semiconductor nanowires as passive antireflection layers, as described before, we propose additionally a multi-junction solar cell design in which one of the active layers is formed by arrays of base-tapered nanowires.

In this chapter, we first explain sensing using the large and narrow peaks in reflection contrast of ensembles of vertically aligned nanowires. We compare the angular shift of the reflection contrast with different SiO_2 shell thicknesses to the shift in reflection of a surface plasmon resonance (SPR) sensor in Section 9.2. We find that the reflection contrast of the nanowire layer is more sensitive to thin layers of SiO_2 than surface plasmon resonances. This important conclusion confirms the potential use of semiconductor layers as very sensitive optical sensors. Further, we propose a NO_2 sensing platform based on nanowires. In Section 9.2.2 the point-of-care device for bio-sensing is introduced. In Section 9.3 the working principle of a III/V multi-junction solar cell is explained together with an improvement in efficiency due to a graded index layer. A novel nanowire solar cell design based on base-tapered nanowires is introduced in Section 9.4.

9.2 Sensing using the Reflection Contrast of Vertically aligned Nanowires

The shift of the reflection contrast of ensembles of vertically aligned GaP nanowires is investigated in Chapter 4 by measuring core-shell GaP-SiO_2 nanowire layers with different SiO_2 shell thicknesses. We found that the reflection contrast is very sensitive to small changes in the surrounding of the nanowires and that the peak of the reflection contrast shifts parabolically as a function of SiO_2 shell thickness. While we measured in Chapter 4 the reflection of different samples, we consider here an optical sensor, in which the light is impinging on a fixed position on the sample and the material to detect is flown onto the sample. Sensing using a small beam size results in large and narrow peaks of the reflection contrast (see Fig. 4.8 on page 62). Figure 9.1a shows calculations of the reflection contrast at λ = 532 nm for nanowires without and with SiO_2 shells with different thicknesses. The reference sample without a SiO_2 shell corresponds to the calculation fitting the measurement of Fig. 4.8a on page 62. With increasing shell thickness, the reflection contrast peak shifts to larger angles of incidence.

To demonstrate the high sensitivity of the reflection contrast to a material surrounding the nanowires, we compare the shift of the peak in the reflection contrast to a shift in the dip of a surface plasmon resonance (SPR) sensor [154]. Refractive index sensing using SPR's is a state-of-the-art sensing technique. Surface plasmon polaritons (SPPs) are evanescent electromagnetic waves confined in subwavelength scales at the interface between a dielectric and a metal and propagating along the interface. This strong confinement makes SPPs very sensitive to changes in the refractive index of the dielectric. Typically, SPP's are excited by total internal reflection of an incident plane wave at the interface between a prism and a metal layer as depicted in Figure 9.2. In this figure, gold is used as a metal and the dielectric is indicated by the thin layer of SiO_2. Figure 9.1b shows the calculation of attenuated total reflection of p-polarized light for different thicknesses

of the SiO$_2$ layer (see Fig. 9.2). The dip in the reflection is caused by the coupling of the incident beam to SPPs at the metal surface. Depending on the thickness of the SiO$_2$ layer, the resonance angle shifts to larger angles of incidence.
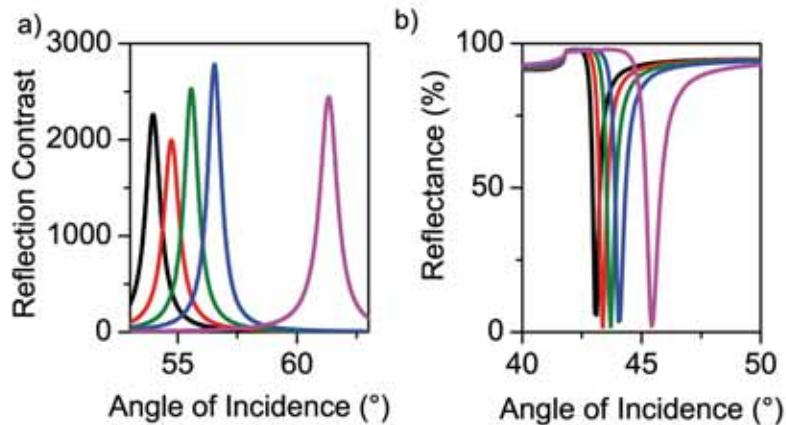

Figure 9.1: Calculated reflection contrast at λ = 532 nm of a layer of GaP nanowires (black curve) and nanowires covered with a SiO$_2$ shell of 5 nm (red curve), 10 nm (olive curve), 15 nm (blue curve), and 30 nm (magenta curve). The thickness of the nanowire layer is 1μm and the radius of the nanowires and the average distance is r_c = 19.65 nm and d_{nw} = 160 nm, respectively. b) Calculation of the attenuated total reflection at λ = 630 nm of a SPR sensor without and with a SiO$_2$ layer with the same thicknesses as in a).

Figure 9.2: Surface plasmon polariton at the interface between gold and SiO$_2$ excited using total internal reflection on a prism-gold interface.

The shift of the surface plasmon resonance is plotted together with the shift of the peak of the reflection contrast in Figure 9.3. We have also included in this figure the experimental data obtained from Figure 4.10. The shift of the SPR, as well as the measured reflection contrast peak shift using a large beam on the sample and the calculated peak shift follow a parabolic dependence. Both measurements and calculations of the reflection contrast

show a larger peak shift than the SPR. While a layer of SiO_2 with a thickness of 30 nm shifts the surface plasmon resonance by 2.4 °, the measurement of the reflection contrast shows a shift of 6.9 °. Theoretically, a shift of 7.4° is expected. Therefore, we can conclude that layers of semiconductor nanowires are more sensitive to changes in the refractive index in thin layers around the nanowires than SPPs to changes in the refractive index in similar layers on top of metals. The higher sensitivity of the reflection contrast can be attributed to the large surface to volume ratio of nanowires that allows probing small changes in their surrounding. Semiconductor nanowire layers are very promising materials for bio-sensing applications, considering that the shell thicknesses and the refractive index of the investigated SiO_2 layers are comparable to that of layers of proteins or DNA.
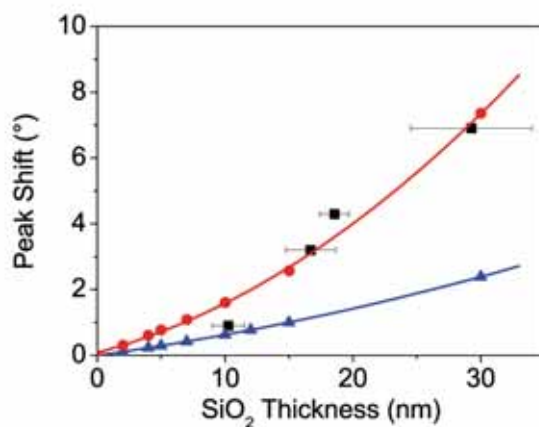
Figure 9.3: Measured peak shift of the reflection contrast as a function of the SiO_2 thickness (black squares), calculated peak shift of the reflection contrast for optimized polarization (red circles) and peak shift of a SPR sensor (blue triangles). The solid lines are fits to the data.

9.2.1 NO$_2$ Sensing using Vertically Aligned Nanowires

In the previous section, we have described the high sensitivity of the reflection contrast to a medium surrounding the nanowires by measuring and modeling core-shell GaP-SiO_2 nanowires with different shell thickness. Here, we use the high sensitivity of the reflection contrast for detection of NO_2 gas. This detection is done by means of porphyrines. When the porphyrines are exposed to NO_2, an electronic transition is activated that gives rise to a characteristic absorption band around 700 nm and to changes of the complex refractive index of the porphyrins. For calculating the sensitivity of a NO_2 sensor, we consider the volume surrounding the GaP nanowires completely infiltrated with porphyrins that are embedded in a nanoporous silica matrix with a porosity of 30 %. A detailed description of

the porphyrines, the nanoporous silica matrix, and the change in refractive index due to exposure can be found in Ref. [155]. The refractive index of the porphyrines embedded in a SiO_2 matrix can be modeled using a Lorentz-oscillator model. Further details of the model can be found in Ref. [155]. The refractive indices determined by the Lorentz-oscillator model are given in Figure 9.4 for a NO_2 concentration of 0.5 ppm (dashed curve) and 1.3 ppm (dashed-dotted curve). For comparison also the refractive index of non-exposed porphyrines in a SiO_2 matrix are given (solid line).
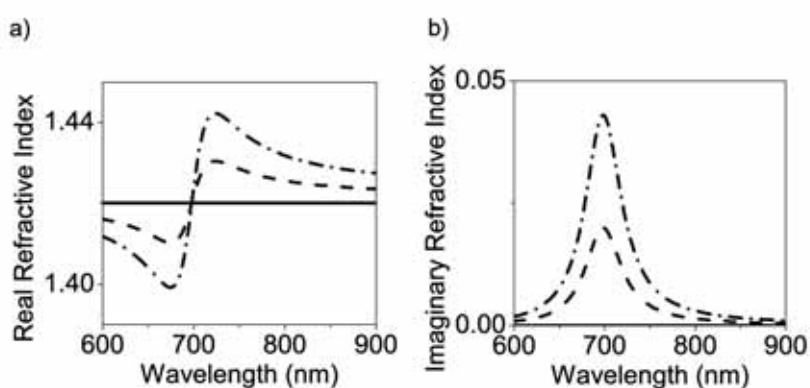
Figure 9.4: a) Real and b) imaginary part of the refractive index for porphyrines embedded in a nanoporous matrix before (black line) and after exposure to 0.5 ppm (dashed curve) and 1.3 ppm (dashed-dotted curve) NO_2.

Figure 9.5a shows a calculation of nanowires embedded in porphyrins in a nanoporous silica matrix without exposure to NO_2 (black curve) and exposed to NO_2 with a concentration of 0.5 ppm (dashed curve) and 1.3 ppm (dashed-dotted curve). While the reflection contrast peak located at around 730 nm is shifted by 13 nm when exposed to NO_2 with a concentration of 1.3 ppm, the contrast at 730 nm decreases by 3 orders of magnitude. An exposure to NO_2 with a concentration of 0.5 ppm results in a amplitude decrease of 2 orders of magnitude, that is easily detectable. For comparison, Figure 9.5b shows a calculation of the reflection of a 1.5 μm thick layer of porphyrines on top of a gold surface at an angle of incidence of 60°. While the reflection contrast decreases by 3 orders of magnitude, the reflection only decreases by 2 orders of magnitude when exposed to 1.3 ppm of NO_2. This strong decrease of the reflection contrast allows for a sensitive detection of low concentrations of NO_2 at a single wavelength.

Sensing NO_2 for health issues requires a much lower detection limit than 0.5 ppm. If we focus on sensing the toxic concentrations defined by the World Health Organization, we need to estimate the sensitivity for NO_2 concentrations of 0.1 ppm (200 μg/m^3) for short term exposure and 0.02 ppm (40 μg/m^3) for long term exposure. From the three calculated reflection contrast curves (Fig. 9.5), we can extrapolate that the dip in reflection contrast at 700 nm increases parabolically and the peak at 730 nm decreases parabolically
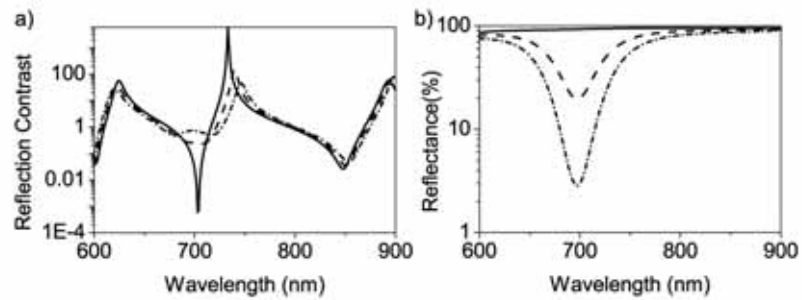
Figure 9.5: a) Calculated reflection contrast as a function of wavelength of a layer of GaP nanowires with a length of 1.5 μm, a GaP filling fraction of 15 %, and an angle of incidence of 60° for no exposure to NO_2 (solid curve), 0.5 ppm NO_2 (dashed curve), and 1.3 ppm (dashed-dotted curve). b) Calculated p-polarized reflection of a 1.5 μm thick layer of porphyrines on top of gold for the same NO_2 concentrations as in a) and an angle of incidence of 60°.
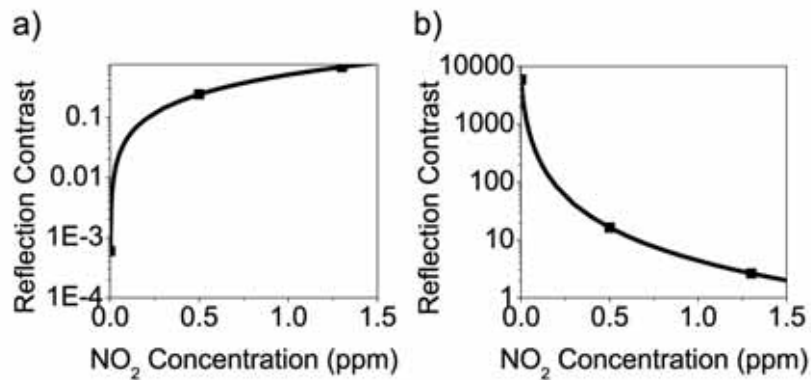

Figure 9.6: Calculated reflection contrast as a function of NO_2 concentration for of a layer of GaP nanowires with a length of 1.5 μm, a GaP filling fraction of 15 %, and an angle of incidence of 60° at a wavelength of a) 700 nm and b) 730 nm. The symbols correspond to the calculated reflection contrast of Fig. 9.5, the curves are parabolic fits.

as a function of NO_2 concentration (Figs. 9.6a and b). Based on Ref. [156], we can assume that the refractive index of the porphyrine layer linearly changes with NO_2 concentration. Therefore, if the layer is exposed to 0.1 ppm, the reflection contrast at the wavelength of the dip increases by a factor of 75. An exposure to 0.02 ppm results in a increase of one order of magnitude. When sensing at the peak position, the two concentrations decrease the contrast by a factor of 22 and 3.5, respectively. In both cases, i.e., sensing at the dip or peak position, the nanowire layer shows a high sensitivity to the critical values of NO_2 concentration in air. Such an optical sensor could be cost-effectively realized using a laser diode or a LED emitting at a single wavelength or with a very narrow emission spectrum and a Si photodetector.

9.2.2 Point-of-care Nanowire Sensor

During the AMOLF Invention Contest, we proposed a point-of-care optical biosensor device based on nanowires. This device should be a handheld device, allowing to be used by nurses or doctors in areas with a low density of hospitals such as parts of Canada, Russia, Australia or third-world countries. Additionally, the device could be used in densely populated areas to save costs for advanced labs.

The nanowire sensing platform is based on reflection contrast sensing as described in Chapter 4 and Section 9.2.1. A calculation of the angle dependent reflection contrast performed on nanowires that are coated with antigens with a thickness of 10 nm and surrounded by water as buffer layer shows a peak at an angle of incidence of 54.1°(Fig. 9.7). The calculation is performed using a wavelength of 640 nm, which is the wavelength of standard lasers in DVD and CD players. If blood or urine is flown through the nanowires, and if the blood contains antibodies of a certain disease that corresponds to the antigens coating the nanowires, the antibodies will stick to the antigens and therefore increase the thickness of the shell around the nanowires. In a next step, the blood is washed away, leaving the coated nanowires surrounded by water. The calculation of the reflection contrast of nanowires coated with antigens and antibodies, assuming an antibody layer thickness of 10 nm corresponding to the antibodies IgG, show that the amplitude at an angle of 54.1° is reduced by three orders of magnitude. The peak in reflection contrast shifts by 6°.

For the point-of-care devices, standard CD or DVD optics can be used together with a microfluidic system. Based on this, the cost per point-of-care device will be around € 300 to € 500. The nanowire chip, that in an ideal situation will be reusable by removing the antibodies with a pH solution, will cost around € 30 - € 50, depending on the material and the fabrication steps. Therefore, it is possible to develop a handheld optical biosensor for much less than € 1000.

9.3 Tapered Nanowires as Antireflection Surfaces for Multi-junction Solar Cells

Instead of determining the light coupling efficiency into Si solar cells, as we did in Chapter 7 on page 98, we focus here on a graded refractive index layer based on GaP nanowires
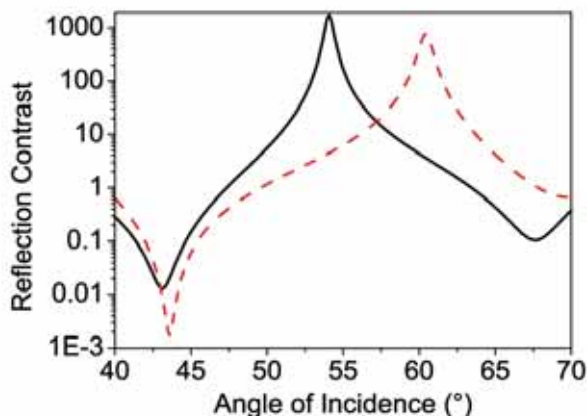
Figure 9.7: Calculated reflection contrast as a function of angle of incidence of a layer of nanowires with a length of 1.5 μm, a GaP filling fraction of 9 %, and a wavelength of 640 nm for nanowires coated with the antigen embedded in a buffer (black curve) and coated with antibodies with a thickness of 10 nm sticking to the antigens embedded in a buffer with a refractive index of 1.33.

for III/V solar cells. While Si solar cells are the world wide most fabricated and installed solar cells [152], they only capture a narrow spectral range. For this narrow spectral range, the standard Si_3N_4 antireflection layers are sufficient and are not only used for reducing the reflection, but additionally used as surface passivation layers. [157]

The market segment of III/V compound semiconductors is much smaller, as the fabrication of III/V materials is more expensive. However, III/V solar cells have found their niche for space solar cells and in concentrator systems. While the fabrication is more expensive for III/V than for Si solar cells, the efficiency of III/V solar cells exceeds that of Si. Heteroepitaxy allows for growing different III/V semiconductors with different electronic bandgaps upon each other, as long as their crystal lattice dimensions are matching. While double-junction and triple-junction solar cells have been already demonstrated [158], research focusses now on the fabrication of quadruple solar cells. A schematic of a possible quadruple solar cell is given in Figure 9.8a. In this example, the solar cell consists of four different subcells, where the subcell with the highest electronic bandgap energy forms the top subcell, for example, InGaP. By adjusting the In content of the subcell, the bandgap energy can be optimized for best performance. Below the top subcell, a GaAs subcell, an InGaAsP subcell and an InGaAs subcell are fabricated, each absorbing the light of a spectral energy lower than the one above. For the last two subcells, the material composition can be chosen for best performance, as long as the lattice mismatch does not exceed a certain critical value for the epitaxial growth. The top-most layer of the solar cell is AlInP for electrical contact. To show the wide spectral range that can be covered

133

with multi-junction solar cells, Figure 9.8b shows the solar radiance standard AM1.5G, including the absorption bands of a quadruple-junction solar cell. From Figure 9.8b, it is obvious that multi-junction solar cells capture a broad spectral range that requires a broadband antireflection layer.
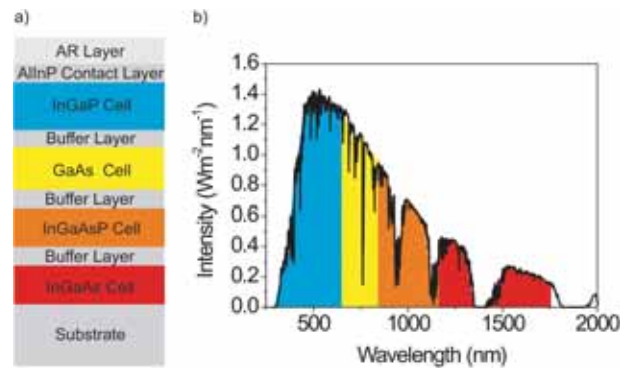

Figure 9.8: a) Schematic of a quadruple solar cell and b) Solar spectrum AM1.5G and absorption band of the individual junctions of the quadruple solar cell.

Additionally, as III/V multi-junction cells are mainly used in concentrator systems, in which the light is focused onto the cell, an antireflection coating that reduces the reflection for angles up to 30° is required.

A standard antireflection coating for single junction GaAs III/V solar cells is a ZnS/MgF_2 double layer with a thickness of 40 nm and 99 nm, respectively. The reflection is reduced due to destructive interference of light reflected at the interfaces. However, as we have shown in Chapter 7, a graded refractive index layer is advantageous over interference coatings with respect to bandwidth and omni-directionality.

To verify the increase in efficiency of a multi-junction solar cell coated with nanowires, we have performed calculations of a quadruple solar cell with the individual layers chosen as described in Figure 9.8a. The calculations take into account the reflection from, transmission into, and absorption in each layer of the solar cell by using the transfer-matrix method. From the reflection from and transmission into each layer, the photocurrent is calculated by assuming an internal quantum efficiency of 100 %, meaning that every photon absorbed in one of the layers contributes to the photocurrent of the cell. We have calculated the external efficiency of the solar cell from the calculations of the reflection, transmission and absorption for normal incidence using the standard spectrum at the earth's surface (AM1.5G, 1000Wm^{-2}, see Fig. 9.8b), and compared the external efficiency of a solar cell coated with a graded index layer and with a standard ZnS/MgS_2 double-layer antireflection coating. The quality of a solar cell is defined by its fill factor, i.e., the ratio between the maximum power of a solar cell and the product of open-circuit voltage and short-circuit current. The fill factor of the simulated quadruple solar cell is estimated to be 87 %. For a graded refractive index layer with a thickness of 1 μm and a

parabolically increasing refractive index from 1 to 3.3, matching the optical impedance at the air-nanowire layer and nanowire layer-AlInP interface, an external efficiency of 33.9 % is calculated. For comparison, a standard ZnS/MgS_2 double layer antireflection coating [159] allows for a theoretical efficiency of 33.2%. The graded index layer increases the relative efficiency of a solar cell by 2.1 %.

The top most layer of a multi-junction solar cell is AlInP. However, the growth of nanowires on AlInP has not been reported before. Additionally, instead of the graded index layer presented in Chapter 7, that is grown on (111) substrates, III/V solar cells are usually fabricated on (100) substrates. To verify that the growth of GaP nanowires on an $Al_xIn_{1-x}P$ (x = 0.5) layer that is lattice matched to GaAs is possible, we have performed a first growth run of GaP nanowires on a 30 nm thick AlInP layer on top of a GaAs substrate. For the first test, gold colloids with a diameter of 10 nm are spin-coated on the substrate to catalyze the growth of the nanowires. Figure 9.9a shows GaP nanowires grown for 3 min at a temperature of 570 °C (sample XXII in Table 2.1, page 29). As described in Chapter 2, the growth on (100) substrates does not lead to vertical nanowires, but on nanowires that grow with certain angles with respect to the substrate. Therefore, the nanowires shown in the SEM image in Figure 9.9a grow in different directions. However, as long as the nanowires have a diameter and a length in the subwavelength range, their orientation has no effect on a graded refractive index. What is more important is the tapering of the nanowires that results in a larger GaP filling fraction at the bottom than at the top of the layer.
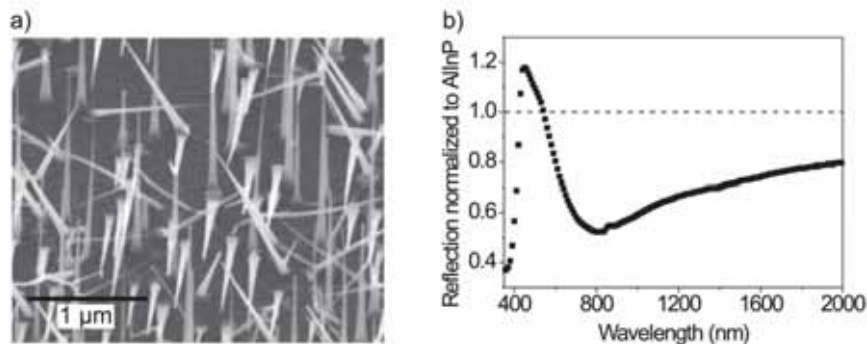

Figure 9.9: a) Scanning electron micrograph of GaP nanowires grown on AlInP that is lattice matched to GaAs. b) Total reflection from sample normalized to the total reflection of an AlInP layer grown on GaAs.

A first measurement of the total reflectance using the angle-integrated setup described in Chapter 7 on page 104 is shown in Figure 9.9b normalized to the total reflectance of an AlInP layer on top of a GaAs substrate. A reduction of the total reflectance is realized over a broad range of wavelengths, indicating that more light is coupled into the AlInP and GaAs layers, when these are covered by tapered GaP nanowires.

For a better performance of the graded index layer, the nanowires can be grown using a thin gold film for catalyzing the growth. Alternatively, the gold catalyst can be predefined by SCIL (see Chapter 2) for optimum surface coverage.

9.4   Novel Design of a Nanowire based Solar Cell

In Chapter 8 we state that the absorption in layers of base-tapered nanowires is enhanced due to their geometry. From analyzing the electric near field along the nanowires, we have determined that the strong optical absorption in the base-tapered nanowire layer is due to several effects, depending on the wavelength. The low effective refractive index at the top has a high impact on the amount of light coupled into the nanowire layer. Due to this low refractive index, light can be coupled efficiently into the layer. Further, the high absorption coefficient of InP at short wavelength results in strong absorption of light in the straight top segment of the nanowires. For longer wavelength, light is coupled to guided modes in the tapered base, where it gets absorbed for wavelength smaller than that of the electronic bandgap energy of InP (λ = 920 nm). For wavelengths longer than that of the electronic bandgap energy of InP, the light is efficiently coupled into the underlying substrate by the guided modes. Based on these findings, we propose the following design for an efficient nanowire solar cell (Fig. 9.10). Base-tapered InP nanowires have been doped forming a radial pn-junction. Radially doped base-tapered nanowires can be used for an efficient photo-current conversion of light in the wavelength range between 400 nm and 920 nm. The nanowires are heteroepitaxially grown on top of a solar cell formed by a medium with the electronic bandgap at a wavelength around 1100 nm or longer, e.g., InGaAsP, Si, or Ge. For these wavelengths the light will be guided into the underlying layer with extremely high efficiency where it gets absorbed and converted to current.
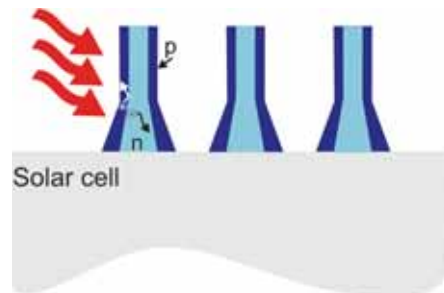

Figure 9.10: Proposed design of a new base-tapered nanowire solar cell. Radially doped base-tapered InP nanowires are grown heteroepitaxially on top of a solar cell with an electronic bandgap smaller than that of InP.

9.5 Conclusion

We have discussed in this chapter four possible applications of ensembles of nanowires. First, we have described that nanowires can be used as a very sensitive sensing platform. A comparison with a surface plasmon resonance sensor shows that the reflection contrast is more sensitive to changes in the surrounding of the nanowires than a surface plasmon resonance sensor to thin films. Second, we have shown that ensembles of nanowires are a promising sensing platform for NO_2 gas sensing and in a point-of-care device for bio-sensing. While NO_2 sensing is important to secure the air quality, a handheld bio-sensor based on nanowires can reduce the costs of medical testing. The third application refers to tapered nanowires grown on III/V multi-junction solar cells to increase their efficiency. The fourth application describes a novel solar cell design based on tapered nanowires.

REFERENCES

[1] J. B. Hannon, S. Kodambaka, F. M. Ross, and R. M. Tromp, *The influence of the surface migration of gold on the growth of silicon nanowires*, Nature **440**, 69 (2006).

[2] X. Duan, Y. Huang, Y. Cui, J. Wang, and C. M. Lieber, *Indium phosphide nanowires as building blocks for nanoscale electronic and optoelectronic devices*, Nature **409**, 66 (2001).

[3] S. J. An and G.-C. Yi, *Near ultraviolet light emitting diode composed of n-GaN/ZnO coaxial nanorod heterostructures on a p-GaN layer*, Appl. Phys. Lett. **91**, 123109 (2007).

[4] N. Sköld, L. S. Karlsson, M. W. Larsson, M.-E. Pistol, W. Seifert, J. Trägårdh, and L. Samuelson, *Growth and optical properties of strained GaAs-GaIn$_{1-x}$P$_x$ core-shell nanowires*, Nano Lett. **5**, 1943 (2005).

[5] M. T. Björk, B. J. Ohlsson, T. Sass, A. I. Persson, C. Thelander, M. H. Magnusson, K. Deppert, L. R. Wallenberg, and L. Samuelson, *One-dimensional steeplechase for electrons realized*, Nano Lett. **2**, 87 (2002).

[6] M. H. Huang, S. Mao, H. Feick, H. Yan, Y. Wu, H. Kind, E. Weber, R. Russo, and P. Yang, *Room-temperature ultraviolet nanowire nanolasers*, Science **292**, 1897 (2001).

[7] X. Duan, Y. Huang, R. Agarwal, and C. M. Lieber, *Single-nanowire electrically driven lasers*, Nature **421**, 241 (2003).

[8] M. Yazawa, M. Koguchi, and K. Hiruma, *Heteroepitaxial ultrafine wire-like growth of InAs on GaAs substrates*, Appl. Phys. Lett. **58**, 1080 (1991).

[9] T. Mårtensson, C. P. T. Svensson, B. A. Wacaser, M. W. Larsson, W. Seifert, K. Deppert, A. Gustafsson, L. R. Wallenberg, and L. Samuelson, *Epitaxial III/V nanowires on silicon*, Nano Lett. **4**, 1987 (2004).

[10] E. P. A. M. Bakkers, J. A. van Dam, S. D. Franceschi, L. P. Kouwenhoven, M. Kaiser, M. Verheijen, H. Wondergem, and P. van der Sluis, *Epitaxial growth of InP nanowires on germanium*, Nature Mat. **3**, 769 (2004).

[11] M. S. Gudiksen, L. J. Lauhon, J. Wang, D. C. Smith, and C. M. Lieber, *Growth of nanowire superlattice structures for nanoscale photonics and electronics*, Nature **425**, 617 (2002).

[12] D. Li, Y. Wu, R. Fan, P. Yang, and A. Majumdar, *Thermal conductivity of Si/SiGe superlattice nanowires*, Appl. Phys. Lett. **83**, 3186 (2003).

[13] M. T. Borgström, V. Zwiller, E. Müller, and A. Imamoglu, *Optically bright quantum dots in single nanowires*, Nano Lett. **5**, 1439 (2005).

[14] J. C. Johnson, H.-J. Choi, K. P. Knutsen, R. D. Schaller, P. Yang, and R. J. Saykally, *Single gallium nitride nanowire lasers*, Nature Mat. **1**, 106 (2002).

[15] J. Wang, M. S. Gudiksen, X. Duan, Y. Cui, and C. M. Lieber, *Highly polarized photoluminescence and photodetection from single indium phosphide nanowires*, Science **293**, 1455 (2001).

[16] S. L. Diedenhofen, G. Vecchi, R. E. Algra, A. Hartsuiker, O. L. Muskens, G. Immink, E. P. A. M. Bakkers, W. L. Vos, and J. Gómez Rivas, *Broad-band and omnidirectional antireflection coatings based on semiconductor nanorods*, Adv. Mat. **21**, 973 (2009).

[17] A. P. Goodey, S. M. Eichfeld, K.-K. Lew, J. M. Redwing, and T. E. Mallouk, *Silicon nanowire array photoelectrochemical cells*, JACS **129**, 12344 (2007).

[18] O. L. Muskens, M. T. Borgström, E. P. A. M. Bakkers, and J. Gómez Rivas, *Giant optical birefringence in ensembles of semiconductor nanowires.*, Appl. Phys. Lett. **89**, 233117 (2006).

[19] Y. Huang, X. Duan, Y. Cui, L. J. Lauhon, K.-H. Kim, and C. M. Lieber, *Logic gates and computation from assembled nanowire building blocks*, Science **294**, 1313 (2001).

[20] M. T. Björk, B. J. Ohlsson, C. Thelander, A. I. Persson, K. Deppert, L. R. Wallenberg, and L. Samuelson, *Nanowire resonant tunneling diodes*, Appl. Phys. Lett. **81**, 4458 (2002).

[21] E. D. Minot, F. Kelkensberg, M. van Kouwen, J. A. van Dam, L. P. Kouwenhoven, V. Zwiller, M. T. Borgström, O. Wunnicke, M. A. Verheijen, and E. P. A. M. Bakkers, *Single quantum dot nanowire LEDs*, Nano Lett. **7**, 367 (2007).

[22] Y.-J. Lee, D. S. Ruby, D. W. Peters, B. B. McKenzie, and J. W. P. Hsu, *ZnO nanostructures as efficient antireflection layers in solar cells*, Nano Lett. **8**, 1501 (2008).

[23] L. Tsakalakos, J. Balch, J. Fronheiser, B. A. Korevaar, O. Sulima, and J. Rand, *Silicon nanowire solar cells*, Appl. Phys. Lett. **91**, 233117 (2007).

[24] C. F. Bohren and D. R. Huffman, *Absorption and scattering of light by small particles*, Wiley, New York, 1983.

[25] A. Kirchner, K. Busch, and C. M. Soukoulis, *Transport properties in random arrays of cylinders*, Phys. Rev. B **57**, 277 (1998).

[26] R. S. Wagner and W. C. Ellis, *Vapor-liquid-solid mechanism of single crystal growth*, Appl. Phys. Lett. **4**, 89 (1964).

[27] E. I. Givargizov, *Fundamental aspects of VLS growth*, J. Crystal Growth **31**, 20 (1975).

[28] X. Duan and C. M. Lieber, *General sythesis of compound semiconductor nanowires*, Adv. Mat. **12**, 298 (2000).

[29] R. E. Algra, M. A. Verheijen, M. T. Borgström, L.-F. Feiner, G. Immink, W. J. P. van Enckevort, and E. P. A. M. Bakkers, *Twinning superlattices in indium phosphide nanowires*, Nature **456**, 369 (2008).

[30] J. Johansson, L. S. Karlsson, C. P. T. Svensson, T. Mårtensson, B. A. Wacaser, K. Deppert, L. Samuelson, and W. Seifert, *Structural properties of <111>B-oriented III-V nanowires*, Nature Mat. **5**, 574 (2006).

[31] M. T. Borgström, G. Immink, B. Ketelaars, R. Algra, and E. P. A. M. Bakkers, *Synergetic nanowire growth*, Nature Nanotech. **2**, 541 (2007).

[32] K. Hiruma, M. Yazawa, T. Katsuyama, K. Ogawa, K. Haraguchi, M. Koguchi, and H. Kakibayashi, *Growth and optical properties of nanometer-scale GaAs and InAs whiskers*, Appl. Phys. Rev. **77**, 447 (1995).

[33] F. Glas, J.-C. Harmand, and G. Patriarche, *Why does wurtzite form in nanowires of III-V zinc blende semiconductors?*, Phys. Rev. Lett. **99**, 146101 (2007).

[34] X. Duan and C. M. Lieber, *Laser-assisted catalytic growth of single crystal GaN nanowires*, JACS **122**, 188 (2000).

[35] A. Cavallini, L. Polenta, M. Rossi, T. Richter, M. Marso, R. Meijers, R. Calarco, and H. Lüth, *Defect distribution along single GaN nanowhiskers*, Nano Lett. **6**, 1548 (2006).

[36] L. K. van Vugt, S. Rühle, and D. Vanmaekelbergh, *Phase-correlated nondirectional laser emission from the end facets of a ZnO nanowire*, Nano Lett. **6**, 2707 (2006).

[37] M. A. Verheijen, G. Immink, T. de Smet, M. T. Borgström, and E. P. A. M. Bakkers, *Growth kinetics of heterostructured GaP-GaAs nanowires*, JACS **128**, 1353 (2006).

[38] L. J. Lauhon, M. S. Gudiksen, D. Wang, and C. M. Lieber, *Epitaxial core-shell and core-multishell nanowire heterostructures*, Nature **420**, 57 (2002).

[39] M. A. Verheijen, R. E. Algra, M. T. Borgström, G. Immink, E. Soutry, W. J. P. van Enckevort, E. Vlieg, and E. P. A. M. Bakkers, *Three-dimensional morphology of GaP-GaAs nanowires revealed by transmission electron microscopy tomography*, Nano Lett. **7**, 3051 (2007).

[40] B. Tian, X. Zheng, T. J. Kempa, Y. Fang, N. Yu, G. Yu, J. Huang, and C. M. Lieber, *Coaxial silicon nanowires as solar cells and nanoelectronic power sources*, Nature **449**, 885 (2007).

[41] K. Haraguchi, T. Katsuyama, K. Hiruma, and K. Ogawa, *GaAs p-n junction formed in quantum wire crystals*, Appl. Phys. Lett. **60**, 745 (1992).

[42] A. M. Morales and C. M. Lieber, *A laser ablation method for the synthesis of crystalline semiconductor nanowires*, Science **279**, 208 (1998).

[43] S. N. Mohammad, *Self-catalytic solution for single-crystal nanowire and nanotube growth*, The Journal of Chemical Physics **127**, 244702 (2007).

[44] M. J. Bierman, Y. K. A. Lau, A. V. Kvit, A. L. Schmitt, and S. Jin, *Dislocation-driven nanowire growth and Eshelby twist*, Science **320**, 1060 (2008).

[45] J. Zhu, H. Peng, A. F. Marshall, D. M. Barnett, W. D. Nix, and Y. Cui, *Formation of chiral branched nanowires by the Eshelby Twist*, Nature Nanotech. **3**, 477 (2008).

[46] W. S. Shi, Y. F. Zheng, N. Wang, C. S. Lee, and S. T. Lee, *Oxide-assisted growth and optical characterization of gallium-arsenide nanowires*, Appl. Phys. Lett. **78**, 3304 (2001).

[47] R.-Q. Zhang, Y. Lifshitz, and S.-T. Lee, *Oxide-assisted growth of semiconducting nanowires*, Adv. Mat. **15**, 635 (2003).

[48] K. Ikejiri, J. Noborisaka, S. Hara, J. Motohisa, and T. Fukui, *Mechanism of catalyst-free growth of GaAs nanowires by selective area MOVPE*, J. Crystal Growth **298**, 616 (2007), Thirteenth International Conference on Metal Organic Vapor Phase Epitaxy (ICMOVPE XIII).

[49] R. K. Debnath, R. Meijers, T. Richter, T. Stoica, R. Calarco, and H. Lüth, *Mechanism of molecular beam epitaxy growth of GaN nanowires on Si(111)*, Appl. Phys. Lett. **90**, 123117 (2007).

[50] A. I. Hochbaum, R. Fan, R. He, and P. Yang, *Controlled growth of Si nanowire arrays for device integration*, Nano Lett. **5**, 457 (2005).

[51] I. Doron-Mor, Z. Barkay, N. Filip-Granit, A.Vaskevich, and I. Rubinstein, *Ultrathin gold island films on silanized glass. Morphology and optical properties*, Chem. Mater. **16**, 3476 (2004).

[52] P. Mohan, J. Motohisa, and T. Fukui, *Controlled growth of highly uniform, axial/radial direction-defined, individually addressable InP nanowire arrays.*, Nanotechnology **16**, 2903 (2005).

[53] L. E. Jensen, M. T. Björk, S. Jeppesen, A. I. Persson, B. J. Ohlsson, and L. Samuelson, *Role of surface diffusion in chemical beam epitaxy of InAs nanowires*, Nano Lett. **4**, 1961 (2004).

[54] H. J. Fan, W. Lee, R. Scholz, A. Dadgar, A. Krost, K. Nielsch, and M. Zacharias, *Arrays of vertically aligned and hexagonally arranged ZnO nanowires: a new template-directed approach*, Nanotechnology **16**, 913 (2005).

[55] H. J. Fan, B. Fuhrmann, R. Scholz, F. Syrowatka, A. Dadgar, A. Krost, and M. Zacharias, *Well-ordered ZnO nanowire arrays on GaN substrate fabricated via nanosphere lithography.*, J. Cryst.Growth **287**, 34 (2006).

[56] T. Mårtensson, P. Carlberg, M. Borgström, L. Montelius, W. Seifert, and L. Samuelson, *Nanowire arrays defined by nanoimprint lithography*, Nano Lett. **4**, 699 (2004).

[57] M. Verschuuren and S. Wuister, *Imprint lithography*, US 2008/0011934 (2008).

[58] T. Odom, J. Love, D. Wolfe, K. Paul, , and G. Whitesides, *Improved pattern transfer in soft lithography using composite stamps*, Langmuir **18**, 5314 (2002).

[59] M. Verschuuren and H. van Sprang, *3D photonic structures by sol-gel imprint lithography*, Mater. Res. Soc. Symp. Proc. **1002**, 1002 (2005).

[60] B. A. Wacaser, K. A. Dick, J. Johansson, M. T. Borgström, K. Deppert, and L. Samuelson, *Preferential interface nucleation: An expansion of the VLS growth mechanism for nanowires*, Adv. Mat. **21**, 153 (2009).

[61] W. Braun, V. M. Kaganer, A. Trampert, H.-P. Schönherr, Q. Gong, R. Nötzel, L. Däweritz, and K. H. Ploog, *Diffusion and incorporation: shape evolution during overgrowth on structured substrates*, Journal of Crystal Growth **227-228**, 51 (2001).

[62] A. Kwan, J. Dudley, and E. Lantz, *Who really discovered Snell's law?*, Physics World **15**, 64 (2002).

[63] M. Born and E. Wolf, *Principles of optics*, Cambridge University Press, 6th edition, 1997.

[64] D. Kovalev, G. Polisski, J. Diener, H. Heckler, N. Künzner, V. Y. Timoshenko, and F. Koch, *Strong in-plane birefringence of spatially nanostructured silicon*, Appl. Phys. Lett. **78**, 916 (2001).

[65] N. Künzner, D. Kovalev, J. Diener, E. Gross, V. Y. Timoshenko, G. Polisski, and F. Koch, *Giant birefringence in anisotropically nanostructured silicon*, Opt. Lett. **26**, 1265 (2001).

[66] C. J. Oton, Z. Gaburro, M. Ghulinyan, L. Pancheri, P. Bettoti, L. D. Negro, and L. Pavesi, *Scattering rings in optically anisotropic porous silicon*, Appl. Phys. Lett. **81**, 4919 (2002).

[67] V. Y. Timoshenko, L. A. Osminkina, A. I. Efimova, L. A. Golovan, P. K. Kashkarov, D. Kovalev, N. Künzner, E. Gross, J. Diener, and F. Koch, *Anisotropy of optical absorption in birefringent porous silicon*, Physical Review B **67**, 113405 (2003).

[68] B.-H. O, C.-H. Choi, S.-B. Jo, M.-W. Lee, D.-G. Park, B.-G. Kang, S.-H. Kim, R. Liu, Y. Y. Li, M. J. Sailor, and Y. Fainman, *Novel form birefringence modeling for an ultracompact sensor in porous silicon films using polarization interferometry*, IEEE Photonics Technology Letters **16**, 1546 (2004).

[69] N. Künzner, J. Diener, E. Gross, D. Kovalev, V. Y. Timoshenko, and M. Fujii, *Form birefringence of anisotropically nanostructured silicon*, Phys. Rev. B **71**, 195304 (2005).

[70] L. A. Golovan, P. K. Kashkarov, and V. Y. Timoshenko, *Form birefringence in porous semiconductors and dielectrics: A review*, Crystallography Reports **52**, 672 (2007).

[71] M. L. Markham, J. J. Baumberg, D. C. Smith, X. Li, T. Gabriel, G. S. Attard, and I. Nandhakumar, *Birefringent cadmium-telluride-based metamaterial*, Appl. Phys. Lett. **86**, 011912 (2005).

[72] I. M. Tiginyanu, I. V. Kravetsky, S. Langa, G. Marowsky, J. Monecke, and H. Föll, *Porous III-V compounds as nonlinear optical materials*, phys. stat. sol. (a) **197**, 549 (2003).

[73] F. Genereux, S. W. Leonard, H. M. van Driel, A. Birner, and U. Gösele, *Large birefringence in two-dimensional silicon photonic crystals*, Phys. Rev. B **63**, 161101(R) (2001).

[74] W. A. de Heer, W. S. Bacsa, A. Châtelain, T. Gerfin, R. Humphrey-Baker, L. Forro, and D. Ugarte, *Aligned carbon nanotube films: Production and optical and electronic properties*, Science **268**, 845 (1995).

[75] F. J. Garcia-Vidal, J. M. Pitarke, and J. B. Pendry, *Effective medium theory of the optical properties of aligned carbon nanotubes*, Phys. Rev. Lett. **78**, 4289 (1997).

[76] W. Lü, J. Dong, and Z.-Y. Li, *Optical properties of aligned carbon nanotube systems studied by the effective-medium approximation method*, Phys. Rev. B **63**, 033401 (2000).

[77] J. C. Maxwell-Garnett, *Colours in metal glasses and in metallic films*, Phil. Trans. R. Soc. Lond. A **203**, 385 (1904).

[78] E. Hecht, *Optics*, Addison Wesley, 4th edition, 2002.

[79] W. Zinth and U. Zinth, *Optik - Lichtstrahlen - Wellen - Photonen*, Oldenbourg Verlag München, 2009.

[80] I. J. Hodgkinson and Q.-H. Wu, *Birefringent thin films and polarizing elements*, World Scientific, 1997.

[81] F. L. Pedrotti, S. J. and L. S. Pedrotti, *Introduction to optics*, Pearson - Prentice Hall, 1993.

[82] O. Levy and D. Stroud, *Maxwell Garnett theory for mixtures of anisotropic inclusions: Application to conducting polymers*, Phys. Rev. B **56**, 8035 (1997).

[83] L. D. Stefano, I. Rendina, L. Moretti, S. Tundo, and A. M. Rossi, *Smart optical sensors for chemical substances based on porous silicon technology*, Appl. Opt. **43**, 167 (2004).

[84] E. Gross, D. Kovalev, N. Künzner, V. Y. Timoshenko, J. Diener, and F. Koch, *Highly sensitive recognition element based on birefringent porous silicon layers*, J. Appl. Phys. **90**, 3529 (2001).

[85] N. Künzner, E. Gross, D. Kovalev, V. Y. Timoshenko, and D. Wallacher, *Capillary condensation monitored in birefringent porous silicon layers.*, J. Appl. Phys. **94**, 4913 (2003).

[86] V. S.-Y. Lin, K. Motesharei, K.-P. S. Dancil, M. J. Sailor, and M. R. Ghadiri, *A porous silicon-based optical interferometric biosensor*, Science **278**, 840 (1997).

[87] K.-P. S. Dancil, D. P. Greiner, and M. J. Sailor, *A porous silicon optical biosensor: Detection of reversible binding of IgG to a protein A-modified surface*, JACS **121**, 7925 (1999).

[88] S. E. Létant and M. J. Sailor, *Molecular identification by time-resolved interferometry in a porous silicon film*, Adv. Mat. **13**, 335 (2001).

[89] M. P. Stewart and J. M. Buriak, *Chemical and biological applications of porous silicon technology*, Adv. Mat. **12**, 859 (2000).

[90] L. D. Stefano, P. Arcari, A. Lamberti, C. Sanges, L. Rotiroti, I. Rea, and I. Rendina, *DNA optical detection based on porous silicon technology: from Biosensors to Biochips*, Sensors **7**, 214 (2007).

[91] J. J. Saarinen, S. M. Weiss, P. M. Fauchet, and J. E. Sipe, *Optical sensor based on resonant porous silicon structures*, Optics Express **13**, 3754 (2005).

[92] P. A. Snow, E. K. Squire, and P. S. J. Russell, *Vapor sensing using the optical properties of porous silicon bragg mirrors*, J. of Appl. Phys. **86**, 1781 (1999).

[93] H. Ouyang, C. C. Striemer, and P. M. Fauchet, *Quantitive analysis of the sensitivity of porous silicon optical biosensors*, Appl. Phys. Lett. **88**, 163108 (2006).

[94] B. Schulz, D. Chan, J. Bäckström, and M. Rübhausen, *Spectroscopic ellipsometry on biological materials - investigations of hydration dynamics and structural properties*, Thin Solid Films **455-456**, 731 (2004).

[95] N. A. Nicorovici, D. R. McKenzie, and R. C. McPhedran, *Optical resonances of three-phase composites and anomalies in transmission*, Optics Comm. **117**, 151 (1995).

[96] O. L. Muskens, S. L. Diedenhofen, M. H. M. van Weert, M. T. Borgström, E. P. A. M. Bakkers, and J. Gómez Rivas, *Epitaxial growth of aligned semiconductor nanowire metamaterials for photonic applications*, Adv. Func. Mat. **18**, 1039 (2008).

References

[97] J. Gómez Rivas, O. L. Muskens, M. T. Borgström, S. L. Diedenhofen, and E. P. A. M. Bakkers, *One-Dimensional Nanostructures*, volume 3 of *Lecture Notes in Nanoscale Science and Technology*, chapter 6, pages 127–145, Springer, 2008.

[98] S. A. Fortuna and X. Li, *Metal-catalyzed semiconductor nanowires: a review on the control of growth directions*, Semicond. Sci. Technol. **25**, 024005 (2010).

[99] D. S. Wiersma, P. Bartolini, A. Lagendijk, and R. Righini, *Localization of light in a disordered medium*, Nature **390**, 671 (1997).

[100] F. J. P. Schuurmans, D. Vanmaekelbergh, J. van de Lagemaat, and A. Lagendijk, *Strongly photonic macroporous gallium phosphide networks*, Science **284**, 141 (1999).

[101] M. Störzer, P. Gross, C. M. Aegerter, and G. Maret, *Observation of the critical regime near anderson localization of light*, Phys. Rev. Lett. **96**, 063904 (2006).

[102] F. Scheffold, R. Lenke, R. Tweer, and G. Maret, *Localization or classical diffusion of light?*, Nature **398**, 206 (1999).

[103] M. D. Kelzenberg, S. W. Boettcher, J. A. Petykievicz, D. B. Turner-Evans, M. C. Puntam, E. L. Warren, J. M. Spurgeon, R. M. Briggs, N. S. Lewis, and H. A. Atwater, *Enhanced absorption and carrier collection in Si wire arrays for photovoltaic applications*, Nature Mat. **9**, 205 (2010).

[104] X. W. Sun, J. Z. Huang, J. X. Wang, and Z. Xu, *A ZnO nanorod inorganic/organic heterostructure light-emitting diode emitting at 342 nm*, Nano Lett. **8**, 1219 (2008).

[105] H. C. van de Hulst, *Light Scattering by small particles*, Dover Publications, Inc., 1981.

[106] C. G. Bernhard, *Structural and functional adaption in a visual system*, Endeavour **26**, 79 (1967).

[107] W. H. Southwell, *Gradient-index antireflection coatings*, Opt. Letters **8**, 584 (1983).

[108] J. A. Dobrowolski, D. Poitras, P. Ma, H. Vakil, and M. Acree, *Toward perfect antireflection coatings: numerical investigation*, Appl. Opt. **41**, 3075 (2002).

[109] D. Poitras and J. A. Dobrowolski, *Toward perfect antireflection coatings. 2. Theory*, Appl. Opt. **43**, 1286 (2004).

[110] E. B. Grann, M. G. Moharam, and D. A. Pommet, *Optimal design for antireflective tapered two-dimensional subwavelength grating structures*, J. Opt. Soc. Am. A **12**, 333 (1995).

[111] P. Lalanne and G. M. Morris, *Antireflection behaviour of silicon subwavelength periodic structures for visible light*, Nanotechnolgy **8**, 53 (1997).

[112] A. Gombert, W. Glaubitt, K. Rose, J. Dreibholz, B. Bläsi, A. Heinzel, D. Sporn, W. Döll, and V. Wittwer, *Subwavelength-structured antireflective surfaces on glass*, Thin Solid Films **351**, 73 (1999).

[113] Y. Kanamori, M. Sasaki, and K. Hane, *Broadband antireflection gratings fabricated upon silicon substrates*, Opt. Lett. **24**, 1422 (1999).

[114] H. Kikuta, H. Toyota, and W. Yu, *Optical elements with subwavelength structured surfaces*, Optical Review **10**, 63 (2003).

[115] W. Zhou, M. Tao, L. Chen, and H. Yang, *Microstructured surface design for omnidirectional antireflection coatings on solar cells*, J. Appl. Phys. **102**, 103105 (2007).

[116] T. Lohmüller, M. Helgert, M. Sundermann, R. Brunner, and J. P. Spatz, *Biomimetic interfaces for high-performance optics in the deep-UV light range*, Nano Lett. **8**, 1429 (2008).

[117] J.-Q. Xi, M. F. Schubert, J. K. Kim, E. F. Schubert, M. Chen, S.-Y. Lin, W. Liu, and J. A. Smart, *Optical thin-film materials with low refractive index for broadband elimination of Fresnel reflection*, Nature Photonics **1**, 176 (2007).

[118] Y.-F. Huang, S. Chattopadhyay, Y.-J. Jen, C.-Y. Peng, T.-A. Liu, Y.-K. Hsu, C.-L. Pang, H.-C. Lo, C.-H. Hsu, Y.-H. Chang, C.-S. Lee, K.-H. Chen, and L.-C. Chen, *Improved broadband and quasi-omnidirectional anti-reflection properties with biomimetic silicon nanostructures*, Nature Nanotech. **2**, 770 (2007).

[119] C.-H. Sun, W.-L. Min, N. C. Linn, and P. Jiang, *Templated fabrication of large area subwavelength antireflection gratings on silicon*, Appl. Phys. Lett. **91**, 231105 (2007).

[120] C.-H. Sun, P. Jiang, and B. Jiang, *Broadband moth-eye antireflection coatings on silicon*, Appl. Phys. Lett. **92**, 061112 (2008).

[121] Z. Yu, H. Gao, H. Ge, and S. Y. Chou, *Fabrication of large area subwavelength antireflection structures on Si using trilayer resist nanoimprint lithography and liftoff*, J. Vac. Sci. Technol. B **21**, 2874 (2003).

[122] C. H. Chiu, P. Yu, H. C. Kuo, C. Chen, T. C. Lu, S. Wang, S. H. Hsu, Y. J. Cheng, and Y. C. Chang, *Broadband and omnidirectional antireflection employing disordered GaN nanopillars*, Optics Express **16**, 8748 (2008).

[123] J. Zhu, Z. Yu, G. F. Burkhard, C.-M. Hsu, S. T. Connor, Y. Xu, Q. Wang, M. McGehee, S. Fan, and Y. Cui, *Optical absorption enhancement in amorphous silicon nanowire and nanocone arrays*, Nano Lett. **9**, 279 (2009).

[124] P. Vukusic and J. R. Sambles, *Photonic structures in biology*, Nature **424**, 852 (2003).

[125] R. A. Laff, *Silicon nitride as an antireflection coating for semiconductor optics*, Appl. Opt. **10**, 968 (1971).

[126] D. S. Hobbs, B. D. MacLeod, and J. R. Riccobono, *Update on the development of high performance anti-reflecting surface relief micro-structures*, Proc. of SPIE **6545**, 65450Y (2007).

[127] Z. P. Yang, L. C. Ci, J. A. Bur, S. Y. Lin, and P. Ajayan, *Experimental observation of an extremely dark material made by a low-density nanotube array*, Nano Lett. **8**, 446 (2008).

[128] F. J. Garcia-Vidal, *Metamaterials: Towards the dark side*, Nat. Photonics **2**, 215 (2008).

[129] P. Yeh, *Optical waves in layered media*, John Wiley and Sons, New York, Chichester, Brisbane, Toronto, Singapore, 1988.

[130] J. Nelson, *The physics of solar cells*, Imperial College Press, 2003.

[131] L. Cao, J. White, J. S. Park, J. A. Schuller, B. M. Clemens, and M. L. Brongersma, *Engineering light absorption in semiconductor nanowire devices*, Nature Mat. **8**, 643 (2009).

[132] B. Tian, T. J. Kempa, and C. M. Lieber, *Single nanowire photovoltaics*, Chem Soc Rev **38**, 16 (2009).

[133] W. Wei, Y.-Y. Bao, C. Soci, Y. Ding, Z.-L. Wang, and D. Wang, *Direct heteroepitaxy of vertical InAs nanowires on Si substrates for broad band photovoltaics and photodetection*, Nano Lett. **9**, 2926 (2009).

[134] L. Tsakalakos, *Nanostructures for photovoltaics*, Materials Science and Engineering **R62**, 175 (2008).

[135] S. Chattopadhyay, Y. F. Huang, A. J. Jen, A. Ganguly, K. H. Chen, and L. C. Chen, *Anti-reflecting and photonic nanostructures*, Materials Science and Engineering **R 69**, 1 (2010).

[136] O. Muskens, J. Gómez Rivas, R. Algra, E. P. A. M. Bakkers, and A. Lagendijk, *Designing light scattering in nanowire materials for photovoltaic applications*, Nano Lett. **8**, 2638 (2008).

[137] Z. Fan, R. Kapadia, P. W. Leu, X. Zhang, Y.-L. Chueh, K. Takei, K. Yu, A. Jamshidi, A. A. Rathore, D. J. M. W. Ruebusch, and A. Javey, *Ordered arrays of dual-diameter nanopillars for maximized optical absorption*, Nano Lett. **10**, 3823 (2010).

[138] Y.-L. Chueh, Z. Fan, K. Takei, H. Ko, R. Kapadia, A. Rathore, N. Miller, K. Yu, M. Wu, E. Haller, and A. Javey, *Black Ge based on crystalline/amorphous core/shell nanoneedle arrays*, Nano Lett. **10**, 520 (2010).

[139] V. Sivakov, G. Andrä, A. Gawlick, A. Berger, J. Plentz, F. Falk, and S. H. Christiansen, *Silicon nanowire-based solar cells on glass: Synthesis, optical properties, and cell parameters*, Nano Lett. **9**, 1549 (2009).

[140] J. Zhu, Z. Yu, S. Fan, and Y. Cui, *Nanostructured photon management for high performance solar cells*, Mater. Sci. Eng. R **2010**.

[141] E. Garnett and P. Yang, *Light trapping in silicon nanowire solar cells*, Nano Lett. **10**, 1082 (2010).

[142] M. B. Spitzer, C. J. Keavney, S. M. Vernon, and V. E. Haven, *Indium phosphide shallow homojunction solar cells made by metalorganic chemical vapor deposition*, Appl. Phys. Lett. **51**, 364 (1987).

[143] P. Lalanne, M. Besbes, J. P. Hugonin, S. van Haver, O. T. A. Janssen, A. M. Nugrowati, M. Xu, S. F. Pereira, H. P. Urbach, A. S. van de Nes, P. Bienstman, G. Granet, A. Moreau, S. Helfert, M. Sukharev, T. Seideman, F. Baida, B. Guizal, and D. van Labeke, *Numerical analysis of a slit-groove diffraction problem*, J. Europ. Opt. Soc. Rap. Public. **2**, 07022 (2007).

[144] A. Aminian and Y. Rahmat-Samii, *Spectral FDTD: A novel technique for the analysis of oblique incident plane wave on periodic structures*, IEEE Trans. Antennas and Propagation **54**, 1818 (2006).

[145] J. A. Roden and S. D. Gedney, *Convolutional PML (CPML): An Efficient FDTD implementation of the CFS-PML for arbitrary media*, Microw. Opt. Tech. Letters **27**, 334 (2000).

[146] E. Palik, editor, *Handbook of optical constants of solids*, Academic Press, 1998.

[147] F. Patolsky, G. Zheng, O. Hayden, M. Lakadamyali, X. Zhuang, and C. M. Lieber, *Electrical detection of single viruses*, Proceedings of the National Academy of Sciences of the United States of America **101**, 14017 (2004).

[148] Y. Cui, Q. Wei, H. Park, and C. M. Lieber, *Nanowire nanosensors for highly sensitive and selective detection of biological and chemical species*, Science **293**, 1289 (2001).

[149] M. Law, H. Kind, B. Messer, F. Kim, and P. Yang, *Photochemical sensing of NO_2 with SnO_2 nanoribbon nanosensors at room temperature*, Angewandte Chemie **114**, 2511 (2002).

[150] *WHO Air quality guidelines for particulate matter, ozone, nitrogen dioxide and sulfur dioxide*, 2005.

[151] http://www.nationaalkompas.nl/preventie/van-ziekten-en-aandoeningen/infectieziekten/hiv/kosten-van-preventie.

[152] International Energy Agency, *Technology Roadmap - Solar Photovoltaic Energy*, Technical report, International Energy Agency, 2010.

[153] Bundesministerium für Umwelt, Naturschutz und Reaktorsicherheit (BMU), *Entwicklung der erneuerbaren Energien in Deutschland im Jahr 2009*, (2010).

[154] J. Homola, *Surface plasmon resonance based sensors*, Springer Verlag, 2006.

[155] A. Berrier, P. Offermans, R. Cools, B. van Megen, W. Knoben, G. Vecchi, J. Gómez Rivas, M. Crego-Calama, and S. Brongersma, *Enhancing the sensitivity of surface plasmon resonances with porphyrins embedded in nanoporous silica*, (in preparation).

[156] Y. Itagaki, K. Deki, S.-I. Nakashima, and Y. Sadaoka, *Toxic gas detection using porphyrin dispersed polymer composites*, Sensors and Actuators B: Chemical **108**, 393 (2005), Proceedings of the Tenth International Meeting on Chemical Sensors.

[157] A. G. Aberle, T. Lauinger, J. Schmidt, and R. Hezel, *Injection-level dependent surface recombination velocities at the silicon-plasma silicon nitride interface*, Appl. Phys. Lett. **66**, 2828 (1995).

[158] A. W. Bett, F. Dimroth, G. Stollwerck, and O. V. Sulima, *III-V compounds for solar cell applications*, Applied Physics A **69**, 119 (1999).

[159] E. J. Haverkamp, P. Mulder, G. J. Bauhuis, J. J. Schermer, M. M. A. J. Voncken, J. van Deelen, A. T. J. van Niftrik, and P. K. Larsen, *Spectrum and bandgap optimized antireflection coating by numerical simulations*, in *20th European Photovoltaic Solar Energy Conference*, 2005.

Summary

Semiconductor nanowires have received a lot of interest during the last years because of their extreme optical properties. Giant polarization anisotropy in the absorption and emission of light from single nanowires, extreme light confinement assisted by exciton polaritons, and enhanced detection sensitivity of analytes are some examples. These properties are leading to novel applications such as nano-light sources, electrical sensors, or quantum emitters. Many applications, such as nanowire solar cells or LEDs, will rely on large areas covered by ensembles of nanowires. Therefore, for devices based on nanowires, the knowledge on how light propagates in these layers is of utmost importance.

In this thesis, an experimental study on light propagation in ensembles of GaP nanowires and arrays of InP nanowires is given. First, the growth of GaP and InP nanowires using the vapor-liquid-solid growth mechanism by metal-organic vapor phase epitaxy is introduced in Chapter 2. The vapor-liquid-solid growth mechanism requires a metal catalyst particle. Depending on the catalyst, ordered or disordered ensembles of nanowires can be grown. We describe the growth of disordered ensembles of nanowires from a thin gold film and the growth of arrays of nanowires from nanoparticles patterned by substrate conformal imprint lithography. Further, we discuss the nanowire morphology depending on the growth parameters and the substrate. We show that the nanowires grow vertical on (111) substrates. Nanowires grown on (100) substrates preferentially form an angle of 35° with respect to the substrate surface. While the initial diameter of the nanowires is defined by the gold catalyst, increasing the growth temperature allows for growing shells around the nanowires. The growth at a specific temperature results in conically shaped nanowires.

Depending on the morphology of the nanowires, light propagates differently in ensembles of nanowires. While layers of thin nanowires form an effective medium that is strongly birefringent, i.e., the refractive index is different for different polarizations, layers of thick nanowires form a strongly scattering medium with a short scattering mean free path. Conically shaped nanowires form a graded refractive index layer that guides the light into the substrate and therewith reduces the reflection at the interface.

In Chapter 3, the birefringence of thin layers of nanowires is described. The refractive index of these layers of nanowires is different for light polarized along or perpendicular to the nanowire elongation. The difference between the two refractive indices defines

the birefringence parameter. We determine the birefringence by measuring the reflection contrast, i.e., the ratio of reflected light passing through crossed and parallel aligned polarizer and analyzer. We obtain the birefringence parameter of the nanowire layer from fits to the measurements with a transfer-matrix formalism based on Jones calculus. The experimentally determined birefringence is compared to the birefringence parameter determined from Maxwell-Garnett effective medium theory. The birefringence parameter is slightly lower than expected from theory due to bending of the nanowires. We find that the birefringence parameter of layers of nanowires is constant over a broad range of wavelengths.

The large birefringence of ensembles of vertically aligned GaP nanowires can be significantly modified by adding a shell as thin as 10 nm of SiO_2 around the nanowires. In Chapter 4, the modification of the birefringence is determined experimentally by polarization-dependent reflection measurements. This modification is modeled with Maxwell-Garnett effective medium theory and Jones calculus for anisotropic layers. We show that s-polarized light is more sensitive to changes in the surrounding of the nanowires than p-polarized light. The reflection contrast exhibits large and narrow peaks that shift strongly due to the presence of the thin shell.

In contrast to Chapters 3 and 4, where we have determined the birefringence of vertically aligned nanowires, we have investigated the birefringence of nanowire layers that are grown on (100) GaP substrates in Chapter 5. These nanowires are oriented such that they form an angle of 35° with respect to the substrate surface. Due to this alignment, dense ensembles of GaP nanowires form biaxial media. We determine the in-plane birefringence of layers of nanowires with different nanowire diameter by measuring the transmission contrast. We find that a nanowire layer with a certain nanowire diameter forms a $\lambda/4$-waveplate.

In Chapter 6, we describe the propagation of light in layers of thick nanowires. Scattering of light influences the propagation of light depending on the nanowire diameter. We determine the scattering mean free path of light, i.e., the mean distance between two scattering events, in layers of vertically aligned nanowires. We show that the scattering is anisotropic and that the scattering mean free path varies with the angle of incidence due to the alignment of the nanowires. GaP nanowires grown on (100) substrates form a stronger scattering medium than vertically aligned nanowires. We find that ensembles of nanowires belong to the strongest scattering media to date.

In Chapter 7, we describe that graded refractive index layers reduce the reflection and increase the coupling of light into a substrate by matching the refractive index at the interfaces. For obtaining a graded refractive index layer based on GaP nanowires, the GaP filling fraction needs to be gradually increased from the top to the bottom of the layer. We show that ensembles of GaP nanorods form graded refractive index layers when they are conically shaped. Alternatively, a graded refractive index can be obtained using cylindrically shaped nanorods with a distribution of lengths, which also leads to an increased GaP filling fraction at the bottom of the layer. We model the graded index layers using a transfer-matrix method for isotropic layered media. We find that the coupling of light into a GaP substrate is increased for a broad range of wavelengths and angles.

In Chapter 8, we demonstrate experimentally that arrays of base-tapered InP

nanowires on top of an InP substrate form a strongly broadband and omnidirectional absorbing medium due to their specific geometry. Almost perfect absorption of light (higher than 97 %) occurs in the system. We explain the strong optical absorption by finite-difference time-domain simulations and we find that the base-tapered geometry of the nanowires strongly enhances the absorption for wavelengths below the electronic bandgap energy of InP. Above the electronic bandgap energy of InP, the light is efficiently coupled into the underlying substrate due to guided optical modes in the nanowires.

Based on the findings of Chapters 4, 7, and 8, we propose in Chapter 9 possible applications of ensembles of nanowires. The high sensitivity of layers of nanowires to thin shells around the nanowires that is described in Chapter 4, inspired us to propose a very sensitive gas and bio-sensor. Tapered nanowires form a graded refractive index layer, which we describe in Chapter 7. We propose using graded refractive index layers based on GaP nanowires for increasing light coupling into III/V multi-junction solar cells. From the strong absorption of light in arrays of base-tapered InP nanowires (Chapter 8), we propose a novel solar cell concept based on base-tapered nanowire arrays.

SAMENVATTING IN HET NEDERLANDS

Halfgeleidende nanodraden hebben de afgelopen jaren grote wetenschappelijke interesse gewekt vanwege hun uitzonderlijke optische eigenschappen. Voorbeelden zijn de 'reuze polarisatie-anisotropy' in de lichtabsorptie en de lichtemissie van afzonderlijke nanodraden, het extreem sterk invangen van licht ten gevolge van excitonpolaritonen, en een verhoogde gevoeligheid van de detectie van analieten. Deze eigenschappen leiden tot nieuwe toepassingen zoals nano-lichtbronnen, elektrische sensoren of quantum emitters. Veel toepassingen, zoals zonnecellen of LEDs zullen gebruik maken van grote ensembles van nanodraden. Daarom is het belangrijk om te weten hoe licht zich in zulke uit nanodraden bestaande lagen voortplant.

In dit proefschrift wordt een experimentele studie van de voortplanting van licht in ensembles van GaP nanodraden en patronen van InP nanodraden gepresenteerd. Allereerst wordt in hoofdstuk 2 beschreven hoe men GaP en InP nanodraden kan laten groeien door middel van de damp-vloeistof-vaste stof-reactie met metaalorganische gasfaseëpitaxie. De damp-vloeistof-vaste stof-reactie heeft kleine metaal druppels als katalysator nodig. Afhankelijk van de aard van de katalysator kan men geordende of ongeordende ensembles van nanodraden laten groeien. We beschrijven het laten groeien van ongeordende ensembles van nanodraden uitgaande van een dunne laag goud en het laten groeien van patronen van nanodraden uitgaande van nano-deeltjes die door substraatconforme imprint-lithografie zijn gestructureerd. Verder beschrijven we de morfologie van de nanodraad, die van de groeiparameters en het substraat afhankelijk is. We laten zien dat de nanodraden verticaal op een (111) substraat groeien. Op (100) substraten groeien nanodraden bij voorkeur onder een hoek van 35° ten opzichte van het substraat. De initiële doorsnede van de nanodraden wordt vastgelegd door de goudkatalysator, maar door de groeitemperatuur te verhogen kan de doorsnede van de nanodraden vergroot worden. Bij een specifieke temperatuur kunnen taps toelopende nanodraden worden gegroeid.

Op welke manier het licht zich in een laag nanodraden voortplant hangt af van hun morfologie. Lagen dunne nanodraden vormen een effectief medium dat sterk dubbel-brekend is, d.w.z. dat de brekingsindex van deze lagen van de polarisatie van het licht afhangt. Lagen dikke nanodraden vormen een sterk licht verstrooiend medium, met een

korte gemiddelde vrije weglengte. Taps toelopende nanodraden vormen een medium met langzaam oplopende brekingsindex, waardoor ze het licht in het substraat in leiden en daardoor de reflectie aan het grensvlak verlagen.

In hoofdstuk 3 beschrijven we de dubbelbreking van lagen dunne nanodraden. De brekingsindex van deze lagen is verschillend voor licht dat langs de nanodraden of loodrecht erop is gepolariseerd. Het verschil tussen deze twee brekingsindices definieert de dubbelbrekingsparameter. We bepalen de dubbelbrekingsparameter door het reflectiecontrast te meten, dus de intensiteitsverhouding van gereflecteerd licht dat door gekruiste of door parallel uitgelijnde polarisator en analysator loopt. De dubbelbrekingsparameter verkrijgen wij door deze meetingen te fitten met behulp van een transfermatrix formalisme dat op de Jones calculus gebaseerd is. We vergelijken de experimenteel gevonden dubbelbrekingsparameter met de dubbelbrekingsparameter, zoals berekend door middel van Maxwell-Garnett effectieve medium theorie. De gemeten dubbelbrekingsparameter is iets lager dan theoretisch verwacht omdat de nanodraden niet helemaal rechtop staan, maar gebogen zijn. We vinden dat de dubbelbrekings- parameter van een laag nanodraden constant is over een breed golflengtegebied.

De hoge dubbelbreking van ensembles van rechtop staaande GaP nanodraden kan sterk veranderd worden door een SiO_2 mantel met een dikte van 10 nm rond de nano- draden aan te brengen. In hoofdstuk 4 is deze verandering van de dubbelbreking experi- menteel onderzocht door middel van polarisatie-afhankelijke metingen. De verander- ing is gemodeleerd met behulp van Maxwell-Garnett effectieve medium theorie en Jones calculus voor anisotrope lagen. We laten zien dat s-gepolariseerd licht gevoeliger is voor veranderingen in de omgeving van de nanodraden dan p-gepolariseerd licht. Het reflectie contrast heeft hoge en smalle pieken die verschuiven door de aanwezigheid van dunne mantels rond de nanodraden.

In tegenstelling tot hoofdstukken 3 en 4, waar we de dubbelbreking van ensembles van rechtop staande nanodraden hebben onderzocht, onderzoeken we in hoofdstuk 5 de dubbelbreking van lagen bestaande uit nanodraden die op een (100) substraat gegroeid zijn. Deze nanodraden zijn zo georiënteerd dat zij een hoek van 35° met het substraat vormen. Door deze uitlijning vormen deze lagen een biaxiaal medium. We hebben de invlaksdubbelbreking van lagen bestaand uit nanodraden met verschillende doorsnede bepaald door het transmissie contrast te meten. Een laag nanodraden met een bepaalde draad doorsnede vormt een kwartlambdaplaat.

In hoofdstuk 6 beschrijven we de voortplanting van licht in lagen dikke nanodraden. De invloed van lichtverstrooing op de voortplanting van het licht is afhankelijk van de nanodraad doorsnede. We bepalen de gemiddelde vrije weglengte van het licht, dus de afstand tussen twee opeenvolgende verstrooiingen, in lagen rechtop staande nanodraden. We laten zien dat de lichtverstrooiing anisotroop is en dat ten gevolge van de uitlijning van de nanodraden de vrije weglengte verandert bij verandering van de invalshoek van het licht. GaP nanodraden die op een (100) substraat gegroeid zijn verstrooien licht sterker dan de ensembles van rechtop staande nanodraden. We vinden dat ensembles van nano- draden tot de sterkst verstrooiende materialen behoren.

In hoofdstuk 7 beschrijven we hoe een geleidelijk oplopende brekingsindex de reflectie verlaagt en de inkoppelingsefficiëntie naar een substraat verhoogt doordat deze

de brekingsindices aan het grensvlak op elkaar aanpast. Om uit GaP nanodraden een laag met geleidelijk oplopende brekingsindex te maken, bestaand uit GaP nanodraden te maken, is het nodig om de GaP vulfractie van boven naar beneden geleidelijk te laten toenemen. We laten zien dat ensembles van GaP nanodraden een geleidelijk oplopende brekingsindex vormen als ze taps toelopen. Ook hebben we een laag met geleidelijk oplopende brekingsindex gemaakt uit cilindrische nanodraden van ongelijke lengte. Ten gevolge van deze lengteverdeling bevind zich onderin de laag ook meer materiaal. We modelleren de geleidelijke oplopende brekingsindex met behulp van een transfer-matrix methode voor isotrope materialen. We vinden dat de laag nanodraden ervoor zorgt dat er over een breed golflengtebereik en hoekbereik meer licht in een GaP substraat inkoppelt.

In hoofdstuk 8 laten we zien dat patronen bestaand uit aan de basis taps uitlopende InP nanodraden op een InP substraat door de specifieke geometrie van de nadraden een medium vormen dat over een breed spectrum en ook over een groot hoekbereik sterk absorbeert. Het systeem vertoont bijna perfecte lichtabsorptie (hoger dan 97 %). We verklaren de sterke optische absorptie met behulp van eindige-differentie berekeningen in het tijdsdomein en we vinden dat de sterke absorptie voor golflengtes korter dan overeenkomend met de elektrische bandgap van InP door de tapse vorm van de basis komt. Licht met golflengtes langer dan overeenkomend met de elektrische bandgap koppelt juist efficiënt in in het substraat vanwege het bestaan van golfgeleidende optische modes in de nanodraden.

Gebaseerd op de resultaten van hoofdstuk 4, 7 en 8 stellen we in hoofdstuk 9 mogelijke toepassingen van ensembles van nanodraden voor. De hoge gevoeligheid van de optische eigenschappen van lagen nanodraden voor de aanwezigheid van dunne mantels rond de nanodraden, die in hoofdstuk 4 is gepresenteerd, inspireerde ons om een heel gevoelige gas- en biosensor voor te stellen. Taps toelopende nanodraden vormen een laag met geleidelijk oplopende brekingsindex zoals in hoofdstuk 7 beschreven staat. We stellen voor om deze lagen te gebruiken om meer licht in een III/V multijunctiezonnecel in te koppelen. De sterke lichtabsorptie in patronen van aan de basis taps uitlopende InP nanodraden (hoofdstuk 8) brengt ons ertoe om een nieuwe zonnecel voor te stellen die op zulke nanodraden gebaseerd is.

ZUSAMMENFASSUNG

Halbleiter-Nanodrähte haben in den letzten Jahren wegen ihrer extremen optischen Eigenschaften großes Interesse geweckt. Riesige Polarisationsanisotropie der Absorption und Emission einzelner Nanodrähte, extreme Lichtbegrenzung durch Exziton-Polaritonen und verstärkte Empfindlichkeit in der Detektion von Analyten sind einige Beispiele. Diese Eigenschaften führen zu neuen Anwendungen wie zum Beispiel Nano-Lichtquellen, elektrischen Sensoren oder Quantenemittern. Viele Anwendungen, wie Nanodraht-Solarzellen oder LEDs, werden auf großflächigen Nanodraht-Ensembles basieren. Deshalb ist es wichtig zu wissen, wie sich Licht in solchen Nanodrahtschichten ausbreitet.

Diese Dissertation enthält eine experimentelle Charakterisierung der Fortpflanzung von Licht in GaP-Nanodraht-Ensembles und InP-Nanodraht-Arrays. Das Wachstum der GaP- und InP-Nanodrähte durch den Vapor-Liquid-Solid Mechanismus in der Metallorganischen Gasphasenepitaxie (MOVPE) ist in Kapitel 2 beschrieben. Der Vapor-Liquid-Solid Mechanismus erfordert einen Metall-Katalysator. Abhängig vom Katalysator werden geordnete oder ungeordnete Nanodraht-Ensembles gewachsen. Wir beschreiben das Wachstum der ungeordneten Nanodraht-Ensembles mittels eines dünnen Goldfilms und das Wachstum von geordneten Nanodraht-Arrays mittels Goldpartikeln, die durch substrat-konforme Imprint-Lithographie strukturiert sind. Des Weiteren beschreiben wir die Nanodraht-Morphologie, die von den Wachstumsparametern und vom Substrat abhängt. Wir zeigen, dass die Nanodrähte auf (111)-Substraten vertikal wachsen. Nanodrähte, die auf (100)-Substraten gewachsen sind, formen vorzugsweise einen 35°-Winkel mit der Oberfläche. Der Durchmesser der Nanodrähte ist durch die Größe des Katalysatorpartikels gegeben. Durch Wachstum bei einer höheren Temperatur kann der Durchmesser vergrößert werden. Bei einer bestimmten Temperatur ist es möglich, konische Nanodrähte zu wachsen.

Licht pflanzt sich abhängig von der Morphologie der Nanodrähte unterschiedlich in Nanodraht-Ensembles fort. Während Lagen dünner Drähte ein effektives Medium bilden, das stark doppelbrechend ist, das heißt, dass der Brechungsindex abhängig von der Polarisation ist, sind Lagen dicker Nanodrähte stark streuend, mit einer kurzen freien Weglänge. Konische Nanodrähte formen eine Lage mit graduellem Brechungsindex, die das Licht in das Substrat leiten und dadurch die Reflexion an der Oberfläche reduzieren.

In Kapitel 3 ist die Doppelbrechung der Lagen dünner Nanodrähte beschrieben.

Der Brechungsindex dieser Nanodraht-Lagen ist unterschiedlich für Licht, das parallel oder senkrecht zur Nanodraht-Achse polarisiert ist. Der Unterschied zwischen den beiden Brechungsindizes definiert den Doppelbrechungsparameter. Wir bestimmen die Doppelbrechung durch Messungen des Reflexionskontrasts. Es sind zwei Messungen erforderlich, um den Reflexionskontrast zu ermitteln: Bei der ersten werden Polarisator und Analysator gekreuzt, bei der zweiten parallel ausgerichtet. Der Reflexionskontrast ergibt sich aus dem Verhältnis der Intensitäten der beiden Messungen. Wir erhalten den Doppelbrechungsparameter, indem wir die Messungen durch Berechnungen mit Hilfe eines Transfer-Matrix Formulismus auf Basis des Jones Calculus angleichen. Wir haben den experimentell ermittelten Doppelbrechungsparameter mit dem Wert verglichen, der mittels der Theorie effektiver Medien nach Maxwell-Garnett berechnet wurde. Der experimentelle Doppelbrechungsparameter ist etwas geringer als der theoretisch erwartete, weil die Nanodrähte nicht gerade stehen. Wir haben bestimmt, dass der Doppelbrechungsparameter über einen breiten Spektralbereich konstant ist.

Die starke Doppelbrechung vertikal ausgerichteter Nanodraht-Ensembles kann durch das Anbringen einer 10 nm dünnen Hülle um die Nanodrähte signifikant verändert werden. In Kapitel 4 ermitteln wir die Veränderung experimentell durch polarisationsabhängige Reflexionsmessungen. Wir beschreiben diese Veränderung mit Hilfe der Theorie effektiver Medien nach Maxwell-Garnett und dem Jones Calculus für anisotrope Medien. Wir zeigen, dass s-polarisiertes Licht empfindlicher für Veränderungen in der Umgebung der Nanodrähte ist als p-polarisiertes Licht. Der Reflexionskontrast zeigt große und schmale Spitzen, die sich durch die Anwesenheit der dünnen Hüllen stark verschieben.

Im Gegensatz zu Kapitel 3 und 4, in denen wir die Doppelbrechung vertikaler Nanodrähte beschrieben haben, befassen wir uns in Kapitel 5 mit der Doppelbrechung der Nanodrähte, die auf (100)-GaP-Substraten gewachsen sind. Diese Nanodrähte sind so angeordnet, dass sie einen 35°-Winkel mit der Substratoberfläche bilden. Wegen dieser Ausrichtung formen dichte GaP-Nanodraht-Ensembles ein biaxiales Medium. Wir bestimmen die Doppelbrechung in Nanodrahtproben mit unterschiedlichen Nanodrahtdurchmessern durch Messungen des Transmissionskontrasts. Es zeigt sich, dass eine Nanodrahtschicht mit einem bestimmten Nanodrahtdurchmesser einer $\lambda/4$-Platte entspricht.

In Kapitel 6 beschreiben wir die Fortpflanzung von Licht in Schichten, die aus dicken Nanodrähten bestehen. Lichtstreuung beeinflusst abhängig vom Nanodrahtdurchmesser die Ausbreitung des Lichts. Wir bestimmen die freie Weglänge des Lichts, das heißt den durchschnittlichen Abstand zwischen zwei Streuprozessen, in Schichten vertikaler Nanodrähte. Wir zeigen, dass die Streuung anisotrop ist und dass die freie Weglänge auf Grund der Ausrichtung der Nanodrähte vom Einfallswinkel abhängt. GaP-Nanodrähte, die auf einem (100)-Substrat gewachsen sind, streuen das Licht stärker als vertikale Nanodrähte. Unsere Resultate belegen, dass Nanodraht-Ensembles zu den am stärksten streuenden Medien gehören.

In Kapitel 7 beschreiben wir, wie graduelle Brechungsindexschichten die Reflexion verringern und auf Grund der Brechungsindexanpassung an den Schnittstellen mehr Licht in ein Substrat koppeln. Um eine graduelle Brechungsindexschicht aus GaP-Nanodrähten zu erhalten, ist es nötig, dass der GaP-Füllanteil von oben nach unten langsam ansteigt. Wir zeigen, dass konische Nanodrähte eine graduelle Brechungs-

indexschicht formen. Alternativ lässt sich eine solche Schicht mit graduell variierendem Brechungsindex mittels vertikaler zylindrischer Nanodrähte erzeugen. Diese formen eine graduelle Brechungsindexschicht durch unterschiedliche Längen der Nanodrähte, die auch dazu führen, dass mehr GaP unten in der Schicht vorhanden ist. Wir modellieren diese graduellen Brechungsindexschichten mit Hilfe einer Transfer-Matrix-Methode für isotrope Medien. Wir zeigen, dass über einen breiten Spektralbereich und einen weiten Einfallswinkelbereich mehr Licht in das Substrat gekoppelt wird.

In Kapitel 8 zeigen wir experimentell, dass Arrays von Nanodrähten, deren unterer Teil konisch ist, auf Grund ihrer spezifischen Geometrie ein breitbandig und omnidirektional absorbierendes Medium formen. In diesem System tritt fast perfekte Absorption des Lichts (mehr als 97 %) auf. Wir erklären die starke optische Absorption durch finite-difference time-domain (FDTD) Simulationen. Die Simulationen zeigen, dass die konische Basis der Nanodrähte die Absorption für Wellenlängen, die kürzer als die elektronische Bandkantenenergie von InP sind, stark verstärkt. Für Wellenlängen länger als die Bandkantenenergie von InP wird das Licht auf Grund von geführten optischen Moden in den Nanodrähten effizient in das Substrat gekoppelt.

Basierend auf den Ergebnissen der Kapitel 4, 7 und 8, stellen wir in Kapitel 9 mögliche Anwendungen der Nanodrähte vor. Die hohe Empfindlichkeit der Reflexion von Licht der Nanodraht-Schichten gegenüber dünnen Hüllen um die Nanodrähte, die in Kapitel 4 beschrieben wurden, inspirierte uns, sehr empfindliche Gas- und Biosensoren vorzuschlagen. Konische Nanodrähte formen eine graduelle Brechungindexschicht, die wir in Kapitel 7 beschrieben haben. Wir schlagen vor, graduelle Brechungsindexschichten aus GaP-Nanodrähten zu verwenden, um mehr Licht in eine III/V-Solarzelle zu koppeln. Auf Grund der starken Absorption des Lichts in Nanodrähten mit konischer Basis (Kapitel 8), schlagen wir ein neues Solarzellenkonzept vor, das auf Nanodrähten mit konischer Basis basiert.

NOTATION

$\mathbf{A}_r$	reflected amplitude
A	absorbance
a	amplitude of right-traveling wave
b	amplitude of left-traveling wave
c	speed of light
$\mathbf{D}$	electric displacement field
$\mathbf{D}_{\alpha\alpha+1}$	transmission matrix at the interface of media α and $\alpha+1$
d	nanowire diameter
d_{NW}	distance between two nanowire midpoints
$\mathbf{E}$	electric field
f	filling fraction
$\mathbf{H}$	magnetic field
I	intensity
$I_\parallel$	intensity for parallel aligned polarizer and analyzer
$I_\perp$	intensity for crossed polarizer and analyzer
I_i	incident irradiance
$\mathbf{J}$	Jones vector
$\mathbf{k}$	wavevector
k	wavenumber
k_{eff}	extinction coefficient
kr	size parameter
kl_s	scattering strength
L	nanowire layer thickness
L'	optical path length
l	unit length
l_s	scattering mean free path
$\mathbf{M}$	matrix
n	refractive index
$\mathbf{OA}$	vector describing the analyzer

165

OB	projection of the vector **OE** onto the slow axis
OC	projection of the vector **OE** onto the fast axis
OE	vector parallel to the polarizer
OF	amplitude of the field parallel to the analyzer
OP	vector describing the polarizer
P	propagation matrix
$Q_{sc,s,p}$	scattering efficiency for s- and p-polarization
R	reflectance
R	reflection
r	radius
r	distance
$r_{s,p}$	reflection coefficient for s- and p-polarization
$S_{sc,s,p}$	Poynting vector of s- and p-polarized scattered light
T	transmission
t	time
$t_{s,p}$	transmission coefficient for s- and p-polarization
v_p	phase velocity
$W_{sc,s,p}$	scattered power for s- and p-polarization
α_1	depolarization factor
χ	angle between polarizer and analyzer
Δ	retardation
Δn	birefringence parameter
δ	phase difference
ϵ	permittivity
λ	wavelength in vacuum
Φ	azimuthal angle
ϕ	phase change of light
ρ	density of nanowires
σ_s	scattering cross section
θ	angle of incidence
θ'	internal angle
θ_α	internal angle in medium α
$\theta_{s,p}^g$	group velocity for s- and p-polarization
ω	angular frequency

ACKNOWLEDGMENTS

Writing a thesis and conducting PhD-research is a long and tedious process. While there are plenty of tough moments, most of the time was pure fun. Installing optical setups comes close to playing with "LEGO"[1] bricks during work-time. Understanding the measurement data after relating them during a time-consuming process to theory results in moments of great relief and happiness. Presenting these results to a broad audience and receiving positive feedback makes up for the cumbersome work. Well, to sum up, the last four years have been a great time. That I enjoyed the last four years so much is due to quite some people, whom I thank a lot.

First of all, I am very grateful to Jaime, who gave me the possibility to work on nanowires in his group. Jaime, thanks a lot for the stimulating discussions, the motivation during the hard times, the critical view on my data, and for helping me to grow as a scientist. It was great working together with you and I am quite sure that I will miss our endless scientific fights. I know now that you were right most of the times.

Heel veel dank aan Erik. Zonder jou en jouw onderzoek naar nanodraden bij Philips en later op de TU/e was mijn project niet mogelijk geweest. Bedankt niet alleen voor het delen van informatie over het groei-proces, maar ook over het leven en het werken in Nederland. Het is een mooi land om in te leven en te werken, ook al was het niet altijd zo makkelijk als ik gehoopt/gewenst had.

I also like to thank all the members of the Surface Photonics group from AMOLF. Otto it was nice working together with you on nanowires, also after you left to the Photon Scattering group. Your knowledge on nanowires helped me a lot when starting my PhD-project. Manuel, I learned a lot from you on handling optical equipment. Thanks for that. Yichen, you were always open for coffee breaks during which we talked not only about science but also about the cultural differences of Germany, The Netherlands, China and different other countries. It was interesting to hear your opinion on politics, which differs so much from the European point of view. Gabriele, thanks for the nice time in the lab, sharing an office, and the useful discussion. I have learned a lot from you. Vincenzo, thanks to your very open personality it was a pleasure to work together with you. You were always open for discussing theoretical questions. I understood that you disliked going

---

[1]LEGO®is a trademark of the LEGO Group.

CURRICULUM VITAE

Silke L. Diedenhofen is born in 1980 in Goch, Germany. After her Abitur in 2000 at the "Städtisches Gymnasium Kalkar", she studied electrical engineering at the "Universität Duisburg-Essen" in Duisburg, Germany. During her studies she worked as an undergraduate student for 3 years in the Optoelectronics group. She did her student research project for 5 months in the group Electronic Materials and Nanostructures and has performed an internship with Bookham Inc. in Caswell, England. In 2006 she finished her studies with her Diplomarbeit on "Vertikale elektrooptische Modulatoren auf Halbleiterbasis" (Vertical Electrooptical Modulators based on Semiconductors) in the Optoelectronics group under supervision of Prof. Dieter Jäger. In May 2006 she started her PhD project in the group Nanowire Photonics/Surface Photonics under supervision of Jaime Gómez Rivas. She was the 1st AMOLF PhD student in the FOM industrial partnership program "Microphotonic Light Sources" that combined AMOLF and Philips. The industrial partnership program allowed her to conduct her research at Philips Research in combination with regular work-discussions at AMOLF. In her free time she likes reading books, playing the clarinet and traveling.

LIST OF PUBLICATIONS

This thesis is based on the following publications:

1. *Generic Nano-Imprint Process for Fabrication of Nanowire Arrays*, Aurélie Pierret, Moïra Hocevar, Silke L. Diedenhofen, Rienk E. Algra, E. Vlieg, Eugene C. Timmering, Marc A. Verschuuren, George W. G. Immink, Marcel A. Verheijen, Erik P. A. M. Bakkers, Nanotech. **21**, 065305 (2010) **(Chapter 2)**

2. *Optical Anisotropy of Semiconductor Nanowires*, Jaime Gómez Rivas, Otto L. Muskens, Magnus T. Borgström , Silke L. Diedenhofen, and Erik P. A. M. Bakkers, *One-Dimensional Nanostructures*, Volume 3 of *Lecture Notes in Nanoscale Science and Technology*, chapter 6, pages 127-145, Springer (2008) **(Chapter 3)**

3. *Modified Reflection in Birefringent Layers of Core-Shell Semiconductor Nanowires*, Silke L. Diedenhofen and Jaime Gómez Rivas, Semicond. Sci. Technol. **25**, 024008 (2010). **(Chapter 4)**

4. *Refractive Index Sensing using Semiconductor Nanowires*, Silke L. Diedenhofen, Rienk E. Algra, Erik P. A. M. Bakkers, and Jaime Gómez Rivas, in preparation. **(Chapter 4)**

5. *Epitaxial Growth of Aligned Semiconductor Nanowire Metamaterials for Photonic Applications*, Otto L. Muskens, Silke L. Diedenhofen, Maarten H. M. van Weert, Magnus T. Borgström, Erik P. A. M. Bakkers, and Jaime Gómez Rivas, Adv. Func. Mat. **18**, 1039 (2008). **(Chapter 5)**

6. *Anisotropic Scattering of Light by ensembles of Semiconductor Nanowires*, Silke L. Diedenhofen, Otto L. Muskens, and Jaime Gómez Rivas, in preparation. **(Chapter 6)**

7. *Broad-band and Omnidirectional Anti-Reflection Coatings based on Semiconductor Nanowires*, Silke L. Diedenhofen, Gabriele Vecchi, Rienk E. Algra, Alex Hartsuiker, Otto L. Muskens, George Immink, Erik P. A. M. Bakkers, Willem L. Vos, and Jaime Gómez Rivas, Adv. Mat., **21**, 973 (2009) also highlighted in Physica Status Solidi RRL, **3**, A52 (2009). **(Chapter 7)**

8. *Efficiënt licht invangen met behulp van nanogestructureerde oppervlakken*, Silke L. Diedenhofen, Rienk E. Algra, Erik P. A. M. Bakkers, Jaime Gómez Rivas, Nederlands Tijdschrift voor Natuurkunde, **75**, 176 (2009). **(Chapter 7)**

9. *Extraordinary Broadband and Omnidirectional Absorption in Arrays of Base-Tapered Semiconductor Nanowires*, Silke L. Diedenhofen, Olaf T. A. Janssen, Grzegorz Grzela, Erik P. A. M. Bakkers, Jaime Gómez Rivas, submitted. **(Chapter 8)**

Other publications by the author:

1. *Nanoscale Free-Carrier Profiling of Individual Semiconductor Nanowires by Infrared Near-field Nanoscopy*, Johannes M. Stiegler, Andreas J. Huber, Silke L. Diedenhofen, Jaime Gómez Rivas, Rienk E. Algra, Erik P. A. M. Bakkers, Rainer Hillenbrand, Nano Letters, **10**, 1387 (2010).

2. *Large Photonic Strength of Highly Tunable Resonant Nanowire Materials*, Otto L. Muskens, Silke L. Diedenhofen, Bernard C. Kaas, Rienk E. Algra, Erik P. A. M. Bakkers, Jaime Gómez Rivas, and Ad Lagendijk, Nano Lett. **9**, 930 (2009), also highlighted in Nature Photonics, **3**, 186 (2009).

3. *Directional Light Emission from Arrays of Semiconductor Nanowires*, Silke L. Diedenhofen, Aurélie Pierret, Olaf T. A. Janssen, Moïra Hocevar, Rienk E. Algra, Erik P. A. M. Bakkers, and Jaime Gómez Rivas, in preparation.

4. *Experimental Determination of the Optical Constants of Layers of Wurtzite InP Nanowires*, Silke L. Diedenhofen, Lou-Fé Feiner, Moïra Hocevar, Erik P. A. M. Bakkers, and Jaime Gómez Rivas, in preparation.